Università Politecnica delle Marche
Scuola di Dottorato di Ricerca in Scienze dell'Ingegneria
Curriculum in Ingegneria Civile, Ambientale, Edile ed Architettura

---

Applications of industrialised GFRP components, structural adhesives and solar selective coatings on construction elements: durability experimental studies.

Ph.D. Dissertation of:

Margherita Giampaoli

Advisor:

Prof. Placido Munafò

XV Ciclo – new series

Università Politecnica delle Marche
Scuola di Dottorato di Ricerca in Scienze dell'Ingegneria
Curriculum in Ingegneria Civile, Ambientale, Edile ed Architettura

---

Applications of industrialised GFRP components, structural adhesives and solar selective coatings on construction elements: durability experimental studies.

Ph.D. Dissertation of:

Margherita Giampaoli

Advisor:

Prof. Placido Munafò

XV Ciclo – new series

Università Politecnica delle Marche
Dipartimento di Ingegneria Civile, Edile ed Architettura (DICEA)
Via Brecce Bianche — 60131 - Ancona, Italy

Alla mia amata famiglia

Al mio amore

Ringraziamenti

Arrivata alla conclusione di questo affascinante triennio, i miei ringraziamenti vanno innanzitutto al mio tutor prof. Placido Munafò. Sapientemente guidata in questo vastissimo mondo della ricerca, ora più che mai comprendo come tutte le esperienze avute appartengano ad un filo conduttore, lo stesso che poi va a costituire il gomitolo della mia formazione professionale.
Nel mio percorso formativo inserisco anche la prof. Francesca Stazi, con la quale ho intrapreso lo studio e la scrittura dei primi articoli scientifici. Senza di lei non avrei acquisito una certa padronanza di questo lavoro piuttosto complesso, la stessa che mi accompagnerà nel futuro prossimo, e che spero di poter migliorare sempre più.
Un caloroso ringraziamento anche al Ricercatore Marco Rossi, alla prof.ssa Francesca Tittarelli, al prof. Costanzo di Perna, all'Ing. Gianluca Chiappini, all'Ing. Luigi Montalto, all'Ing. Antonio Dantuono, all'Ing. Adriano di Cristoforo, e a tutti i tecnici: Franco Rinaldi, Andrea Conti, Giuliano Giuliani, Giampaolo Giuliani, Carla Conti, grazie ai quali gli studi descritti nella presenti tesi sono stati condotti ed hanno avuto esito positivo.
Grazie a Vanessa, collega, socia, amica. Con te lavoro, mi confronto, mi confido, mi sento sostenuta e cresco. Non vorrei o potrei volere una persona diversa a mio fianco. Grazie a Giovanni, Gianluca, Lorenzo, Sara e agli altri ragazzi del dipartimento, ancora presenti e non, ognuno di voi mi ha permesso di fare una bella esperienza in questi tre anni vissuti insieme.

Tutto questo sarebbe stato impossibile senza la mia adorata famiglia, di questa e di chissà quante vite. Non c'è giorno senza la consapevolezza di quanto mi sento amata e di quanto vi amo. Senza voi non sarei proprio quella che sono, il vostro amore è la base di tutto.
Grazie a Rodo, ragazzo e compagno, le nostre strade si sono affiancate così naturalmente, e magicamente allo stesso modo proseguono; ogni giorno di questa mia importante esperienza mi hai sostenuta con l'amore, il rispetto, la simpatia e l'umiltà che ti contraddistinguono.

Un pensiero alle mie carissime amiche e amici, di tutte le età, vicini e lontani, siete una delle mie più dolci certezze. Grazie a Lucy, potremo crescere all'infinito senza cambiare mai la nostra amicizia. Grazie a Mario, sei come un fratello ed un angelo allo stesso tempo. Grazie a Jess, che ha dato un contributo alla tesi, e a Phil, bellissimo avervi conosciuti.
Grazie alle ragazze che si stanno dottorando con me, è stato fondamentale condividere gioie e dolori di questi tre anni. Grazie alle amiche di tessuti, con voi ho compreso che tutto si può avverare, basta volerlo.

Grazie a me stessa.
"Marghe avevi così tanta paura di non essere all'altezza, eppure era proprio la tua strada".
Chissà dove mi porterà, ma era proprio questa.

Ancona, novembre 2016 *Margherita*

Abstract

The *aim* of this work is to demonstrate the applicability of innovative materials, such as Glass Fibre Reinforced Polymer (GFRP) industrialized components (profiles), structural adhesives, and solar selective coatings, on construction elements, from the design phase to the industrialization process, with the objective of their commercialization on the national and international market.

Following the "Technological Simplification" principle, the research group designed and patented the *Full Glass* window frame (patent n. PCT/IB2014/066098) and the *Structural Member* for curtain walls (patent application n. 102015000087569), high-performance and easy to assemble components composed of these innovative materials in a limited number of pieces. In this thesis, the *feasibility of the ideas behind the patents* is tested. Two different aspects were investigated: the mechanical performance of the GFRP profiles and of the structural adhesives, for their application both on windows and on curtain walls; the energy performance of the solar selective coatings, for their implementation on the glass surfaces. The degradation mechanisms (durability) of the materials were also extensively analyzed.

The *methods* used were mostly of the experimental type. The components and materials properties (mechanical, physical, chemical, optical) were tested in laboratory conditions and the effects of different types of ageing conditions were analysed, such as continuous condensation (ISO 6270-2 and UNI EN 1096-2), temperature and moisture changes (EN ISO 9142), UV irradiation (ASTM D904–99 and ASTM G154–00a) and saline spray (UNI EN 1096-2). Furthermore, numerical and analytical studies were carried out, with the objective to check and validate the results obtained through experimental tests.

The *main outcome was the validation of the patents* (the *Full Glass* window and the *Structural Member* for curtain walls) *basic ideas*, which is a key point in the industrialization process of the construction elements. Experimental results, in fact, demonstrated that the use of GFRP profiles, also bonded with structural adhesives and combined with steel, is successful on windows and curtain walls, even when they are exposed to adverse environmental conditions. Furthermore, the study of the glass coatings was useful to deepen the improvement of the energy performance of the glazed construction elements.
Moreover, the *industrialization process* of the innovative construction components was discussed, demonstrating the feasibility of the transfer of a research result, based on the principle of the "Technological Simplification", to the production world and, then, to the market.

Contents

Chapter 1

Overall introduction

1.1 Objectives

The aim of the Ph.D. research was the transfer of innovative elements, consisting of advanced components and materials, to the construction market.
Over the last few years, the working group has designed and patented the *Full Glass* window frame (patent n. PCT/IB2014/066098) and the *Structural Member* for curtain walls (patent application n. 102015000087569). The guiding principle is mainly the "Technological Simplification" a method to realize high-performance and easy to assemble components, by using innovative materials in a limited number of pieces. This principle led to low energy consumption in the production, assembly, maintenance and disposal processes, becoming the new concept of "environmental sustainability" [1].

In this work, the feasibility of the ideas behind the patented construction elements is checked. Particularly, the applicability of Glass Fibre Reinforced Polymer (GFRP) industrialized components (profiles) and of innovative materials, such as structural adhesives and solar selective coatings, on windows and curtain walls, is discussed, particularly their degradation mechanisms (durability).
Two different aspects were investigated: the mechanical performance of the GFRP profiles and of the structural adhesives, for their application both on windows stiles and rails and on glass facades mullions; the energy performance of the solar selective coatings, for their implementation on the glass surfaces. The following studies were conducted:

(i) An experimental and numerical study focused on the mechanical performance of GFRP profiles: tensile, torsional and flexural properties were analyzed in different specimens geometry, and the effect of the aging treatment was observed [2].

(ii) An experimental study aimed at the comparison of different adhesives used in GFRP profiles conjunctions: the mechanical performance in shear and tension were analyzed also after the exposition to different aging conditions [3].

(iii) An experimental and analytical study regarded the comparison of different epoxy adhesives used in GFRP-steel profiles conjunctions: the objective was to verify the compatibility of the two materials and the steel contribute to the stiffness increase of GFRP profiles. The verification of the hybridization method was conducted through several mechanical tests and the effects of different aging conditions were observed.

(iv) An experimental and numerical study centered on the degradation phenomena of different types of double glass coating: physical, chemical, optical and energy properties were evaluated after the exposition to different aging conditions [4].

1.2 Literature review

In recent years, in civil engineering, increasing attention has been focused on technologies and innovative materials that allow achieving both excellent mechanical performance and maximum energy efficiency. Furthermore, increasing interest has also been pointed towards technological simplification. The reduction of the number of components leads to numerous advantages: the ease of installation, the saving of production time and the decrease of environmental impacts, thanks to the reduction of production processes and the relative CO_2 emissions [1].

Glass Fibre Reinforced Polymer (GFRP) pultruded profiles are able to fulfill all these requirements, thanks to the combination of high mechanical performance, lightness, good durability in aggressive environments and low thermal and electrical conductivity. Therefore, starting from the end of the 90s, GFRP profiles have been applied to many fields of civil engineering: initially they were implemented on structural members as reinforcing elements while, in recent years, they are used as industrialized components (profiles) and they are employed in bridges, buildings [5], electricity transmission towers [6], and windows frames [7,8]. **The present work is aimed at this latter topic, which includes window and curtain walls.**

Because of the growing use of pultruded profiles in structural applications, the study of the mechanical properties of GFRP profiles is much investigated in the literature. Several studies were carried out to characterize their mechanical properties in un-aged conditions. Flexural [9,10], torsional [11], tensile [12] and compressive [13] properties on small samples were studied also comparing, in some cases [12,13], different geometries. Other studies were focused on full-scale components such as connections [14], profiles [15] or panels [16]. Some of them also surveyed the structural efficacy of building GFRP components coupled to other materials, such as concrete [16,17]. Numerous experiments were performed to compare profiles with different types of the matrix [18,19], demonstrating that the vinyl ester resin has better mechanical properties than the polyester one.

With regard to the durability, different types of accelerated environmental conditions were investigated. The effect of exposing GFRP profiles to UV radiation is mainly confined to few microns of the surface, leading to very small changes in the mechanical properties [19-21].

With regard to the effects of the water on GFRP profiles, some studies demonstrated that the "hot-wet" environment is critical and several types of research have been dedicated to this aspect. Many authors investigated the effects of the immersion in demineralized [19,20,22-26] and salt [19,23-26] water. Some studies also compared degradation under both artificial and natural aging [18,21,25]. However, comprehensive and validated data are still scarce, a large scatter and contrasting data in the results are observed, even if similar methodologies are used.

The aim of the first study (i) of the present work is to evaluate the mechanical response of many GFRP profiles, with a polyester matrix, after exposure under severe humidity level. Dog-bone and squared tubular GFRP profiles were exposed for six months in a climatic chamber, at the constant temperature of 40° C and relative humidity of 98-100 %. During the exposure in the climatic chamber, the weight variation due to water absorption was measured. Tensile, torsional and flexural tests were performed after the exposure period and compared with those obtained from un-aged profiles.

Despite the several beneficial properties, if compared to steel, composite materials present some disadvantages. GFRPs are profiles with a high fiber content and their mechanical properties depend on the orientation of the fibers. This orthotropic nature necessarily requires the availability of data on mechanical properties that nowadays are still lacking [27]. Moreover, they present the difficulty of realizing bolted joints: bolting, in fact, is not a material-adapted way to connect [31], because adherents are subjected to drilling operations that cut the fibers. In this case, adhesive connection represents the most efficient joining method, leading to a uniform load transfer [32-34]. **In the Full Glass window, the mobile frame is composed of four GFRP profiles connected through the bonding technique.** However, this kind of connection is strongly influenced by environmental conditions, which can reduce mechanical properties of the adhesives.

Adhesively bonded joints formed the subject of several types of research. The mechanical behavior [32], failure modes [35-38] and the effect of the joint geometry on the structural response [39-41] were investigated. Regarding environmental effects, most of the studies focused on adhesively-bonded joints for aerospace and automotive engineering, nonetheless there are some papers that shifted their attention to the civil engineering field. For example, Zhang et al. [33,42] demonstrated that high temperatures lower the mechanical performance of bonded joints, especially when the glass transition temperature of the adhesive is reached. This phenomenon is even more pronounced with high humidity levels.

However, validated data about the properties of adhesives used to connect pultruded materials are still scarce. Furthermore, there is a lack of understanding of the aging degradation mechanisms suffered by different types of adhesives used in GFRP joints.

The aim of the second study (ii) of the present work is to compare the mechanical behavior of pultruded GFRP joints, bonded with different types of adhesives, under both un-aged and aged conditions. Six different types of adhesives were investigated: two epoxies, one acrylic, one methacrylate and two polyurethane adhesives. Single lap and butt joints were loaded up to failure, and the results obtained from unaged specimens were compared with

those subjected to cyclic accelerated exposure to moisture, low and high temperatures, and ultraviolet (UV) radiation.

The GFRP profiles, in comparison with steel, present the further disadvantage of the low elastic modulus (up to ten times lower) [43-46], and the consequent high deformability in loading conditions. Therefore, **this feature impedes the applications of GFRP pultruded materials in structures with large spans** [47-49]**, especially when small profiles size is required, such as in curtain walls.**
For this reason, it is necessary to develop suitable approaches to improve the stiffness of the GFRP pultruded material, and some authors demonstrate that coupling GFRP profiles with higher mechanical performances materials – i.e. hybridization system - is an advantageous method [43,50,51].
Kim and Lee [45] developed a steel-reinforced hybrid GFRP deck panel for temporary bridges. The results confirmed that the flexural stiffness of the GFRP deck panel was effectively increased by the proposed methods of hybridization. Wu et al. [43] explored two strengthening methods to improve the bearing capacities of GFRP pultruded SHS sections, by bonding alternatively CFRP plates and steel sections on the external surfaces of the GFRP profiles. Both the strengthening methods demonstrated considerable enhancement of the bearing capacities, respectively of 70 % and of 200 %.
Therefore, it was demonstrated that the use of the steel allows increasing the mechanical performance of the GFRP material. However, to the authors knowledge, validated data for designers are still scarce and there has been little research on the comparison of different types of adhesives used for the joining of GFRP and steel profiles. Most of the existing studies examine the behavior of only one adhesive used to connect GFRP decks to steel girders and were not focused on the improving of the GFRP profiles stiffness [52-55]. Furthermore, the evaluation of the influence of environmental aging was not presented, even if it is well known that bonding connections are strongly influenced by environmental conditions, which can reduce mechanical properties of the adhesives [2,33,42].

In the third study (iii) of the present work, an experimental campaign on the connection of GFRP pultruded profiles and steel laminates through three different epoxy adhesives is proposed. The objective is to investigate three different aspects. The first is the compatibility of the bonding system, through shear tests conducted on small-scale specimens (GFRP-steel single lap joints), particularly the effects of two environmental aging. The second is the response to the local stresses of the bonding system, through puncture resistance tests on full-scale specimens (GFRP-steel squared tubular short profiles) which simulate the local stress transmitted by the curtain panels bolted to the structural members; the effects of two environmental aging is also carried out. The third is the response to flexural stresses of the bonding system, through three-point bending tests on full-scale specimens (GFRP-steel squared tubular long profiles) which simulate the flexural stresses, undergoes by the whole structural members in curtain walls (i.e. the wind load).

Recently, the energy saving standards (legislation 2012/27/UE) have imposed the super insulation of the external walls, completely devolving to the windows the thermal

exchanges between indoor and outdoor. The glass surfaces should satisfy contrasting requirements: optimize the solar gains in the winter season, avoid the heat dispersion and, at the same time, prevent overheating in summer. All these functions can be achieved by multifunctional coatings, such as low-emissivity, solar control, anti-reflectance, UV absorbance films [56-58]. **These devices are commonly applied on the window and curtain walls glazing surfaces, to which this work is addressed.**
Silver is one of the most used metal element in coatings, thanks to its electrical properties, which prevent the heat entrance. It is usually combined with other doping metals characterized by high optic properties, as zinc, tin, and indium [59-61]. However, it is established in the literature that silver-based coatings are not so durable against moisture, which could cause degradation phenomena during transport and storage phases [62,63]. Ando and Miyazaki [64] correlated the lack of durability of silver-based coatings to the moisture-induced migration of the silver. The same authors showed that the combination of silver with other metal elements improves the coatings durability [63,65-67] and other research studies demonstrated that the degradation could be lowered by replacing silver with tin or copper [62,68].
Results on the durability of coatings made up of metals, other than silver, are very scarce in literature even if some authors stressed the importance of this topic [69].

The objective of the fourth study (iv) of the present work is the evaluation of the degradation phenomena occurring on different types of several coatings subjected to hot-wet and salt-spray environments. In the experimental phase, physical, chemical and optical decay were analyzed. In the numerical phase, the samples were compared in terms of energy consumption, comfort levels, and environmental impact, also considering the effort of the performance decay.

1.3 References

[1] P. Munafò. Considerazioni sulle tematiche di ricerca del Settore Scientifico Disciplinare di Architettura Tecnica. *Colloqui.AT.e* Artec (2015) 21-24

[2] F. Stazi, M. Giampaoli, L. Nisi, M. Rossi, P. Munafò. Mechanical performance reduction of GFRP specimens with polyester matrix exposed to continuous condensation. *Composites Part B* 99 (2016) 330-339

[3] Stazi F, Giampaoli M., Rossi M, Munafo P. Environmental ageing on GFRP pultruded joints: Comparison between different adhesives. *Composite Structures* 133 (2015) 404–414

[4] F. Stazi, M. Giampaoli, F. Tittarelli, C. Di Perna, P. Munafò. Durability of different glass coatings in humid and saline environments, ageing impact on heat-light transmission and thermal comfort. *Building and Environment* 105 (2016) 210-224

[5] Keller T. Recent all-composites and hybrid fibre-reinforced polymer bridges and buildings. *Progress in structural engineering and materials* 3 (2001) 132–140

[6] Godat A, Légeron F, Gagné V, Marmion B. Use of FRP pultruded members for electricity transmission towers. *Composite Structures* 105 (2013) 408-421

[7] Appelfeld D, Hansen C. S, Svendsen S. Development of a slim window frame made of glass fibre reinforced polyester. *Energy and Buildings* 42 (2010) 1918-1925

[8] Dispenza C, Pisano A. A, Fuschi P. Numerical simulations of the mechanical characteristics of glass fibre reinforced C-profiles. *Composite Science and Tecnology* 66 (2006) 2980-2989

[9] Chacòn Y. G, Paciornic S, d'Almeida J. R. M. Microstructural evaluation and flexural mechanical behavior of pultruded glass fiber composites. *Materials Science and Engineering A* 528 (2010) 172-179

[10] Sà M. F, Gomes A. M, Correia J. R, Silvestre N. Creep behavior of pultruded GFRP elements – Part 1: literature review and experimental study. *Composite Structures* 93 (2011) 2450-2459

[11] Turvey G. J. Torsion test on pultruded GRP sheet. *Composites Science and Technology* 58 (1988) 1343-1351

[12] Keller T, Tirelli T, Zhou A. Tensile fatigue performance of pultruded glass fiber reinforced polymer profiles. *Composite Structures* 68 (2005) 235-245

[13] Bai Y, Vallèe T, Keller T. Delamination of pultruded glass fiber-reinforced polymer composites subjected to axial compression. *Composite Structures* 91 (2009) 66-73

[14] Carrion J. E, LaFave J. M, Hjelmstad K. D. Experimental behavior of monolithic composite cuff connections for fiber reinforced plastic box sections. *Composite Structures* 65 (2005) 333-345.

[15] Feo L, Mosallam A. S, Penna R. Mechanical behavior of web-flange junctions of thin-walled pultruded I-profiles: an experimental and numerical evaluation. *Composite: part B* 48 (2013) 18-39

[16] Bank L. C, Oliva M. G, Bae H-U, Bindrich B. V. Hybrid concrete and pultruded-plank slabs for highway and pedestrian bridges. *Construction and Building Materials* 24 (2010) 552-558

[17] Ascione F, Berardi V. P, Feo L, Giordano A. An experimental study on the long-term behavior of CFRP pultruded laminates suitable to concrete structures rehabilitation. *Composites: Part B* 39 (2008) 1147-1150

[18] Carra G, Carvèlli V. Ageing of pultruded glass fibre reinforced polymer composites exposed to combined environmental agents. *Composite Structures* 108 (2014) 1019-1026

[19] Cabral-Fonseca S, Correia J. R, Rodrigues M. P, Branco F. A. Artificial accelerated ageing of GFRP pultruded profiles made of polyester and vinyl ester resins: characterization of physical-chemical and mechanical damage. *Strain* 48 (2012)162–173

[20] Correia J. R, Cabral-Fonseca S, Branco F. A, Ferreira J. G, Eusebio M. I, Rodrigues M. P. Durability of glass fibre reinforced polyester (GFRP) pultruded profiles used in civil engineering applications. *Mechanics of Composite Materials* 42 (2006) 325-338

[21] Sousa J. M, Correia J. R, Cabral-Fonseca S. Durability of glass fibre reinforced polymer pultruded profiles: comparison between QUV accelerated exposure and natural weathering in a mediterranean climate. *Experimental Techniques*. 40 (2016) 207-219

[22] Aniskevich K, Aniskevich A, Arnautov A, Jansons J. Mechanical properties of pultruded glass fibre-reinforced plastic after moistening. *Composite Structures* 94 (2012) 2914-2919

[23] Weitsman Y. J, Effects of fluids on polymer composites. A review. *Contract technical report* (1995)

[24] Ben Daly H, Ben Brahim H, Hfaied N, Harchay M, Boukhili R. Investigation of Water Absorption in Pultruded Composites Containing Fillers and Low Profile Additives. *Polymer Composites* (2007) 355-364

[25] Girao J. P, M. de Sousa. Durability of GFRP Pultruded Profiles made of Vinylester Resin M.Sc. Dissertation Extended Abstract. October (2011)

[26] Liao K, Schultheisz C.R, Hunston D.L. Effects of environmental aging on the properties of pultruded GFRP. *Composites, Part B* 30 (1999) 485-493

[27] Turvey G. J. Testing of pultruded glass fibre-reinforced polymer (GFRP) composite materials and structures. Woodhead Publishing Series in *Civil and Structural Engineering* (2013) 440–508

[28] Sonti S. S, Barbero E. J. Determination of shear properties for RP pultruded composites. *Journal of Reinforced Plastics and Composites* 14 (1995) 390-401

[29] Ogasawara T, Yokozeki T, Onta K, Ogihara S. Linear and nonlinear torsional behavior of unidirectional CFRP and GFRP. *Composite Science and Technology* 67 (2007) 3457-3464

[30] Ascione F, Lamberti M, Razaqpur G. Modifications of standard GFRP sections shape and proportions for improved stiffness and lateral-torsional stability. *Composite Structures* 132 (2015) 265-289

[31] de Castro J, Keller T. Ductile double-lap joints from brittle GFRP laminates and ductile adhesives, part I: experimental investigation. *Composite: part B* 39 (2008) 271-281

[32] Keller T, Tirelli T. Fatigue behavior of adhesively connected pultruded GFRP profiles. *Composite Structures* 65 (2004) 55-64

[33] Zhang Y, Vassilopoulos A. P, Keller T. Environmental effects on fatigue behavior of adhesively-bonded pultruded structural joints. *Composite Science and Technology* 69 (2009) 1022-1028

[34] de Castro J. Experiments on double-lap joints with Epoxy, polyurethane and ADP adhesives. *Composite Construction Laboratory, Appendix B* – Technical Report n. CCLab2000.1 b/2

[35] Zhang Y, Vassilopoulos A. P, Keller T. Fracture of adhesively-bonded pultruded GFRP joints under constant amplitude fatigue loading. *International Journal of Fatigue* 32 (2010) 979-987

[36] Zhang Y, Keller T. Progressive failure process of adhesively bonded joints composed of pultruded GFRP. *Composite Science and Technology* 68 (2008) 461-470

[37] Lee H. K, Pyo S. H, Kim B. R. On joint strength, peel stresses and failure modes in adhesively bonded double-strap and supported single-lap GFRP joints. *Composite Structures* 87 (2009) 44-54

[38] Shahverdi M, Vassilopoulos A. P, Keller T. A phenomenological analysis of mode I of adhesively-bonded pultruded GFRP joints. *Engineering Fracture Mechanics* 78 (2011) 2161-2173

[39] Vallèe T, Correia J. R, Keller T. Probabilistic strength prediction for double lap joints composed of pultruded GFRP profiles part I: experimental and numerical investigations. *Composite Science and Technology* 66 (2006) 1903-1914

[40] Vallèe T, Correia J. R, Keller T. Optimum thickness of joints made of GFRP pultruded adherends and polyurethane adhesive. *Composite Structures* 92 (2010) 2102-2108

[41] Vallèe T. Adhesively bonded lap joints of pultruded GFRP shapes. Thèse n. 2964 (2004)

[42] Zhang Y, Vassilopoulos A. P, Keller T. Effect of low and high temperatures on tensile behavior of adhesively-bonded GFRP joints. *Composite Structures* 92 (2010) 1631-1639

[43] Wu C, Bai Y, Zhao X-L. Improved bearing capacities of pultruded glass fibre reinforced polymer square hollow sections strengthened by thin-walled steel or CFRP. *Thin-Walled Structures* 89 (2015) 67–75

[44] Haoa Q, Wangb Y, Oua J. Design recommendations for bond between GFRP/steel wire composite rebars and concrete. *Engineering Structures* 30 (2008) 3239-3246

[45] Kim H-Y, Lee S-Y. A steel-reinforced hybrid GFRP deck panel for temporary bridges. *Construction and Building Materials* 34 (2012) 192–200

[46] J. Qureshi, J. T. Mottramb. Behaviour of pultruded beam-to-column joints using steel web cleats. *Thin-Walled Structures* 73 (2013) 48–56

[47] Wu C, Bai Y. Web crippling behavior of pultruded glass fibre reinforced polymer sections. *Composite Structures* 108 (2014) 789–800

[48] Borowicz DT, Bank LC. Behavior of pultruded fiber-reinforced polymer beams subjected to concentrated loads in the plane of the web. *Journal of Composites for Constructions* 15(2) (2010) 229–38

[49] Turvey GJ, ZhangY. Characterisation of the rotational stiffness and strength of web–flange junctions of pultruded GRP WF-sections via web bending tests. *Composites Part A* 37(2) (2006)152–64

[50] Hollaway L.C. A review of the present and future utilisation of FRP composites in the civil infrastructure with reference to their important in-service properties. *Construction and Building Materials* 24 (2010) 2419–2445

[51] Hai N. D, Mutsuyoshi H, Asamoto S, Matsui T. Structural behavior of hybrid FRP composite I-beam. *Construction and Building Materials* 24 (2010) 956–969

[52] Keller T, Gurtler H. Design of hybrid bridge girders with adhesively bonded and compositely acting FRP deck. *Composite Structures* 74 (2006) 202–212

[53] Keller T, Zhou A. Fatigue behavior of adhesively bonded joints composed of pultruded GFRP adherends for civil infrastructure applications. *Composites: Part A* 37 (2006) 1119–1130

[54] Keller T, Schollmayer M. Through-thickness performance of adhesive joints between FRP bridge decks and steel girders. *Composite Structures* 87 (2009) 232–241

[55] Schollmayer M, Keller T. Modeling of through-thickness stress state in adhesive joints connecting pultruded FRP bridge decks and steel girders. *Composite Structures* 90 (2009) 67–75

[56] C. G. Granqvist. Transparent conductors as solar Energy materials: A panoramic review. *Solar Energy Materials & Solar Cells* 91 (2007) 1529-1598

[57] M.C. Singh, S.N. Garg. R. Jha. Different glazing systems and their impact on human thermal comfort-Indian scenario. *Building and Environment* 43 (2008) 1596-1602

[58] D. Li, F. Huang, S. Ding. Sol-gel preparation and characterization of nanoporous ZnO/SiO2 coatings with broadband antireflection properties. *Applied Surface Science* 257 (2011) 9752-9756

[59] D. R. Sahu, J. Huang. High quality transparent conductive ZnO/Ag/ZnO multilayer films deposited at room temperature. *Thin Solid Films* 515 (2006) 876-879

[60] K.H. Choi, J.Y. Kim, Y.S. Lee, H.J. Kim. ITO/Ag/ITO multilayer films for the application of a very low resistance transparent electrode. *Thin Solid Films* 341 (1999) 152-155

[61] G. Leftheriotis, S. Papaefthimiou, P. Yianoulis. Integrated low-emittance-electrochromic devices incorporating ZnS/Ag/ZnS coatings as transparent conductors. Solar Energy Materials & Solar Cells 61 (2000) 107-112

[62] M. Okada, M. Tazawa, P. Jin, Y. Yamada, K. Yoshimura. Fabrication of photocatalytic heat-mirror with TiO2/TiN/TiO2 stacked layers. *Vacuum* 80 (2006) 732-735

[63] E. Ando, M. Miyazaki. Durability of doped zinc oxide/silver/doped zinc oxide low emissivity coatings in humid environment. *Thin Solid Films* 516 (2008) 4574-4577

[64] E. Ando, M. Miyazaki. Moisture degradation mechanism of silver-based low-emissivity coatings. *Thin Solid Films* 351 (1999) 30-312

[65] M. Miyazaki, E. Ando. Durability improvement of Ag-based low-emissivity coatings. *Journal of Non-Crystalline Solids* 178 (1994) 245-249

[66] E. Ando, S. Suzuki, N. Aomine, M. Miyazaki, M. Tada. Sputtered silver-based low-emissivity coatings with high moisture durability. *Vacuum* 59 (2000) 792-799

[67] E. Ando, M. Miyazaki. Moisture resistance of the low-emissivity coatings with a layer structure of Al-doped ZnO/Ag/ Al-doped ZnO. *Thin Solid Films* 392 (2001) 289-293

[68] D.R. Sahu, J. Huang. Characteristics of ZnO/Cu/ZnO multilayer films on copper layer properties. *Applied Surface Science* 253 (2006) 827-832

[69] A. Cannavale, F. Fiorito, M. Manca, G. Tortorici, R. Cingolani, G. Gigli. Multifunctional bioinspired sol-gel coatings for architectural glasses. *Building and Environment* 45 (2010) 1233-1243

Chapter 2

The results of the research: the patents

In recent years, the research group designed and patented the *Full Glass* window frame (patent n. PCT/IB2014/066098) and the *Structural Member* for curtain walls (patent application n. 102015000087569), high-performance and easy to assemble components made of GFRP pultruded profiles, structural adhesives and solar selective glass coatings. The use of these materials, characterized with higher mechanical and thermal performance than the traditional ones, allowed the design of construction elements with less pieces and, consequently, the reduction of CO_2 emissions during the entire life cycle of the products, from the production to the disposal phase. The basic principle, named "Technological Simplification" represents the new concept of environmental sustainability. In the following sections, the patented construction elements are presented.

2.1 The patent "Serramento per finestra"

2.1.1) State of the art

Traditional fixed and mobile windows frames usually have large sizes, thus affecting the design and the performance of the windows, especially the thermal properties. Furthermore, the elevated number of their components have a significant negative influence on energy consumptions, both in the production and in the disposal phases.
The objective of the *Full Glass* window patent design, named "Serramento per finestra", is the resolution of these issues.

2.1.2) The registered patent: PCT/IB2014/066098

Full Glass is an innovative window that is elegant, lightweight and transparent. Simultaneously, this window has high mechanical strength, thermal insulation, and durability properties.
The small frame "disappears" from the outside view: in fact, thanks to excellent mechanical properties of the glass fiber reinforced pultruded (GFRP) profiles, it is entirely positioned within the double-glass cavity. The GFRP fixed frame is mainly within the exterior walls:

the result is a full-glazed elegant window. Furthermore, the fixed frame can be connected with an existing one.
Full Glass is a very flexible system: all the accessories (movement systems and gaskets) are within the standard double-glass cavity and could be chosen according to every design choice. Furthermore, the system it suitable to several environmental conditions. The frame and the glass are adhesively connected and the type of adhesive may vary according to different operative temperatures, to ensure the maximum performance of the system.
The combination of the low thermal conductivity of GFRPs with the double-glass system, which can be with the triple-glazed window, led to very high thermal performances. The use of solar selectivity glass coatings can further improve the thermal behavior.
Pultruded profiles demonstrate excellent resistivity to environmental exposures, therefore, the system is very durable and requires low maintenance costs.
The invention leads to a considerable technological simplification: *Full Glass* window, in fact, is made up of a limited number of simplified profiles, allowing a fast and easy assembly.

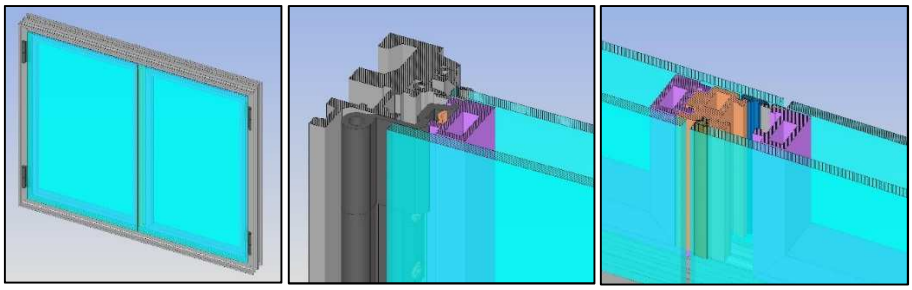

Figure 2.1. Full Glass 3d views overall view, mobile-fixed frames conjunction; shutters closing system.

2.1.3) Product information

Double-glazing alternative dimensions
6/30/6(4)
6/24/6(4)*
6/12/4/12/6(4)
*in this case, special movement systems are required.

Joint type
Open

Number of profiles
Fixed frames: 2
Mobile frames: 2

Sliding frame: 2
Fixed frame connected with an existing one: 2

Opening systems
Two-wing
Overturned
Sliding

Handling systems
European
R-40

2.2 The patent “Montante per facciate continue”

2.2.1) State of the art

The structural frames of traditional curtain walls are usually made of aluminum and, as occurs in windows, the use of this material has a negative impact on both the design and the thermal property, due to the large size and the high thermal conductivity of the frames. Furthermore, the elevated number of components constituting the construction elements causes very high CO_2 emissions during all the curtain walls life cycle.
The objective of the *Structural Member* patent design, named “Montante per facciate continue”, is the resolution of these issues.

2.2.2) The patent application n. 102015000087569

The *Structural Member* is a linear construction element which, with reduced sections (from 55x55 mm^2 to 110x110 mm^2), allows the realization of curtain walls with high glazing areas. Panels of different sizes and materials can be used since the *Structural Member* presents both high load carrying capacity and stiffness, such as to keep deformations to a minimum. Furthermore, it is made of GFRP pultruded profiles, an energy saving material, which is also very durable against environmental aging. The application of the construction element is very easy.
The innovative principle consists of the use of GFRP profiles, with small sectional areas, linked to pre-tended steel wires. The *Structural Member* can be used to realize curtain walls with high glazing areas (max 3,5÷4 ml), thereby guaranteeing a seal against air and water and a good thermal insulation.
Furthermore, the *Structural Member* offers great versatility: it can be used to carry panels of different sizes and material (glass, wood, aluminum, etc.), allowing the assembly of opaque and transparent surfaces both in vertical and horizontal positions, in addition to different inclinations. It can also be used in existing buildings, in every roofs configuration.

Pultruded profiles demonstrate excellent resistivity to environmental exposures therefore the system is very durable and benefits from low maintenance costs.
This construction element allows a noticeable simplification of the production and assembly phases since it is made of a limited number of components, with simple geometries.

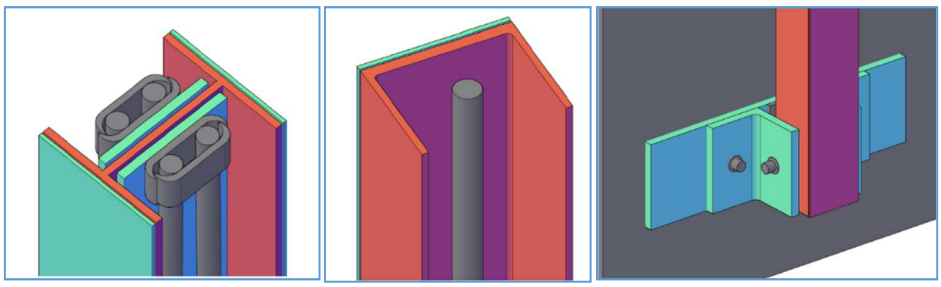

Figure 2.2. "Structural Member" 3d views: double T-section, C-section and the connection to the slab.

2.2.3) Product information

The *Structural Member* includes:
- GFRP profiles with different sections (C and double T) with areas less than 90x90 mm^2;
- steel laminates bonded to GFRP profiles with the objective of tightening the composite profiles and to facilitate the fixing of the panels;
- one or more pre-tended steel wires linked to the GFRP profile through several terminals, with the objective of containing deformations. The steel wires allow to reduce the member's length of free inflection on every occasion. The ends of the steel wires are connected to the building's structure through forks.

The *Structural Member* is linked to the building's structure (slabs) through connection systems readily available on the market (corner guides Halfen, etc.).

2.3 List of figures

Chapter 3

On GFRP small samples and full-scale profiles: mechanical performance before and after the ageing treatment

The aim of the present study is to evaluate the mechanical performance of GFRP pultruded profiles subjected to a continuous condensation environment, for they application on windows and curtain walls. The contents of this chapter were published in a previous work: *"Mechanical performance reduction of GFRP specimens with polyester matrix exposed to continuous condensation"* [1].

3.1 Abstract

In this experimental study, GFRP small specimens and full-scale profiles with polyester matrix were exposed for six months to a constant temperature of 40 °C and relative humidity of 98-100 %. The trend of absorption during the ageing treatment was evaluated and, after the exposure period, the mass increment and mechanical properties of aged specimens were compared to un-aged ones. Tensile tests were conducted on dog-bone geometries with different fibre orientations (0°, 45° and 90°), while squared tubular profiles were employed in flexural and torsional tests. The trend of absorption was found to be pseudo-Fickian and the weight increment was very similar for all the tested samples. The artificial ageing reduced the mechanical properties in the matrix dominant direction of GFRP profiles. In tensile tests, the ageing treatment produced different effects depending on specimen fibre orientations: the lowest strength and elastic modulus reductions (respectively of about 4 and 5 %) were registered by those specimens tested along the direction of fibres (0°), which are only moderately affected by moisture and heat. The same failure modes in tension, before and after ageing, were observed for all fibre directions. Both torsional and flexural properties resulted to be significantly decreased (8 %). In these latter loading types, the aged matrix is more involved in the failure mechanisms and this was confirmed by the failure modes that after ageing showed more evident fractures.

3.2 Introduction

Because of the growing use of pultruded materials in civil engineering, the study of GFRP profiles is much investigated in the literature. Several studies were carried out to characterize their *mechanical properties* in un-aged conditions [2-6], also comparing different sizes, geometries [7-9], and types of the matrix [10,11].
Regarding the *durability* aspect, some authors demonstrated that UV radiation leads to very small changes in the GFRP profiles mechanical properties [11-13]. Several studies have been dedicated to the effects of the moisture [10-18], but comprehensive and validated data are still scarce, and a large scatter and contrasting data in the results are observed, even if similar methodologies are used. Table 3.1 summarizes what have been found by various authors in terms of water gain and mechanical properties of aged GFRP profiles. Rather different results are obtained, showing the difficulty of evaluating unanimous values for the properties of aged GFRP profiles.

The aim of the present study is to evaluate the resistance to the high humidity level of GFRP pultruded profiles. An experimental campaign on the mechanical response of many GFRP specimens, with a polyester matrix, after exposure under severe humidity level, was carried out. *Dog-bone* and *squared tubular* GFRP profiles were exposed for six months in a climatic chamber, at the constant temperature of 40° C and relative humidity of 98-100 %. During the exposition in the climatic chamber, the weight variation due to water absorption was measured. Tensile, torsional and flexural tests were performed after the exposure period and compared with those obtained from un-aged profiles.

Table 3.1. Weight (W), tensile (σ) and flexural (F) results of GFRP specimens, subdivided into polyester and vinyl ester matrix, exposed to the wet environment at different temperatures. Comparison among different authors.

Type of matrix	*Ref.*	*Ageing conditions*	*T* (°C)	*Duration* (h)	*Curve*	*W gain* (%)	*σ decrease* (%)	*F decrease* (%)
Polyester	[11]	Immersion	20	8100	A	1.3 (1)[a]	8 (15)[a]	2 (4)[a]
			40		A	1.3 (1)[a]	18 (20)[a]	18 (10)[a]
			60		D	0.7 (0.7)[a]	40 (35)[a]	30 (35)[a]
		Condensation	**40**	6480	LF	1.3 (1.3)[a]	30 (25)[a]	16 (10)[a]
	[12]	Immersion	20	6480	A	0.3	/	16
		Condensation	60	6480	LF	0.3	/	19
		Cycles of water spray + UV	65	2000	-	0	13	7
	[13]	Cycles of water spray + UV	60	3000	/	/	21	22
	[14]	Immersion	20	14400	A	1.3(1.3)[a]	3	16.5
			66	900	D	1.3 (1.3)[a]		
	[15]	Immersion	**40**	/	B	/	/	/
		Condensation	**32**	/	A/B	/	/	/
Polyester +additives	[16]	Immersion	5÷25	2880	LF	0.02÷0.5	/	/
			65÷85		A	0.5÷1.6		
Vinyl ester	[11]	Immersion	20	8100	A	0.5 (0.4)[a]	0 (5)[a]	18 (20)[a]
			40		A	0.5 (0.4)[a]	10 (10)[a]	20 (23)[a]
			60		A	0.7 (0.65)[a]	38 (20)[a]	42 (30)[a]
		Condensation	**40**	6480	LF	0.5 (0.5)[a]	10 (5)[a]	22 (17)[a]
	[13]	Cycles of water spray + UV	60	3000	/	/	3	13
	[17]	Immersion	20	17280	A	0.5 (0.4)[a]	10 (8)[a]	20 (20)[a]
			40		A	0.6 (0.4)[a]	10 (0)[a]	28 (23)[a]
			60		D	0.8 (0.7)[a]	38 (23)[a]	48 (31)[a]
		Condensation	**40**	9000	LF	0.8 (0.7)[a]	8 (0)[a]	28 (19)[a]
	[18]	Immersion	25	3900	A	0.7 (0.6)[a]	29 (9120h)	4.8
			75	2400	D	0.7 (0.7)[a]		40

The values with bold format refer to the similar ageing conditions adopted in the present study.

[a] The values in brackets refer to the mechanical properties of profiles at extrapolated 2340 hours (6 months), to make a comparison with those obtained in the present study.

3.3 Experimental methods

3.3.1) Materials

The studied material is a pultruded E-glass fibre reinforced polyester composite (supplied by Fibrolux, Germany), adopted for its widespread use. It is made of alternating layers of unidirectional fibre roving and chopped strand mat embedded in the polyester matrix. A polyester surface veil was used to protect the profiles against environmental actions.

3.3.2) Artificial ageing

The environmental aging exposure was simulated according to ISO 6270-2:2005 [19], using a climatic chamber "Angelantoni" CST-130 S model, equipped for this purpose. A total number of twenty-seven profiles, fifteen dog-bone specimens and twelve squared tubular (Figure 3.1) were aged. All were exposed to a constant air temperature of 40 °C and a relative humidity of 98-100 %. The exposure period was selected referring to the findings of other authors [11] that showed a high rate of strength decrease in the first six months and a subsequent stabilization for longer periods.
The profiles were set at an angle of 60 ° with respect to the horizontal plane to permit drainage of condensed water. Precautions were taken to ensure that no condensation water was allowed to drip onto the test specimens, neither from the walls or ceiling of the climatic chamber nor from other specimens. The distance from the walls was 100 mm, the distance from the surface of the water was 250 mm and the spacing between specimens was 20 mm.
Prior to testing, specimens were removed from the climatic chamber and immediately tested, without any further conditioning. Other authors adopted this type of procedure [14,17].

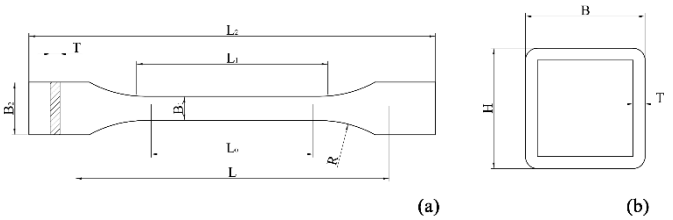

Figure 3.1. Geometries of tested specimens: dog-bones (a) and squared tubular (b) profiles.

3.3.3) Water absorption test

The aim of this experimental phase was to evaluate the water absorption of pultruded profiles due to environmental aging.

One of the main responsible of the mechanical properties degradation is water. The moisture uptake is considered an indication of the possible imparted damage, due to matrix cracks and detachment at the interface between fibres and matrix. It has also been observed that the rate of moisture absorption at elevated temperatures is higher than at ambient temperature [12,14,16,18].
Therefore, referring to others authors [10,12,18], a preliminary evaluation of the effects of the relative humidity and temperature within the climatic chamber has been performed. Five dog bone specimens (with 0° fibre direction) were weighted eight times during the artificial ageing, while the mass gain of the twelve tubular specimens was only registered before and after the ageing treatment.
Specimens were carefully wiped to remove any superficial condensation and then weighed using an electronic balance (with an accuracy of 10^{-4} g) to monitor the mass change during the ageing process. The percentage of weight gain *W* with respect to the un-aged materials was calculated as:

$$W=[(m(t)-m(0))/m(0)]x100 \quad (1)$$

being *m(0)* and *m(t)* respectively the specimens mass [g] at the initial state and at the time [t].
The results were compared with the categories drawn by Weitsman [15] in Figure 3.2.
Curve LF represents the linear Fickian behaviour, where the trend of absorption gradually attains equilibrium after a rapid initial take off. The other curves show variations from the ideal Fickian trend. Curve A is called pseudo-Fickian behaviour and represents a moisture weight gain that never reaches equilibrium, due to the phenomena of polymer relaxation. Curve B is a two-stage diffusion process with an abrupt jump after the initial bilinear trend, generally attributed to the change of temperature, applied load or relative humidity. Curves C and D are usually associated with irreversible damage and degradations. In curve C, the rapid moisture weight gain depends on large deformations or damage in the material, for example, fibre/matrix debonding and matrix cracking. In curve D, the loss of material integrity can be ascribed to irreversible chemical or physical breakdown of the material.

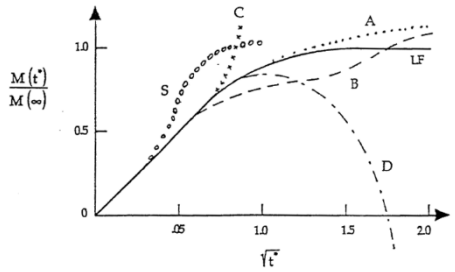

Figure 3.2. Schematic curves representing different categories of recorded weight-gain absorption data in polymers and polymeric composites reported by Weitsman [15].

3.3.4 Mechanical tests

The aim of this experimental phase was to evaluate tensile, torsional and flexural properties of pultruded profiles before and after ageing. Figure 3.1 shows the geometries of tested specimens while the dimensions are listed in Table 3.2.

Table 3.2. Test program.

Profiles	***Mechanical test***		***Un-aged***	***Aged***	***Geometries*** (mm)	
Dog-bones	Tensile	0°	5	5	B_1= 10; B_2= 20 L = 115; L_0 = 50;L_1 = 60; L_2= 160 T= 5; R= 60	
		0°	5	5	B_1= 5; B_2= 10	
		45°	5	5	L= 28; L_0 = 12; L_1= 15; L_2= 40	
		90°	5	5	T= 5; R= 30	
Squared tubular	Flexural		8	8	L_{tot}= 600	B=50 H=50 T=5
	Torsional		4	4	L_{tot}= 400	

Tensile tests were performed according to ISO 527-4:2012 [20] using a "dog-bone" shape.
In order to investigate GFRP profiles tensile properties along further fibre orientations, tests on specimens with reduced size (see Table 3.2), cut at 45° and 90° with respect to the fibre direction were performed. Such reduced size was necessary because of the width of the GFRP profile, which is only 50 mm. In order to check the reliability of such unconventional samples, five reduced samples even for 0° direction were tested and compared to the ones with standard size (see *Section 3.4.5*). In summary, forty specimens were cut out from squared tubular profiles (50x50x600 mm) and were manufactured under ambient laboratory conditions. All samples were tested with a speed of 2 mm/min and loaded up to failure on a Zwick/Roell Z050 testing machine of 50 kN capacity. The elongation of the specimens was measured by an extensometer.

Torsional tests were carried out according to Turvey [4,21] using squared tubular profiles. Eight specimens were tested using a tensile/torsion machine able to apply a maximum torque of 1000 Nm and unlimited rotation. This machine was developed for testing steel specimens in combined tension and torsion loads [22]. In this case, special steel cuff grips were developed to adapt the squared tubular GFRP profiles to the testing machine (Figure 3.3). The specimen free length between the edges was 300 mm. The rotation was applied with a rate of 0.2°/sec. Thereafter the rotation was applied up to the failure of the specimens.

Flexural tests were carried out according to EN 13706-2:2002 [23] using squared tubular profiles. Sixteen specimens were tested through a three-point bending test with a span length of 500 mm; the diameter of the loading member was 10.8 mm. Profiles were tested

with a speed of 2 mm/min and loaded up to failure on a Zwick/Roell ZMART.PRO testing machine of 600 kN under displacements control.

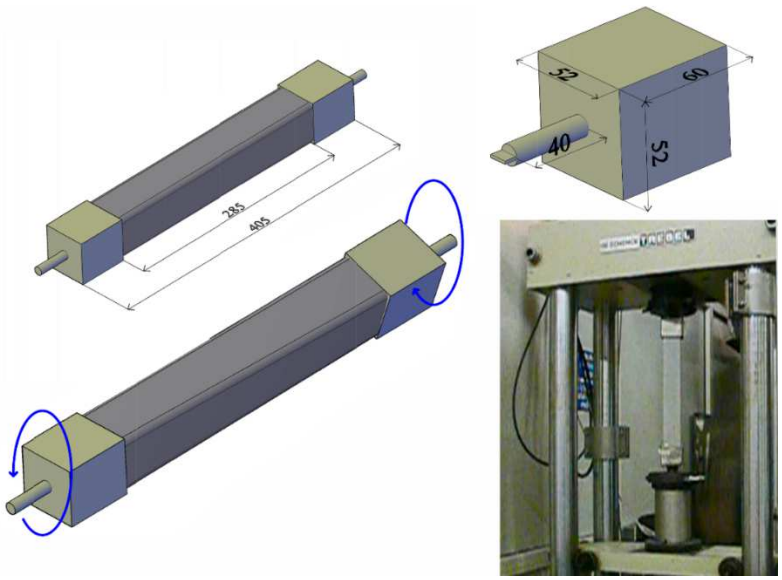

Figure 3.3. The configuration of the torsional test setup: squared tubular profiles with special steel cuff grips and tensile/torsion machine.

3.4 Results and discussion

3.4.1) Water absorption

Figure 3.4 reports the experimental weight-gain curve as a function of the square root of the immersion time normalized to the sample's thickness ($\sqrt{t}/h$), which represents the mean data obtained using five specimens. In the first 5 days, the weight increment follows a linear trend, with a total absorption of 0.32 %. In this initial phase voids and free volumes were filled up and no cracking occurred, as hypothesized by Ben Daly et al. [16]. Between days 5 and 77 a similar increment of absorption was obtained (0.31 %), with a lower curve slope. In this period, a two-stage diffusion process was observed, whit a slight jump in the moisture weight gain, on day 13. In the last ageing period (days 77 to 180), the weight increment was reduced but never reached equilibrium: in fact, the penetration of the water into the polymer matrix induced microstructural variations (the so-called phenomenon of swelling) that caused a relaxation of the polymer structures, leading to further absorption. This phenomenon was well explained in [15]. In summary the trend of absorption throughout the ageing period is

characterized by a slightly fluctuating tendency fitting better with the theoretical curve A. This deviation respect to the ideal Fickian curve could be attributed to the inherent time-dependent response of matrix polymers, which cannot adapt instantaneously to the imposed external environment, even under exposure to constant ambient conditions [15].

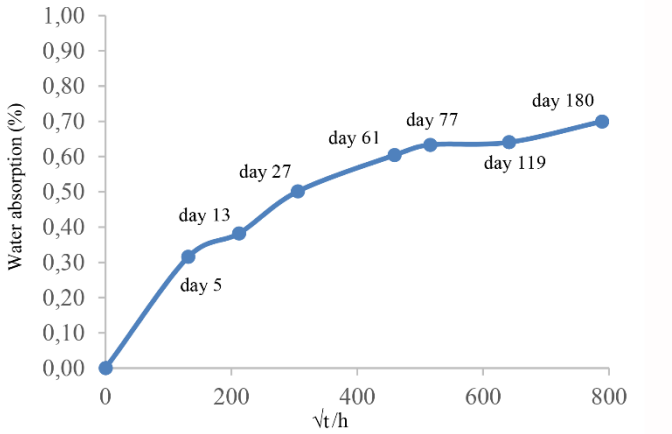

Figure 3.4. Experimental weight-gain curve as a function of the square root of the immersion time normalized to the sample's thickness (√t/h).

The obtained data are consistent with the literature results. As reported in Table 3.1, other authors have shown that the curve of absorption (A, D or LF) is influenced by the ageing temperature, while it does not depend on matrix typology, even if showing a flattened trend with lower weight gain values for vinyl ester composites. For low temperatures (≤25 °C) all the composites (both polyester and vinyl ester) without additives show a pseudo-Fickian behavior (A type), regardless the ageing method (condensation or immersion). For medium-high temperatures (30÷40 °C) almost all composites approach curves A or LF. For high temperatures (≥60 °C) the majority of the authors found instead a trend similar to curve D (with the exception of [12]) where the material exhibits a mass loss. A different behavior is shown by the polyester matrix with the presence of additives: in this case, a Fickian trend (LF type) is observed at low temperatures, changing to pseudo-Fickian (A type) at elevated temperatures. In fact, as explained by some authors [16], the presence of the additives, in particular, low profile additives (LPA), in the polyester matrix, increases the water absorption process at all the immersion temperatures. This is due to the presence of a significant amount of voids in the composite containing this type of additives.
The average total water absorption values (weight-gain) of dog bones and tubular specimens after 6 months is summarized in Table 3.3. For all the sample geometries, the scatter of the data was very reduced, being generally within 1%. The percentage of mass gain is almost similar regardless of the different geometries, as observed by other authors [14]. However

the mean mass increment (0.7 %) is low if compared with the value of 1.3 % reported by Cabral-Fonseca et al. [11], which studied the water absorption of polyester profiles exposed to the same conditions of the present study, i.e. continuous water condensation at 40 °C for 6480 hours (Table 3.1). This discrepancy does not depend on the different duration of the aging periods. Indeed, deducing the mass gains of [11] at 4320 hours from the experimental curve, the water gain maintains the same value of 1.3 %, as the absorption equilibrium was already reached. The different water absorption between the present study and [11] could be instead ascribed to several factors, namely the chemical composition, the morphology and the degree of curing of the polymeric matrix of the composite, as highlighted by [12]. Furthermore, the tested profiles in the present study are characterized by a polyester surface veil in order to prevent water absorption while, in the other study [11], it was not used. It was demonstrated by previous studies that this type of coat has a great influence on the results. Indeed, while some authors stressed that the material surface of the exposed specimens in direct contact with the environment absorbs moisture almost immediately [16], other ones highlighted that the presence of a veil coating protects the specimen making the effect of moisture diffusion negligible [24].

Table 3.3. Average weight-gain results of dog bone specimens and tubular profiles after ageing.

Specimens	***Weight*** (g)		***W gain*** (%)
	un-aged	aged	
Dog-bones	169.17 ± 1.23	170.35 ± 0.98	0.69
Tubular 400	603.80 ± 1.22	608.14 ± 1.47	0.73
Tubular 600	905.20 ± 1.84	911.79 ± 1.94	0.72

3.4.2) Tensile properties

3.4.2.1) Tensile properties of 0˚ specimens with standard dimensions

The variation of the elastic modulus and the tensile strength of specimens with longitudinal fiber (0° inclination) is summarized in Figure 3.5.
Both elastic modulus and tensile strength do not vary significantly after the ageing process, respectively 5.5 % and 4.2 % on average.
The small reduction in tensile properties obtained in the present experiments can be explained observing that, in this case, the fiber are oriented along the loading direction. As observed for instance in [14], fibers, are only moderately affected by moisture and heat, therefore the mechanical properties do not exhibit a large variation. Furthermore, the presence of the polyester surface veil on the specimens surface prevents the water uptake and the consequent reduction of tensile properties. Greatest effects on tensile properties were instead recorded on specimens without the surface veil [11]. In that case, after the same ageing period of 6 months and after the same type of ageing, the tensile strength reduction was about 25 %. The

great incidence of the presence of surface veil could be confirmed by comparing data from studies on similar specimens with and without such coating (respectively [14] and [11]). The former study showed a negligible tensile strength reduction, while the latter obtained a decrement of 8 %. The same observation could be drawn for vinyl ester profiles aged at high temperatures, with [13] and without [11,17] the surface veil.

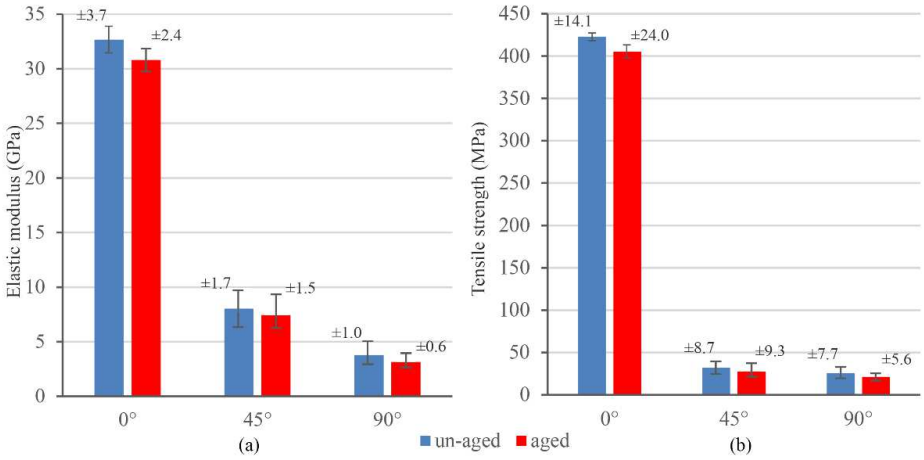

Figure 3.5. Results of tensile tests on specimens with 0˚, 45˚ and 90˚ fiber direction. Variation of the elastic modulus and tensile strength before (a) and after ageing (b).

Before and after the ageing treatment, the failure modes were similar (Figure3.6). Typically, the cracks initiate from defects in the matrix or at the interfaces between the matrix and the fibers, growing subsequently along the fibers [25].

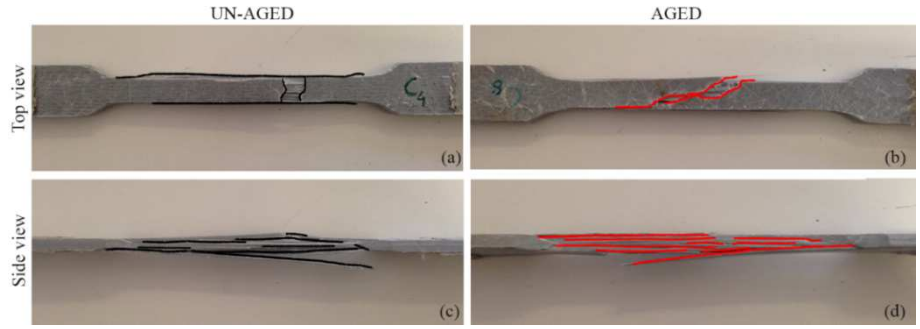

Figure 3.6. Failure modes of specimens with 0° fiber direction, before (a-c) and after (b-d) ageing.

3.4.2.2) Tensile properties of 45° and 90° specimens

The tensile tests on 45° and 90° directions were performed on specimens with a reduced size. This particular size was required because the width of the GFRP profile is only 50 mm. Such geometry is not standard, therefore numerical and experimental studies were carried out to deepen the effect of size dimensions (*Section 3.4.5*).
The results of the tensile tests performed on specimens with fibers inclined at 45° and 90° are summarized in Figure 3.5 in terms of elastic modulus and tensile strength. A reduction of the tensile properties after the ageing treatment was observed. For 45° and 90° samples, the average elastic modulus reduction was about 7 % and 16 %, respectively. Instead, the average tensile strength reduction was about 15 % and 17 %, respectively. In the transverse direction, the artificial ageing produces a larger degradation of the tensile properties, because of the matrix, which is more stressed than fibers in this configuration, is usually more affected by moisture and heat, as pointed out in [10]. To the authors knowledge, no data are available in the literature with regard to 45° direction.
Unfortunately, a large variance was observed in the tests, as remarked by the error bars of Figure 3.5. The variance is much larger than those observed for the 0° samples and seems to be in contrast with the findings of [10], where higher standard deviation were observed for 0° samples rather than for 90° ones. In this case, the variance can be explained by the size effect (see *Section 3.4.5*).
Before and after the ageing treatment, the same failure modes were observed (Figure 3.7) regardless the direction of load application with respect to the fibers. The rupture occurred always along the fiber direction, as for the findings of [25].

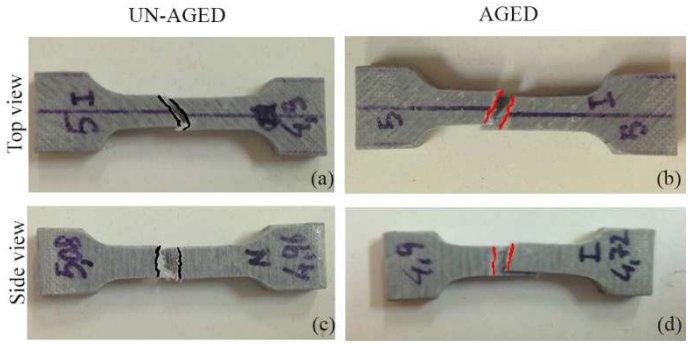

Figure 3.7. Failure modes of specimens with 45° and 90º directions, before (a-c) and after (b-d) ageing.

3.4.3) Torsion properties

The torsional tests were performed on specimens with squared tubular geometry, which is not standard, therefore an FE model was employed to check its reliability, see *Section 3.4.5*. The results of the torsion tests are reported in Figure 3.8. The diagrams show the average torque-rotation response of the specimens before (a) and after (b) artificial ageing. Standard deviation is highlighted by dotted lines and, especially in aged profiles, it increases with the increasing load.
For both aged and un-aged specimens, the response is non-linear over the whole twist range, with a change of slope after 5° of rotation, approximately. The ultimate load registered for aged profiles was on average 8 % lower than the un-aged ones. On average, un-aged tubular specimens were able to accommodate a rotation of about 23° before failure, similar values were observed in aged profiles, with an average rotation of 20° at maximum torque.

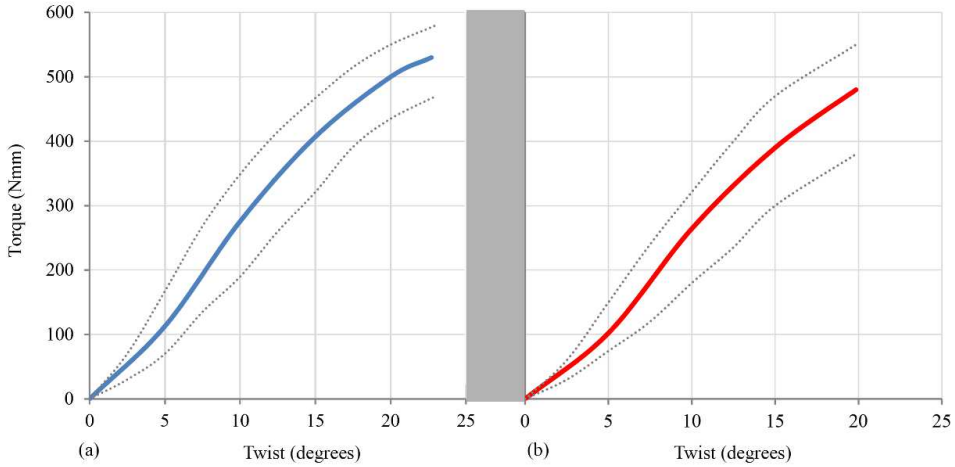

Figure 3.8. Results of torsion tests of un-aged (a) and aged (b) specimens: average values (in bold format) and deviations standard (dashed curves).

From torsional tests, the shear modulus of the GFRP profile could be evaluated using the well-known Bredt-Batho equation for thin walled tubes:

$$G = \frac{T}{\theta}\frac{L}{4A^2}\oint\frac{ds}{t} \tag{2}$$

where T is the torque [Nmm], L is the free length of the tube [mm], θ is the rotation angle [rad], A is the internal area of the section [mm^2] and t is the thickness of the tube [mm].
Here, it is difficult to evaluate the torque value from the experiments because of the observed non-linear behavior in torsion. Looking at the plots of Figure 3.8, the trend has an almost

linear behavior when rotation is between 5° and 10°. In this case, if the Bredt-Batho formula is applied (Eq. 2), an average value of G_{12} = 1.84 GPa was obtained for the un-aged profiles and a value of G_{12} = 1.78 GPa for the aged ones. Therefore, according to these results, the ageing does not produce a significant variation in the shear properties (3 %).
To the authors knowledge, only few research works were dedicated to GFRP profiles tested in torsion before and after the ageing treatment. Furthermore, most of the available studies investigate un-aged rectangular strip specimens [4,21] rather than squared tubular profiles.
With regards to failure modes (Figure 3.9), a crack along one of the corners between web and flanges (Figure 3.9 a-b) was observed for each profile before and after the ageing treatment. However, in the section at the end of profiles (Figure 3.9 c-d), more than one crack occurred in the joining zone, especially in aged profiles.

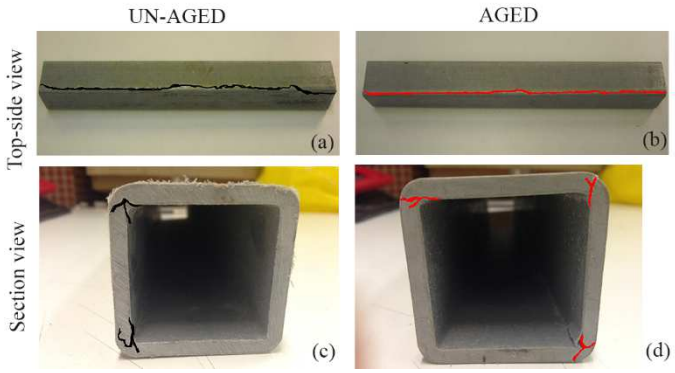

Figure 3.9. Specimens failure modes, before (a-c) and after (b-d) ageing.

3.4.4) Flexural properties

The results of the bending tests are reported in Figure 3.10. The diagrams show the load-displacement response of the specimens before (a) and after (b) artificial ageing.
In both un-aged and aged conditions, there is a great dispersion in the results: this is probably due to the lack of homogeneity caused by the pultrusion process [26]. However, the mean curves plotted in bold format, highlighted an almost bilinear elastic behavior prior to failure, with very similar trends. This is a typical characteristic of the GFRP material when subjected to flexural stresses [26-28].
The failure load for aged profiles was, on average, lower than un-aged ones of about 8% (on average respectively 12.89 kN and 13.96 kN). In bending tests, both fibers and matrix are stressed, and the mechanical properties reduction is mostly attributed to the stiffening of the matrix and the loss of adhesion with fibers, after the aging treatment. Similar results were obtained from other authors [11], registering a flexural strength decrease of about 10 % (Table 3.1) by exposing polyester profiles to a continuous condensation at 40 °C.

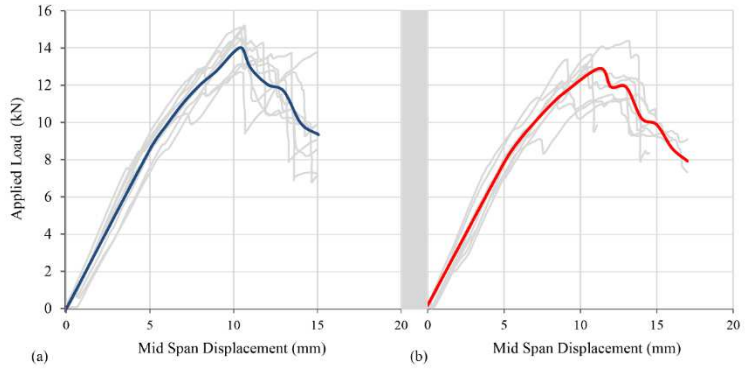

Figure 3.10. Results of flexural tests of un-aged (a) and aged (b) specimens. The curves in bolt format represent the medium values.

Specimens failure modes before and after the ageing treatment were very similar (Figure 3.11). In the compression zone, the loading member caused structural deformations with web-flange separation cracks due to shear stresses (Figure 3.11 a-b). Under the loading area, the cracking direction is more vertical (Figure 3.11 c-d) for the transverse bending acting in this zone [29]. However aged profiles showed several fractures also in the middle parts of both web and flanges for the increased stiffness of the matrix.

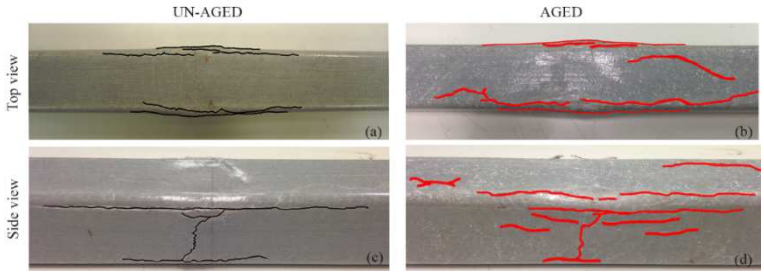

Figure 3.11. Specimens failure modes, before (a-c) and after (b-d) ageing.

3.4.5) Check of non-standard geometries

The geometries used in tensile tests (in particular the samples with reduced size) and torsional tests are not standard, as mentioned in the relative chapters. In order to check the results accuracy, experimental and numerical simulations were carried out.
Adjunctive tests on specimens with reduced geometries, with the same fiber orientation of the standard ones (0°), were done to verify the scale effect. The Young's modulus in the 0°

direction for the two specimen dimensions was compared. The results shown in Table 3.4 demonstrates that the reduced specimens provide an average value of the elastic modulus that is very similar to the one obtained with the standard ones, even with a larger scatter. In fact, the reduced dimension of the tested profiles may determine a higher dispersion of the results, as stressed in [30]. The same idea was also supported in [18], which highlighted that specimens with small dimensions could produce scattered results because of the probable different fiber content.

Table 3.4. Elastic modulus values (GPa) of dog-bones specimens (with 0° fiber direction) with standard and reduced dimensions.

un-aged standard dimensions	***aged standard dimensions***	***un-aged reduced dimensions***
33.87	33.02	23.16
36.15	31.44	17.99
35.76	31.45	52.61
29.78	31.37	33.32
27.71	26.75	32.61
32.66 ± 0.37	**30.81 ± 2.37**	**31.94 ± 13.23**

The values with bold format refer to the mean and standard deviations values.

Numerical simulations on both dog bones and squared profiles were carried out to demonstrate that the stress distribution is almost uniform in the gauge region and that the Saint Venant principle is still reasonably valid. Moreover, they were used to assess the error obtained with such geometries in the identification of the engineering material properties.
An FE model was built using ANSYS, adopting 15000 brick elements for the tensile specimen and 200000 brick elements for the torsional one, see Figure 3.12. The constitutive model used in the numerical simulations is a linear elastic orthotropic model, with constitutive parameters similar to those obtained from the experimental tests (E_1=32 GPa, E_2=3.8 GPa, G_{12}= 2.0 GPa, ν_{12}=0.2). Those parameters were used as reference to evaluate the identification error. According to the FE models:

- For tensile specimens with reduced size, Figure 3.12a shows an almost uniform stress distribution in the measurement and, if a gauge distance L_0 = 12 mm is used to compute the Young's modulus, the error is less than 1% respect to the reference parameters.

- For torsional specimens, Figure 3.12b shows the equivalent von Mises stress after a rotation of the end of 10 degrees and the stress distribution is almost uniform except for the clamping zone. If Eq. (2) is used to compute the shear modulus, using the rotation and the torque from the FE model, the error respect to the reference parameter G_{12} is less than 7%, which is still acceptable.

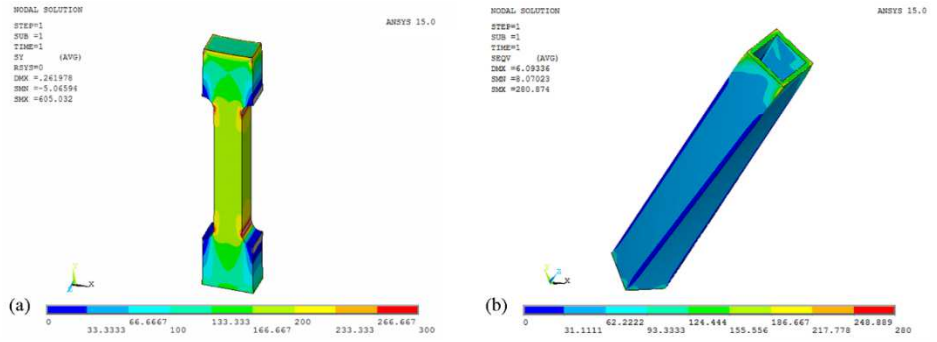

Figure 3.12. FE models of non-standard geometries. (a) Tensile specimen with reduced size: the stress distribution with an applied load of 5kN is almost uniform; (b) Torsional specimen: the stress distribution is uniform except for the two edges; the equivalent von Mises stress is plotted. The stress color scale is in MPa.

3.5 Conclusions

This experimental study investigates the effects of high temperatures and humidity on different geometries of polyester pultruded profiles (i.e. dog-bones and squared tubular specimens), involving absorption, tensional, torsional and flexural tests. The main outcomes are:

- The trend of absorption of the specimens through the ageing period deviated from the ideal Fickian behavior and it was characterized by an initial linear phase followed by a slightly fluctuating tendency, never reaching the equilibrium. This is a characteristic feature of a polymeric matrix as found in the literature. The percentage of mass gain registered by the different samples (all around 0.7 %) was almost similar regardless the different geometries and it was slightly lower than those obtained by other authors, thanks to the presence of a polyester veil on the surface of the profiles.

- Regarding the tensile test, the mechanical properties of specimens tested along the fiber direction (0°) were slightly affected by the ageing treatment: about 5 % and 4 % respectively for elastic modulus and tensile strength). A greater sensitivity to ageing was observed in the other fiber directions (45° and 90°): the average elastic modulus reduction was about 7 % and 16 %, respectively; instead, the average tensile strength reduction was about 15 % and 17 %, respectively. This is because the artificial ageing has a major impact in the degradation of the matrix, which in the latter configurations is more stressed than fibers. However, other research studies are needed on this topic as a large variance was observed because of the reduced specimen dimensions. All samples showed the same failure modes before and after the ageing treatment, occurring along the fiber direction.

- Regarding torsional and flexural tests, the reduction of the loading capabilities of about 8 %, for both types of stress, was showed. The matrix, in this loading condition, is more involved in the failure mechanism than in tensile stress. This aspect was also evident in the failure modes of the aged specimens, which are more damaged than the un-aged ones. The shear modulus of the tested profiles, calculated through a numerical model, was instead reduced to 3 % after ageing.

These results confirmed the applicability of GFRP pultruded profiles on windows and curtain walls, since they maintained adequate mechanical performance even after the ageing treatment.

3.6 References

[1] F. Stazi, M. Giampaoli, L. Nisi, M. Rossi, P. Munafò. Mechanical performance reduction of GFRP specimens with polyester matrix exposed to continuous condensation. *Composites Part B* 99 (2016) 330-339

[2] Chacòn Y. G, Paciornic S, d'Almeida J. R. M. Microstructural evaluation and flexural mechanical behavior of pultruded glass fiber composites. *Materials Science and Engineering* A 2010 (528) 172-179

[3] Sà M. F, Gomes A. M, Correia J. R, Silvestre N. Creep behavior of pultruded GFRP elements – Part 1: literature review and experimental study. *Composite Structures* 93 (2011) 2450-2459

[4] Turvey G. J. Torsion test on pultruded GRP sheet. *Composites Science and Technology* 58 (1988) 1343-1351

[5] Keller T, Tirelli T, Zhou A. Tensile fatigue performance of pultruded glass fiber reinforced polymer profiles. *Composite Structures* 68 (2005) 235-245

[6] Bai Y, Vallèe T, Keller T. Delamination of pultruded glass fiber-reinforced polymer composites subjected to axial compression. Composite Structures 91 (2009) 66-73

[7] Carrion J. E, LaFave J. M, Hjelmstad K. D. Experimental behavior of monolithic composite cuff connections for fiber reinforced plastic box sections. *Composite Structures* 67 (2005) 333-345

[8] Feo L, Mosallam A. S, Penna R. Mechanical behavior of web-flange junctions of thin-walled pultruded I-profiles: an experimental and numerical evaluation. *Composite: part B* 48 (2013) 18-39

[9] Bank L. C, Oliva M. G, Bae H-U, Bindrich B. V. Hybrid concrete and pultruded-plank slabs for highway and pedestrian bridges. *Construction and Building Materials* 24 (2010) 552-558

[10] Carra G, Carvèlli V. Ageing of pultruded glass fibre reinforced polymer composites exposed to combined environmental agents. *Composite Structures* 108 (2014) 1019-1026

[11] Cabral-Fonseca S, Correia J. R, Rodrigues M. P, Branco F. A. Artificial accelerated ageing of GFRP pultruded profiles made of polyester and vinyl ester resins: characterization of physical-chemical and mechanical damage. *Strain* 48 (2012) 162–173

[12] Correia J. R, Cabral-Fonseca S, Branco F. A, Ferreira J. G, Eusebio M. I, Rodrigues M. P. Durability of glass fibre reinforced polyester (GFRP) pultruded profiles used in civil engineering applications. *Mechanics of Composite Materials* 42 (2006) 325-338

[13] Sousa J. M, Correia J. R, Cabral-Fonseca S. Durability of glass fibre reinforced polymer pultruded profiles: comparison between QUV accelerated exposure and natural weathering in a mediterranean climate. *Experimental Techniques* 40 (2016) 207-219

[14] Aniskevich K, Aniskevich A, Arnautov A, Jansons J. Mechanical properties of pultruded glass fibre-reinforced plastic after moistening. *Composite Structures* 94 (2012) 2914-2919

[15] Weitsman Y. J, Effects of fluids on polymer composites. A review. *Contract technical report* (1995)

[16] Ben Daly H, Ben Brahim H, Hfaied N, Harchay M, Boukhili R. Investigation of Water Absorption in Pultruded Composites Containing Fillers and Low Profile Additives. *Polymer Composites* (2007) 355-364

[17] Girao J. P, M. de Sousa. Durability of GFRP Pultruded Profiles made of Vinylester Resin M.Sc. Dissertation Extended Abstract. October (2011)

[18] Liao K, Schultheisz C.R, Hunston D.L. Effects of environmental aging on the properties of pultruded GFRP. *Composites, Part B* 30 (1999) 485-493

[19] ISO 6270-2:2005. Paints and varnishes — Determination of resistance to humidity — Part 2: Procedure for exposing test specimens in condensation-water atmospheres

[20] ISO 527-4:2012. Plastics -Determination of tensile properties – Part 4: Test conditions for isotropic and orthotropic fibre-reinforced plastic composites

[21] Turvey G. J. Testing of pultruded glass fibre-reinforced polymer (GFRP) composite materials and structures. Woodhead Publishing Series in *Civil and Structural Engineering* (2013) 440–508

[22] Cortese L, Coppola T, Campanelli F, Broggiato G.B. (2015). A J2-J3 approach in plastic and damage description of ductile materials. *International Journal of Damage Mechanics* 25 (2016) 228-250

[23] EN 13706-2:2002. Reinforced plastics composites – Specifications for pultruded profiles – Part 2: Methods of test and general requirements

[24] Jiang X, Kolstein H, Bijlaard F.S.K. Moisture diffusion and hygrothermal aging in pultruded fibre reinforced polymer composites of bridge decks. *Materials and Design* 37 (2012) 304–312

[25] Talreja R, Veer Singh C. Damage and failure of composite materials. *Cambridge University Press*, London (2012)

[26] Barros A, La Rovere H. L. Flexural stiffness characterization of fiber reinforced plastic (FRP) pultruded Beam. *Composite Structures* 81 (2007) 274-282

[27] Correia J. R, Branco F. A, Camotim S. D, Silvestre N. First-order, buckling and post-buckling behaviour of GFRP pultruded beams. Part 1: Experimental study. *Computers and Structures* 89 (2011) 2052-2064

[28] Zhang Y, Vassilopoulos A. P, Keller T. Mixed-mode fracture of adhesively-bonded pultruded composite lap joints. *Engineering Fracture Mechanics* 77 (2010) 2712-2726

[29] Chotard T.J, Pasquiet J, Benzeggagh M.L. Impact response and residual performance of GRP pultruded shapes under static and fatigue loading. *Composites Science and Technology* 60 (2000) 895-912

[30] Sutherland L.S, Shenoi R. A, Lewis S.M. Size and scale effects in composites: II. Unidirectional laminates. *Composite Science and Technology* 59 (1999) 221-233

3.7 List of tables and figures

Chapter 4

On GFRP single-lap and butt joints bonded with different adhesives: mechanical performances before and after the ageing treatments

In the Full Glass window, the mobile frame inserted in the double glass cavity is composed of four GFRP profiles connected through the bonding technique. The aim of the present study is to compare the mechanical behavior of pultruded GFRP joints, bonded with different types of adhesives, under both un-aged and aged conditions. The contents of this chapter were published in a previous work: *"Environmental ageing on GFRP pultruded joints: Comparison between different adhesives"* [1].

4.1 Abstract

In this paper, a series of mechanical tests were performed on GFRP (glass fibre reinforced polymers) specimens, adhesively bonded in single-lap and butt joints, in both un-aged and aged conditions. Six different types of adhesives were compared: two epoxies, one acrylic, one methacrylate and two polyurethane adhesives. Two ageing conditions were investigated, i.e. temperature/moisture changes and UV exposure.

Both environmental exposures had a slight effect on the load carrying capacity of the joints, while they remarkably increased their elongation, with a stiffness decrease of about 70÷90 %. For some adhesives, the load carrying capacity was improved because of the completion of the polymerization process caused by the high or slightly high temperatures. For all joints, in both exposures a great stiffness decrease occurred: it was ascribed to the reaching of adhesives T_g during cycles of combined high and low temperatures and to the polymer bond dissociations during UV radiation.

Both before and after the two ageing treatments, the highest load carrying capacity was recorded by the epoxy adhesives that, on the contrary, showed the highest joint elongations. The two polyurethane adhesives always recorded similar ultimate loads, but one of them presented lower deformations, also showing the best compatibility with pultruded laminates.

Nomenclature

ACR	Acrylic adhesive	***MS***	Second polyurethane adhesive
AF	Adhesive failure	***PU***	First polyurethane adhesive
A_t	Application temperature	s_{lj}	Single-lap joint
b_j	Butt joint	S_t	Service temperature
CF	Cohesive failure	T_0	Un-aged conditions
DSC	Differential scanning calorimeter	T_c	Artificial ageing in climatic chamber
EPX1	First epoxy adhesive	T_{eig}	Extrapolated onset temperature
EPX2	Second epoxy adhesive	T_{eig}	Extrapolated end temperature
E_Y	Young modulus	T_g	Glass transition temperature
F	Ultimate failure load	T_{uv}	Artificial ageing under UV rays
GFRP	Glass fiber-reinforced polymer	***UV***	Ultraviolet radiations
k	Joint stiffness	W_t	Working time at 22 °C
L	Elongation	ε	Tensile strain
LFTF	Light-Fiber-Tear Failure	σ	Tensile strength
MET	Methacrylate adhesive	τ	Average shear strength
MF	Mixed failure		

4.2 Introduction

GFRP profiles are materials with a high fiber content and, despite the several beneficial characteristics [2], this feature led to some disadvantages: their mechanical properties, in fact, are different depending on the orientation of the fibers and the design data are still scarce in the literature [3]. Moreover, they present the difficulty of realizing bolted joints [4], because adherents are subjected to drilling operations that cut the fibers. In this case, adhesive connection represents the most efficient joining method, leading to a uniform load transfer [5-7]. However, this kind of connection is strongly influenced by high temperatures and humidity levels, which can reduce mechanical properties of the adhesives [6,8].
To the author's knowledge, validated data about different types of adhesives used in GFRP joints, focused in the civil engineering field, are still scarce and very few studies were conducted on the ageing degradation mechanisms.

The aim of the present study is to compare the mechanical behavior of pultruded GFRP joints, bonded with different types of adhesives, under both un-aged and aged conditions. Six different types of adhesives were investigated: two epoxies, one acrylic, one methacrylate and two polyurethane adhesives. Single lap and butt joints were loaded up to failure, and the results obtained from un-aged specimens were compared with those subjected to cyclic accelerated exposure to moisture, low and high temperatures, and ultraviolet (UV) radiation.

4.3 Experimental methods

4.3.1) Specimen dimensions

Single lap-joints and butt-joints with all tested adhesives were fabricated using pultruded GFRP laminates (Fig. 4.1). The *Single-lap joints* were manufactured from laminates according to [9]. The width of laminates was 25 mm, the thickness 5 mm and the length 100 mm; the overlap length was 12.5 mm. The laminates were cut from squared tubular profiles with cutting section of 50x50x5 mm. Two pieces of laminates (width 25 mm, length 30 mm) were bonded at the ends of the adherents to facilitate gripping of the jaws and avoid misalignment.

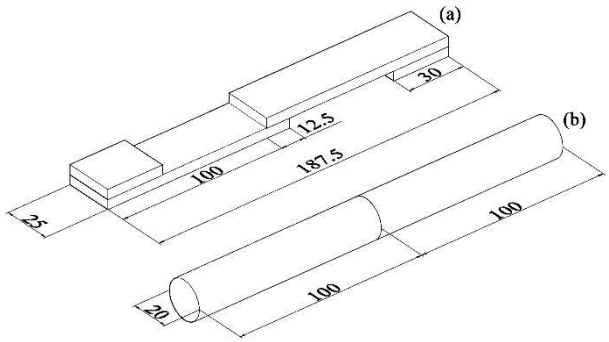

Figure 4.1. Geometry of the specimens used in single-lap (a) and butt (b) joints (dimensions in [mm]).

Single-lap joints are the most widely used method for producing shear strength data of adhesively bonded joints. However the shear tension is associated with peel stress, with variable entity depending on different joints features: adhesives thickness and stiffness [10], overlap length and adherents thickness [11,12]. In relation to the geometries and materials adopted in the present study, the peel effects could be considered negligible, as highlighted in the literature [11].
The *Butt-joints* were manufactured from round rods according to [13]. The length of rods was 100 mm and the diameter 20 mm.
Before applying the adhesives, the surface of the bonding region was mechanically abraded with a sandblasting paper and, for some specimens, a degrease was also used (see Table 4.1).

Table 4.1. Technical and mechanical characteristics of tested adhesives reported by manufacturers.

Adhesive	***EPX1***	***EPX2***	***ACR***	***MET***	***PU***	***MS***
$\boldsymbol{Chemical\ base}$	two-part epoxy adhesive	two-part epoxy adhesive	two-part acrylic adhesive	one-part methacrylate adhesive	one-part polyurethane adhesive/sealant	one-part polyurethane adhesive/sealant
$\boldsymbol{Consistency}$	controlled flow	pasty	viscous	viscous	medium paste	pasty
$\boldsymbol{W_t}$ *(min)*	>300	120	8-12	15	300	20±10
$\boldsymbol{A_t}$ *(°C)*	15 to 25	15 to 25	4 to 22	15 to 35	16 to 27	15 to 35
$\boldsymbol{S_t}$ *(°C)*	-40+120	-40+80	-40+100	-54+100	-40+120	-40+100
$\boldsymbol{T_g}$ *(°C)*	/	71	/	/	-35	-40
$\boldsymbol{Surface\ treatment}$	sand	sand and degrease	sand and degrease	sand and degrease with activator	sand and degrease	sand and degrease
$\boldsymbol{\tau^*}$ *(MPa)*	33.5	15	25	15-30	2.6	1.8
$\boldsymbol{\sigma}$ *(Mpa)*	/	17	/	12-22	6	/
$\boldsymbol{E_Y}$ *(MPa)*	/	1700	/	/	/	1.8
$\boldsymbol{\varepsilon}$ *(%)*	3	5	5	<10	>100	>100
Use	structural	semi-structural	structural	structural	non-structural	non-structural

* On aluminum/steel adherents

To ensure the correct manufacturing and alignment of the specimens, a special wood frame was designed and employed for the production of the joints (Fig. 4.2a). All specimens were cured under ambient laboratory conditions (temperature of 21 °C, relative humidity of 33 %) for 23 days, as recommended by manufacturers.

Figure 4.2. Instruments used for samples preparation (a) and for UV ageing exposures (b).

4.3.2) Material properties

4.3.2.1) GFRP laminates

The studied material is a pultruded E-glass fiber reinforced vinyl ester composite, supplied by Fibrolux, Germany. This material consists of alternating layers of unidirectional fiber roving and chopped strand mat embedded in vinyl ester matrix. A polyester surface veil is used to protect the matrix against environmental actions. As a result of the pultrusion process, the fiber rovings are not uniformly distributed.
In order to determine the mechanical properties, GFRP laminates were tested in tension, according to [14,15]. The width of laminates was 25 mm, the thickness 5 mm and the length 100 mm. The free length was 70 mm and the gauge length of the extensometer was set to 50 mm. The tests were performed with a Zwick/Roell Z050 testing machine, using an extensometer to measure the strain and applying a displacement rate of 5 mm/min. Because of the small size of the used specimens, some of them may contain more fiber roving than others, and this produces a scatter in the mechanical properties. For this reason, three specimens were used for each considered ageing conditions, that are: no ageing (T_0), exposure to severe humidity and high and low temperatures (T_c), and exposure to UV radiation (T_{uv}). The results, summarized in Table 4.2, were used to assess the contribution of the adherents to the total elongation of the joints (Section 4.4.2).

Table 4.2. Mechanical properties in the tension of GFRP materials.

Artificial exposure	E_Y *(GPa)*	σ *(Mpa)*	ε *(%)*
T_0	29.8 ±2.6	168.8 ±31.1	0.7 ±0.2
T_c	27.1 ±2.6	251.8 ±61.9	0.9 ±0.2
T_{uv}	27.8 ±6.5	199.4 ±91.6	0.8 ±0.3

4.3.2.2) Adhesives

Six adhesives of several families were considered in the experimental program: two epoxy adhesives (designated *EPX1* and *EPX2*), one acrylic adhesives (designated *ACR*), one methacrylate adhesive (designated *MET*) and two polyurethane adhesives (designated *PU* and *MS*). Table 4.1 presents the relative technical and mechanical characteristics, reported from manufacturers. Some technical data were not available.
In order to determine adhesives mechanical properties, five specimens of each type of adhesive were tested in tension, according to [14,16]. The dimensions of the dumbbell specimens are shown in Fig. 4.3.

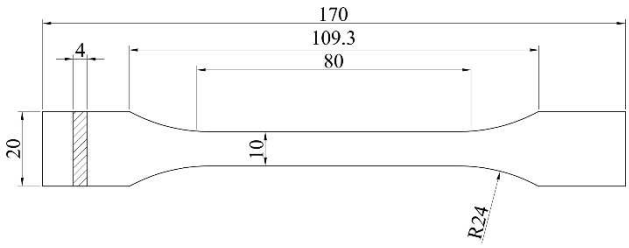

Figure 4.3. Dumbbell specimens dimensions.

All specimens were cured at room temperature for about one month. The results (Table 4.3) were consistent with the data reported by manufacturers, confirming the highest performance of the first epoxy adhesive and the worst load bearing capacity of MS composition.

Table 4.3. Mechanical properties in tension and glass transition temperatures of the adhesives.

Series	E_Y *(MPa)*	σ *(Mpa)*	ε *(%)*	T_g *(°C)*
EPX1	2966.39 ± 44.12	27.34 ± 0.77	2.39 ± 0.65	61.07 ± 3.34
EPX2	1774.03 ± 30.28	17.11 ± 0.70	3.81 ± 0.23	66.87 ± 0.45
ACR	648.60 ± 22.00	11.13 ± 0.50	7.26 ± 0.70	69.37 ± 1.96
MET	428.66 ± 62.00	7.31 ± 0.42	2.96 ± 0.05	70.70 ± 1.41
PU	2.43 ± 0.14	3.41 ± 0.27	150.79 ± 15.93	-35*
MS	2.05 ± 0.18	2.03 ± 0.10	151.10 ± 7.24	-40*

* Reported by manufacturers

In order to determine adhesives glass transition temperature (T_g), three samples of each type of adhesive were tested with a differential scanning calorimeter (*DSC*), according to the standard [17]. DSC plots were obtained by heating samples from 25 °C to 120 °C at a rate of 20 °C/min under an inert gas flow of 100 ml/min. The samples weights were in the range of 10 to 15 mg with a precision of 0.01 mg. The T_g was determined (according to procedure 10.2.9 of [17]) as the midpoint temperature between the extrapolated onset temperature (T_{eig}) and the extrapolated end temperature (T_{efg}). In Fig. 4.4 is reported, as an example, the T_g assignment of one ACR sample. The results (Table 4.3) showed that among structural adhesives, MET had the highest T_g (on average 70.7 °C) and very similar temperatures were obtained for the other adhesives. For non-structural adhesives, it was not possible to identify the T_g values since, as stated by various authors [18], the study of the decomposition of polyurethanes is particularly difficult, complex and heterogeneous, involving a multitude of physical and chemical phenomena. Nevertheless, some authors [19] founded a T_g value for thermoplastic polyurethane adhesives of –49 °C. This value is consistent with those declared by manufacturers for PU and MS adhesives, respectively -40 °C and -35 °C.

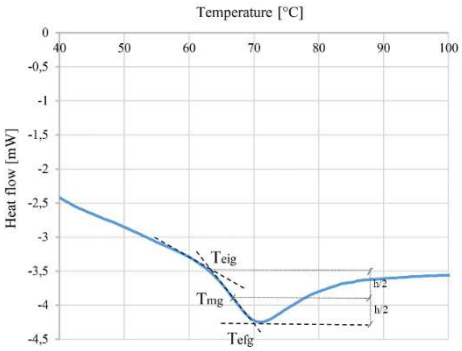

Figure 4.4. Glass transition temperature assignment of one ACR sample.

4.3.3) Mechanical tests

The test program consisted of a series of 18 specimens per adhesive type, as illustrated in Table 4.4. Each series had 9 specimens per support type, i.e. single lap joint and butt joint, subdivided according to the ageing condition: 3 without ageing (T_0), 3 after exposure to humidity and high and low temperatures (T_c), and 3 after exposure to UV radiations (T_{uv}). A different bonding thickness among structural and non-structural adhesives was employed (Table 4.4), respectively 0.3 mm and 2 mm, as recommended by manufacturers. All specimens were loaded up to the joint failure, using a displacement rate of 2.5 mm/min.

Table 4.4. Experimental setup

Series	***Type of joint***	***Adhesives thickness*** *(mm)*	***Geometry of supports***	T_0	T_c	T_{uv}
EPX1	s_{lj}	0.3	laminates	3	3	3
	b_j		rods	3	3	3
EPX2	s_{lj}	0.3	laminates	3	3	3
	b_j		rods	3	3	3
ACR	s_{lj}	0.3	laminates	3	3	3
	b_j		rods	3	3	3
MET	s_{lj}	0.3	laminates	3	3	3
	b_j		rods	3	3	3
PU	s_{lj}	2	laminates	3	3	3
	b_j		rods	3	3	3
MS	s_{lj}	2	laminates	3	3	3
	b_j		rods	3	3	3

The shear strength tests were carried out according to [9] using the single lap joints, while tensile strength tests were carried out according to [13], using butt-joints. All tests were implemented on a Zwick/Roell Z050 testing machine of 50 kN capacity under displacements control (Fig. 4.5a-b).The load and total specimens elongation were measured by transducers within the testing machine.

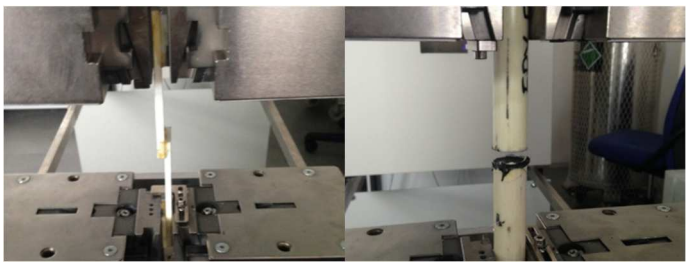

Figure 4.5. Z050 testing machine with clamped single-lap (a) and butt (b) specimens.

4.3.4) Artificial ageing

Two types of ageing were taken into account, one to reproduce the external environment exposure (T_c) and another to reproduce the UV irradiation effect (T_{uv}).
The external environment exposure was simulated using a climatic chamber "Angelantoni" CST-130 S model. A total number of 36 joints was aged according to Cycle D2 of [20]. Each cycle consisted of three exposure periods: first 16 hours at the constant temperature of 40 °C and relative humidity of 100 %, then 4 hours at the constant temperature of -40 °C and finally 4 hours at the constant temperature of 70 °C and relative humidity of 50 %. This ageing cycle was repeated for 2 weeks, according to the standard [20].
The UV ageing was simulated using eight fluorescent UV lamps (Philips Actinic BL TL-D). A total of 36 joints were aged according to [21] with some adaptations. In fact, as highlighted in a previous work [22], the effects of high temperatures (40 °C) are much more relevant than those of UV rays. So these two extreme environmental conditions should be separately analyzed to deepen the UV influence alone. The specimens were subjected to high UV radiations but under laboratory conditions (temperature of 21 °C, relative humidity of 33 %). The recorded temperature on specimens surface was about 26 °C. The samples were placed in horizontal position inside a metallic structure equipped with 4 lamps, 2 at the top and 2 at the bottom (Fig. 4.2b), in order to guarantee a uniform distribution of irradiation. The lamps emitted on a wavelength in the range of 340-400 nm [23], with a peak at 370 nm, producing a UV irradiance between 41 and 45 W/m² on the specimens surfaces. Cycle II of 24 hours [21] was repeated 42 times (overall 1000 hours) without interruption.

4.4 Results

In this section, the load-elongation response and the failure modes of single-lap and butt joints are presented and analyzed. The results are subdivided according to the used environmental conditions (T_0, T_c, and T_{uv}). An in-depth analysis on the contribute of GFRP adherents to the whole joint elongation is reported.

4.4.1) Joints load-elongation response

4.4.1.1) Without ageing (T0)

The load-elongation responses of representative un-aged (as produced) specimens, subjected to shear and tensile tests are shown, respectively, in Fig. 4.6a-b. All tested adhesives had almost a similar behavior for single-lap joint and butt joint. Epoxy (EPX1 and EPX2), acrylic (ACR) and methacrylate (MET) adhesives presented an elastic non-linear behavior, until a brittle rupture. The two polyurethane adhesives (PU and MS) exhibited a much lower load carrying capacity, with low curve slopes and softening phenomena after the ultimate load.

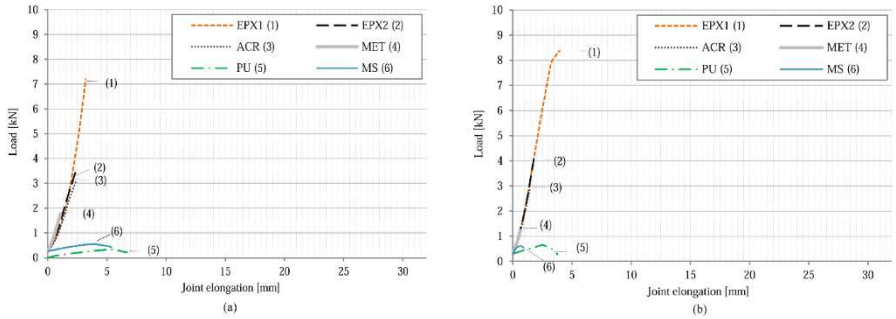

Figure 4.6. Load-joint elongation response of un-aged single-lap (a) and butt (b) specimens.

The ultimate loads (kN) and joint elongations (mm) at failure are given in Table 4.5 in terms of average and standard deviations. The ultimate average shear and normal stress (MPa) were obtained dividing the ultimate loads by the area of the bonded surfaces, for the single-lap and butt configurations, respectively. Table 4.5 shows also the average joint stiffness (kN/mm) computed as the ratio of load to elongation, in the elastic range. For the same adhesive, single-lap joints and butt joints exhibited different ultimate loads. This is because, in the two test configurations, adhesives were subjected to different stress conditions, namely shear and tension.

Table 4.5. Summary of results of shear (slj) and tensile (bj) test on un-aged specimens.

Series	***Type of joint***	***F*** *(kN)*	***L**** *(mm)*	***Ultimate stress*** *(MPa)*	***k*** *(kN/mm)*
EPX1	s_{lj}	7.2 ± 0.5	3.2 ± 0.4	24.6 (τ)	1.15
	b_j	8.4 ± 0.5	3.9 ± 1.1	26.7 (σ)	2.05
EPX2	s_{lj}	3.5 ± 0.8	2.3 ± 0.7	11.1	1.32
	b_j	4.1 ± 1.3	1.8 ± 0.4	13.2	2.00
ACR	s_{lj}	3.1 ± 0.7	2.4 ± 0.6	10.0	1.11
	b_j	2.9 ± 1.0	1.5 ± 0.4	9.4	1.87
MET	s_{lj}	1.8 ± 0.1	1.1 ± 0.04	5.7	1.64
	b_j	1.2 ± 0.4	0.6 ± 0.2	3.9	1.98
PU	s_{lj}	0.3 ± 0.04	5.3 ± 0.6	1.1	0.18
	b_j	0.6 ± 0.1	2.5 ± 0.7	2.1	0.40
MS	s_{lj}	0.5 ± 0.1	4.0 ± 0.5	1.8	0.26
	b_j	0.6 ± 0.05	0.6 ± 0.08	2.0	1.77

* corresponding to the maximum carried value

The ultimate load of EPX1, in single-lap joint configuration, was 7.2 kN, twice than specimens EPX2 (3.5 kN). This trend was confirmed by butt-joints results. The joint elongation of EPX1 was greater than EPX2. For both adhesives, different stiffness among single-lap and butt joint was observed: around 1 kN/mm for the former, and 2 kN/mm for the latter configuration. ACR samples reached ultimate loads slightly lower than EPX2, and the average ultimate stress was around 10 MPa for both single-lap and butt joints. MET samples had ultimate loads and joint elongations lower than previous adhesives. However, in single-lap configuration, MET showed the highest stiffness of all samples (on average 1.64 kN/mm). The non-structural adhesives exhibited ultimate loads 90 % lower than EPX1. In single-lap configuration (shear test), joint elongations were higher than the epoxy adhesive: 5.3 mm and 4.0 mm for respectively PU and MS series. Tensile test with PU and MS butt series revealed instead lower values of elongation. This results variability in the two loading conditions could be ascribed to the relevance of the joint geometry, especially for non-structural adhesives [24]. Joint stiffness values were much lower than the epoxy adhesive, except for the MS adhesive in butt configuration (1.77 kN/mm).
In summary epoxy specimens, and in particular EPX1, had the highest load carrying capacity, for both types of joint. MET did not seem the most appropriate adhesive for GFRP adherents, with low carrying capacity and brittle behavior. In specimens bonded with the two non-structural adhesives, high joint elongations were observed.

4.4.1.2) Exposure to moisture and temperatures (T_c)

Fig. 4.7 shows the representative load-elongation responses of specimens subjected to different temperature and moisture cycles. Single-lap (a) and butt (b) joints of the two epoxy, acrylic, and methacrylate adhesives maintained an elastic non-linear trend, with higher joint elongations and lower curves slope than un-aged specimens. Both non-structural adhesives showed an increase of ductility.

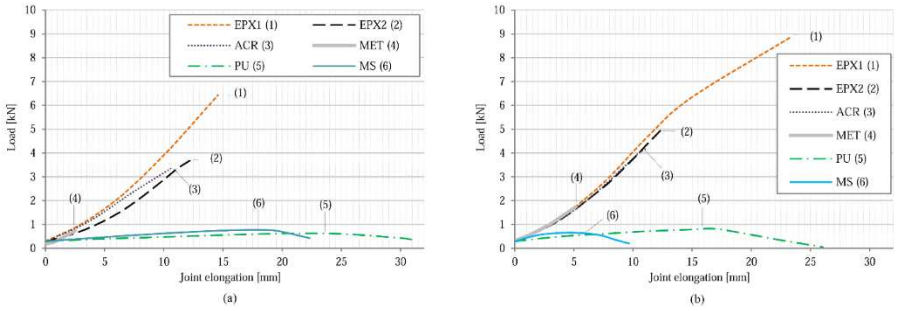

Figure 4.7. Load-joint elongation response of single-lap (a) and butt (b) specimens aged in a climatic chamber.

Table 4.6 presents the results obtained for the different series, concerning ultimate loads (kN) and joint elongations (mm) at failure (in terms of average and standard deviations), ultimate average shear, normal stress (MPa) and joint stiffness (kN/mm).
EPX1 specimens reached the highest ultimate load (as in un-aged configuration), with values up to 6.3 kN and 8.6 kN, in single-lap and butt configurations, respectively. Both joints showed high elongations and a reduced stiffness of 0.34 kN/mm. Similar joint stiffness was achieved by the second epoxy and the acrylic adhesives, with ultimate load and joint elongations lower than EPX1 samples. MET adhesive showed premature brittle failures, with ultimate average shear and normal stress of 2.3 MPa and 5.6 MPa. With respect to the other adhesives, they had the highest joint stiffness, 0.39 kN/mm (shear) and 0.33 kN/mm (tension).With both polyurethane adhesives, very high joint elongations were measured, except for MS in butt configuration. The lowest ultimate loads were registered, and very low joint stiffness was calculated (0.04÷0.06 kN/mm).
A comparison with Table 4.5 shows that ultimate loads were slightly higher than those of un-aged specimens, for all the adhesives except for EPX1 and MET adhesives in single-lap configuration. Even PU-s_{lj} specimens showed a load carrying capacity of 0.6 kN, twice than un-aged specimens. Moreover, joint elongations were higher than those in the un-aged conditions, up to 23.3 mm for the first epoxy adhesive in butt joints, compared to 3.9 mm for the un-aged condition. In general, a decrease of about 70÷90 % was observed in the joint stiffness after the temperatures ageing.

Table 4.6. Summary of results of shear (slj) and tensile (bj) test on specimens aged in a climatic chamber.

Series	***Type of joint***	***F*** *(kN)*	***L**** *(mm)*	***Ultimate stress*** *(MPa)*	***k*** *(kN/mm)*
EPX1	s_{lj}	6.3 ± 1.2	14.6 ± 3.0	20.6 (τ)	0.34
	b_j	8.6 ± 2.1	23.3 ± 6.6	28.2 (σ)	0.34
EPX2	s_{lj}	3.8 ± 0.2	12.5 ± 0.5	12.0	0.23
	b_j	5.1 ± 0.2	12.6 ± 0.5	16.1	0.31
ACR	s_{lj}	3.4 ± 1.0	10.8 ± 3.4	10.9	0.31
	b_j	4.1 ± 0.1	11.1 ± 0.8	13.3	0.32
MET	s_{lj}	0.7 ± 0.2	2.5 ± 0.7	2.3	0.39
	b_j	1.7 ± 0.7	5.2 ± 1.8	5.6	0.33
PU	s_{lj}	0.6 ± 0.02	22.4 ± 9.8	2.0	0.04
	b_j	0.8 ± 0.02	16.8 ± 2.5	2.6	0.05
MS	s_{lj}	0.8 ± 0.04	17.6 ± 1.3	2.5	0.06
	b_j	0.7 ± 0.01	4.7 ± 1.1	2.1	0.19

* corresponding to the maximum carried value

4.4.1.3) Exposure to UV radiation (Tuv)

In the other investigated environmental exposure, all tested adhesives had similar load-elongation behavior for both types of specimens (Fig 4.8a-b): the curves show an elastic non-linear behavior, with higher joint elongations and lower curve slopes than un-aged specimens for structural adhesives. A ductile behavior with low ultimate loads for both polyurethanes is shown.

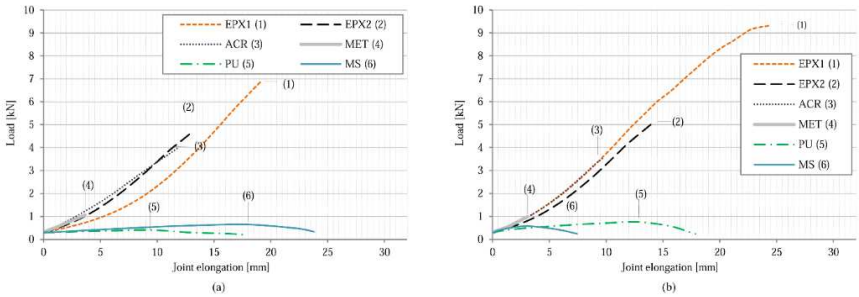

Figure 4.8. Load-joint elongation response of single-lap (a) and butt (b) specimens exposed to UV radiations.

Ultimate loads (kN), joint elongations (mm) at failure (in terms of average and standard deviations), ultimate average shear, normal stress (MPa) and joint stiffness (kN/mm) are summarized in Table 4.7. Among all the specimens subjected to UV radiations, single-lap and butt joints bonded with EPX1 reached the highest ultimate load (respectively 6.9 kN and 9.3 kN) and the highest global elongations. As in the previous case, the ultimate stress and joint elongation of EPX2 were lower than EPX1. Acrylic adhesive demonstrated a lower ultimate load and joint elongation than the previous adhesives but reached a higher joint stiffness: 0.35 kN/mm and 0.31 kN/mm in single-lap and butt configurations, respectively. This behavior differed from that obtained in the previous environmental exposure, where ACR demonstrated lower stiffness values than both epoxy adhesives. The methacrylate adhesive demonstrated again lower load carrying capacity than the others and also slightly lower ultimate loads than un-aged specimens; an incompatibility with pultruded laminates was confirmed. Both polyurethane adhesives presented a ductile behavior, with low load carrying capacity and very high joint elongations. The joint stiffness was lower than that of the other adhesives, except for MS in butt joint configuration (0.3 kN/mm).

Table 4.7. Summary of results of shear (slj) and tensile (bj) test on specimens exposed to UVA radiations.

Series	***Type of joint***	***F*** *(kN)*	***L**** *(mm)*	***Ultimate stress*** *(MPa)*	***k*** *(kN/mm)*
EPX1	s_{lj}	6.9 ± 0.4	19.2 ± 2.1	22.1 (τ)	0.18
	b_j	9.3 ± 0.2	24.5 ± 1.8	29.7 (σ)	0.31
EPX2	s_{lj}	4.7 ± 0.1	13.2 ± 1.4	15.1	0.28
	b_j	5.1 ± 0.2	14.1 ± 1.8	16.1	0.26
ACR	s_{lj}	4.0 ± 0.4	11.9 ± 3.8	12.9	0.35
	b_j	3.6 ± 0.4	9.8 ± 0.6	11.4	0.31
MET	s_{lj}	1.1 ± 0.2	3.7 ± 1.3	3.4	0.30
	b_j	1.0 ± 0.5	3.1 ± 1.7	3.2	0.32
PU	s_{lj}	0.4 ± 0.04	9.4 ± 3.0	1.3	0.11
	b_j	0.8 ± 0.1	12.8 ± 1.8	2.4	0.05
MS	s_{lj}	0.6 ± 0.1	17.9 ± 2.9	2.1	0.07
	b_j	0.6 ± 0.1	3.1 ± 0.9	1.8	0.30

* corresponding to the maximum carried value

From a visual analysis, MET was the sole that showed a substantial variation of color (Fig. 4.9a-b). In summary, the effect of the UV radiations on the specimens was similar to that of combined moisture and temperatures, i.e. a slight increase of the ultimate load (except for EPX1 in single-lap configuration and MET) and a remarkable increase of the total specimen elongation. A decrease of joint stiffness (about 70÷90 %) with respect to un-aged specimens was again observed.

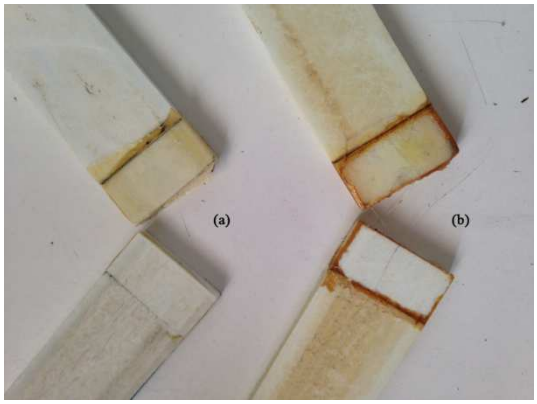

Figure 4.9. Methacrylate joints pre (a) and post (b) accelerated UV ageing.

4.4.2) Contribution of GFRP adherents to joint elongation

The displacement measured by the tensile machine included both the joint deformation and the individual contribution to the elastic deformation given by GFRP adherents and each adhesive. Since the objective was to characterize the joint behavior, it was important to evaluate what was the contribution of the single component to the total measured elongation. The aim of this section is to demonstrate that the GFRP supports can be approximated to a rigid body so that the displacement measured by the tensile machine can be all ascribed to the adhesive connection. To this purpose, the elastic elongation of the GFRP's support alone, at the maximum force recorded in all specimens, was compared to the total displacement measured by the tensile machine for jointed profiles. The elastic elongation was computed using the Hooke's law:

$$\Delta L_{elastic} = \frac{F_{max}}{A \cdot E_Y} L_{tot}$$

where:
F_{max} = ultimate failure load (N) of the joint
A = cross sectional area (mm²) of the GFRP adherent
E_Y = modulus of elasticity (MPa) of the GFRP adherent (see Table 4.2)
L_{tot} = initial total length (mm) of the joint

The ratio of the elastic elongation to the total joint elongation was found to be maximum for EPX1 in single-lap configuration: 7.7 % (with a $\Delta L_{elastic}$ equal to 0.24 mm and a total joint elongation of 3.2 mm). This very low value demonstrated the scarce incidence of GFRPs elongation on the total joint elongation.
The same observation could be drawn for the two ageing conditions, with even lower percentage values (1.6 % for T_c and 1.3 % for T_{uv}).

4.4.3) Failure modes

Fig. 4.10 shows four types of failure modes occurred during specimens mechanical tests and classified according to [25]. The first is an "Adhesive Failure" (*AF* - Fig. 4.10a), and occurred at the interface between the adherend and the adhesive, this is usually not accepted in adhesive technology [7]. The second is a "Cohesive Failure" (*CF* - Fig. 4.10b), occurring within the adhesive layer: this reveals a good compatibility between adhesive and adherents. In Fig. 4.10c there is an example of "Mixed Failure" (*MF*), combining adhesive and cohesive failure. The percentage of failure mode was evaluated by a graphical estimation. In the last figure (Fig. 4.10d) a "Light-Fiber-Tear Failure" (*LFTF*) is presented and occurred within the GFRP adherent, with few glass fibers transferred from the adherent to the adhesive. This last type of failure occurred only for one specimen exposed to UV radiation, thanks to material properties: in fact, E-glass fibers are embedded in vinyl ester resin, more resistant and stiffer than polyester, thus allowing to focus the study on adhesives behaviors (the weaker material),

rather than on the adherents. The quality and content of the pultruded material, in fact, is an important factor in joint efficiency [26].

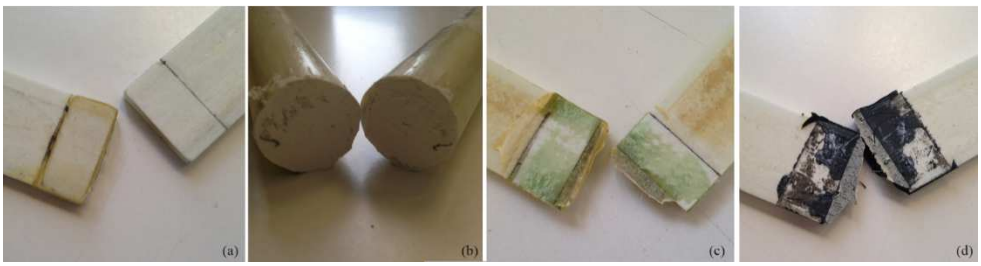

Figure 4.10. Different types of specimens failure modes: adhesive (a), cohesive (b), mixed (c), light fiber tear (d) failures.

Table 4.8 shows the failure modes of un-aged and aged specimens, subjected both to shear and tensile tests. Mostly, single-lap joints and butt joints, bonded with the same adhesive, presented different modes of fracture, due to different stress types: shear for the former and tensile for the latter.

Table 4.8. Summary of failure modes observed in un-aged (T0) and aged (Tc and Tuv) conditions: adhesive (AF), cohesive (CF), mixed (MF), light-fiber-tear (LFTF) failures.

Series	*Joint*	T_0	T_c	T_{uv}
EPX1	s_{1j}	1 *AF*, 1 *MF*(80% *CF*), 1 *MF*(70% *CF*)	1 *CF*, 1 *MF*(90% *AF*), 1 *MF*(70% *AF*)	2 *AF*, 1 *LFTF*
	b_j	1 *CF*, 1 *MF*(70% *AF*), 1 *MF*(60% *AF*)	3 *AF*	3 *AF*
EPX2	s_{1j}	1 *AF*, 2 *MF*(80% *AF*)	2 *AF*. 1 *MF*(95% *AF*)	3 *AF*
	b_j	2 *CF*, 1 *MF*(80% *AF*)	3 *AF*	2 *AF*. 1 *MF*(50% *AF*)
ACR	s_{1j}	2 *MF*(70% *AF*), 1 *MF*(90% *AF*)	1 *AF*, 2 *MF*(60% *CF*)	3 *MF*(60% *AF*)
	b_j	3 *CF*	2 *AF*, 1 *CF*	1 *AF*, 2 *MF*(90% *CF*)
MET	s_{1j}	3 *AF*	3 *AF*	3 *AF*
	b_j	3 *AF*	3 *AF*	3 *AF*
PU	s_{1j}	3 *AF*	2 *AF*, 1 *MF*(90% *AF*)	3 *AF*
	b_j	1 *MF*(70% *CF*), 1 *MF*(80% *AF*), 1 *MF*(90% *CF*)	3 *AF*	3 *AF*
MS	s_{1j}	3 *CF*	3 *CF*	3 *CF*
	b_j	3 *CF*	3 *CF*	1 *MF*(50% AF), 1 *MF*(80% *CF*), 1 *MF*(90% *CF*)

4.4.3.1) Without ageing (T0)

One EPX1-s_{lj} showed an adhesive fracture, while the other two failed for a combination of adhesive and cohesive failure (mainly cohesive). One EPX1-b_j showed instead, a cohesive failure, while the other two exhibited mixed (60÷70 %) fractures. In most single-lap joints, EPX2 failed in the interface between the adherend and the adhesive (80÷100 %); two EPX2-bj specimens presented cohesive failures, while one of them exhibited a mixed one (80% adhesive).
Mostly mixed adhesive failures for ACR-s_{lj} were observed (70% and 90% adhesive), while all tensile tests on ACR-b_j led to cohesive fractures. Joints bonded with methacrylate adhesive showed premature adhesive failures, in both MET-s_{lj} and MET-b_j configurations, therefore that type of adhesive seemed not to be the most appropriate for GFRP materials, otherwise, an inappropriate surface treatment occurred.
In all PU-s_{lj} adhesive failures were observed, while all PU-b_j specimens showed mixed fractures (both adhesive and cohesive). MS specimens showed the same cohesive fracture both in single-lap and butt joints, revealing the best physical/chemical compatibility between adhesive and adherents and, at the same time, a weaker strength than pultruded laminates.

4.4.3.2) Exposure to moisture and temperatures (Tc)

For both epoxy adhesives, the adherence with pultruded laminates got worse during the ageing process, and joints failure became mostly adhesive, except for one EPX1-s_{lj} (cohesive). During ACR tests, a slightly worse behavior, especially for butt joints, was observed (from cohesive to adhesive). MET adhesive showed the same failure mode in both joint configurations, it always occurred in the interface between the adhesive and the pultruded laminates (adhesive failure). A worse connection between adhesive and adherents was observed in aged PU adhesive than un-aged ones. Both the non-structural character and the good compatibility with the laminated support were still confirmed for MS adhesive: after mechanical tests, all cohesive failures were observed.
In summary, cycles in the climatic chamber had a noticeable influence on the failure process of the joint: except for MS specimens, the failure mechanism occurred mainly in adhesive-adherent interfaces.

4.4.3.3) Exposure to UV radiation (Tuv)

For the two epoxy adhesives, both joint configurations showed almost adhesive fractures, except for one light-fiber-tear failure occurred in an EPX1 single-lap specimen: it was a failure occurred within the FRP adherent, near the surface, characterized by a thin layer of the FRP resin matrix visible on the adhesive. Unlike epoxy samples, that suffered UV effects showing a failure modes deterioration, acrylic adhesive maintained for most cases the ruptures observed in un-aged tests, and the same occurred in MET specimens, for both joint configurations. Among non-structural adhesives, PU showed a worsening only in butt joints,

while MS adhesive maintained the best adhesion to adherents: in single-lap specimens, all cohesive failure were registered, and mainly cohesive fractures in butt configuration were observed.
In summary, for the two epoxy adhesives and for PU adhesive, UV radiation generally seemed to deteriorate the adhesion between pultruded laminates and adhesive, changing the failure modes to adhesive. Scarce effects were seen on the others adhesives.

4.5 Discussion

The present study aims to contribute to deepening the knowledge of the ageing degrading mechanisms suffered by different adhesives.
The considered ageing conditions (T_c and T_{uv}) produced almost the same effects on the joints, with a remarkable increase of the joint elongation for all types of adhesives and scarce effects on the ultimate load.
An unexpected result was that all the studied environmental exposures determined a slight increase of load carrying capacity for almost all the tested adhesives. This could be explained by the fact that in the first period of the T_c ageing treatment, specimens were subjected for the first 16 hours to the constant temperature of 40 °C: hence the completion of the polymerization process on the adhesives was achieved, with respect to un-aged samples. This result is consistent with the findings of other authors [8], demonstrating that the exposition of epoxy joints to high temperatures (40 °C) determines an increase of the ultimate load of about 5.6 % with respect to those maintained at room temperatures (23 °C). Moreover, during the T_{uv} ageing, the specimens were inevitably heated by radiations, reaching surface temperature values of about 26 °C. This even small temperature increase could have determined (as occurred for T_c) a slight increase of load carrying capacity, thanks to the cross-linking of the polymer network [22].
In all aged specimens, a great joints elongation and joint stiffness decrease were observed for both T_c and T_{uv} exposures. With regard to specimens exposed to different temperatures, for all tested adhesives the glass transition range was reached and exceeded. Therefore joint stiffness decreased because of the softening of adhesives, with a substantial elasticity modulus decrease during the glass transition [8, 27]. With regard to specimens exposed to the UV radiations, all the tested adhesives demonstrated a scarce UV resistance. This is because of the wavelength of UV radiation, in the range of 90–400 nm, usually cause polymers bond dissociation and the consequent decrease in adhesives elastic modulus [22, 28].
Comparing the different adhesives (Fig. 4.11), EPX1 showed the highest load carrying capacity in all environmental conditions. However, EPX1 specimens tested in shear and tension, after artificial ageing, reached also higher joint elongations than the others, especially those subjected to UV radiations. EPX2 specimens reached lower ultimate loads than EPX1, but higher than other structural adhesives. Moreover, the joint elongations were lower than the previous epoxy adhesive (up to 14 mm for specimens subjected to UV radiation). The choice between the two epoxy adhesives depends on the intended purpose: if

a very high load carrying capacity is required, EPX1 should be used, considering the high deformations that could occur in the structure after ageing. Otherwise, EPX2 should be adopted. In both cases, a protection from UV radiations is recommended to avoid very high adhesive deformations. The bonding efficacy of the adherent-adhesive interface appeared to be negatively affected by high levels of temperatures and humidity, especially in joints bonded with epoxy adhesives, in which the failure modes changed from cohesive to mainly adhesive. This result is consistent with the findings of other authors [6, 8]. Comparing non-structural adhesives, both PU and MS had the similar load carrying capacity, with little difference among un-aged and aged conditions. Joint elongation was on average the highest for PU specimens, which seemed to be very affected by the presence of moisture. MS adhesive resulted in being better than PU, for the lower elongation and the compatibility with substrate, as observed in failure modes (always cohesive).

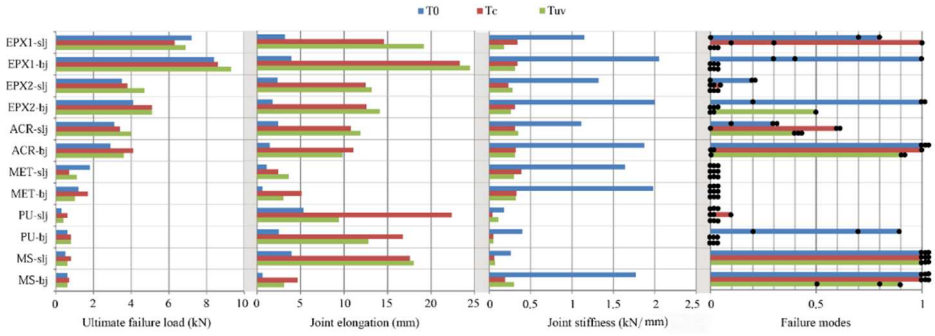

Figure 4.11. Average failure load, joint elongation at failure, joint stiffness and failure modes of specimens under each environmental condition. The failure load ranking was obtained by assigning a value of 0 for undesired adhesive failure, 1 for optimal cohesive failure, and a percentage of cohesive failure for the other mixed collapses. Each point corresponds to one specimen (three for each joint tested).

4.6 Conclusions

This study compares the behavior of six different adhesives for both structural and non-structural connections between GFRP pultruded materials: two epoxy adhesives, one acrylic adhesive, one methacrylate adhesive and two polyurethane adhesives.
Mechanical tests (shear and tensile) were performed in three different environmental conditions: un-aged, after exposure to combined high and low temperatures/moisture levels and under UV radiations.
The results demonstrated that:

- In every environmental condition, all tested adhesives had almost similar load-joint elongation response for single-lap and butt joints. Moreover, for all exposures, epoxy, acrylic and methacrylate adhesives presented an elastic non-linear trend, until a brittle rupture. The first epoxy adhesive demonstrated the highest average shear and tensile strength. Methacrylate adhesive was not an appropriate adhesive for GFRP adherents, with low carrying capacity and brittle behavior. Both polyurethane adhesives exhibited poor load carrying capacity and very high joint elongations compared to the others adhesives, with low curve slopes and softening phenomena after the ultimate stress.

- The two artificial ageing had similar influence on the specimens behavior: a large increase of joints elongation, a slight increase of average failure loads (except for the first epoxy adhesive in single-lap configuration and for methacrylate adhesive) and a significant decrease of the joint stiffness (70÷90 %). For both environmental exposures, the increase of the load carrying capacity could be ascribed to a further polymerization of adhesives for high (40 °C) or slightly high (26 °C) temperatures. The joint stiffness decrease occurred for both environmental ageing with almost the same percentage, for different phenomena. During exposition to cycles of different temperatures and relative humidity, all the adhesives reached the glass transition temperature. During the UV exposure, all the adhesives chemical bonds underwent a dissociation caused by UV wavelengths. Only methacrylate adhesive resulted to be affected by color changing for UV exposure.

- The two artificial ageing had a noticeable influence on the failure modes of the joints. In fact, cycles in climatic chamber changed the failure mode from mixed (for almost all un-aged specimens) to mainly adhesive, except for the second polyurethane adhesive (where the cohesive rupture is maintained). UV radiation seemed to deteriorate the adhesion especially for the two epoxy adhesive and for the first polyurethane adhesive.
In summary, if a structural performance is needed, epoxy adhesives resulted as the best application for GFRP vinyl ester pultruded profiles, in terms of load carrying capacity. However it is necessary to consider the high deformations that could occur, especially under UV exposure.
For non-structural applications, the second polyurethane adhesive was better than the first one, showing similar ultimate loads, but lower deformations and very good compatibility to adherents.

These results suggested some changes to the *Full Glass* window assembly system, particularly the realization of the mobile frame. In fact, in order to avoid undesired deformations of the bonding conjunctions, small metal "L" profiles were inserted in the mobile frame.

4.7 References

[1] Stazi F, Giampaoli M., Rossi M, Munafo P. Environmental ageing on GFRP pultruded joints: Comparison between different adhesives. *Composite Structures* 133 (2015) 404–414

[2] Godat A, Légeron F, Gagné V, Marmion B. Use of FRP pultruded members for electricity transmission towers. *Composite Structures* 105 (2013) 408-421

[3] Turvey G. J. Testing of pultruded glass fibre-reinforced polymer (GFRP) composite materials and structures. Woodhead Publishing Series in *Civil and Structural Engineering* (2013) 440–508

[4] de Castro J, Keller T. Ductile double-lap joints from brittle GFRP laminates and ductile adhesives, part I: experimental investigation. *Composite: part B* 39 (2008) 271-281

[5] Keller T, Tirelli T. Fatigue behavior of adhesively connected pultruded GFRP profiles. Composite Structures 65 (2004) 55-64

[6] Zhang Y, Vassilopoulos A. P, Keller T. Environmental effects on fatigue behavior of adhesively-bonded pultruded structural joints. *Composite Science and Technology* 69 (2009) 1022-1028

[7] de Castro J. Experiments on double-lap joints with Epoxy, polyurethane and ADP adhesives. *Composite Construction Laboratory*, Appendix B – Technical Report n. CCLab2000.1 b/2

[8] Zhang Y, Vassilopoulos A. P, Keller T. Effect of low and high temperatures on tensile behavior of adhesively-bonded GFRP joints. *Composite Structures* 92 (2010) 1631-1639

[9] ISO 4587:2003. Adhesives -Determination of tensile lap-shear strength of rigid-to-rigid bonded assemblies.

[10] Li G, Lee-Sullivan P, Thring R. W. Nonlinear finite element analysis of stress and strain distributions across the adhesive thickness in composite single-lap joints. *Composite structures* 46 (1999) 395-403

[11] Aydin M. D, Ozel A, Temiz S. The effect of adherend thickness on the failure of adhesively-bonded single-lap joints. *Journal Adhesion Science Technology* 19 (2005) 705-718

[12] Cognard J. Y, Creac'hcadec R, Maurice J. Numerical analysis of the stress distribution in single-lap shear tests under elastic assumption-Application to the optimization of the mechanical behavior. *International Journal of Adhesion & Adhesives* 31 (2011) 715-724

[13] DIN EN Norm 10002-1. Metallic materials – Tensile testing. Part 1: Method of test at ambient temperature

[14] EN ISO 527-1:2012. Plastics -Determination of tensile properties – Part 1: General principles

[15] ISO 527-4:2012. Plastics -Determination of tensile properties – Part 4: Test conditions for isotropic and orthotropic fibre-reinforced plastic composites

[16] EN ISO 527-2:2012. Plastics -Determination of tensile properties – Part 2: Test conditions for moulding and extrusion plastics

[17] ASTM D 3418-03. Standard test method for Transition Temperatures of Polymers By Differential Scanning Calorimetry

[18] Chattopadhyay1 D. K, C.Webster D. Thermal stability and flame retardancy of polyurethanes. *Progress in Polymer Science* 34 (2009) 1068–1133

[19] Vega-Baudrit J, Sibaja-Ballestero M, Vazquez P, Torregrosa-Macia R, Martın-Martınez J. M. Properties of thermoplastic polyurethane adhesives containing nanosilicas with different specific surface area and silanol content. *International Journal of Adhesion & Adhesives* 27 (2007) 469–479

[20] EN ISO 9142:2003. Adhesives –Guide to the selection of standard laboratory ageing conditions for testing bonded joints

[21] ASTM D904-99. Standard Practice for Exposure of Adhesive Specimens to Artificial Light

[22] Nguyen T. C, Bai Y, Zhao X. L, Al-Mahaidi R. Effects of ultraviolet radiation and associated elevated temperature on mechanical performance of steel/CFRP double strap joints. *Composite Structures* 94 (2012) 3563-3573

[23] ASTM G154-00a. Standard Practice for operating fluorescent light apparatus for UV exposure of nonmetallic materials

[24] Duncan B, Crocker L, Urquhart J, Arranz E, Mera R, Broughton B. Failure of flexible adhesive joints. NPL Report MATC(A)36 (2011)

[25] ASTM D5573-99 Standard practice for classifying failure modes in fiber-reinforced-plastic (FRP) joints.

[26] Boyd S. W, Winkle I. E, Day A.H. Bonded butt joints in pultruded GRP panels-an experimental study. *International journal of adhesion & adhesion* 24 (2004) 263-275

[27] Bai Y, Nguyen T. C, Zhao X. L, Al-Mahaidi R. Environment assisted degradation of bond between steel and carbon fiber reinforced polymer: a review. *Journal of Materials in Civil Engineering* (2013)

[28] Grassie N, Scott G. Polymer degradation and stabilization. Cambridge: *Cambridge University Press* (1988)

4.8 List of tables and figures

Nomenclature

Figure 4.10. Different types of specimens failure modes: adhesive (a), cohesive (b), mixed (c), light fiber tear (d) failures.
Figure 4.11. Average failure load, joint elongation at failure, joint stiffness and failure modes of specimens under each environmental condition. The failure load ranking was obtained by assigning a value of 0 for undesired adhesive failure, 1 for optimal cohesive failure, and a percentage of cohesive failure for the other mixed collapses. Each point corresponds to one specimen (three for each joint tested).

Chapter 5

On GFRP-steel hybrid bonding systems: mechanical performances before and after the ageing treatments

In this work, the reliability of the *Structural Member* basic principle, i.e. the hybrid system of GFRP pultruded profiles bonded with steel laminates, is verified, with the objective of containing GFRPs deformations. The contents of this chapter will be published in a scientific international journal.

5.1 Abstract

In this paper, the contribution in terms of stiffness increase by coupling steel laminates to GFRP pultruded profiles, through three epoxy adhesives, is investigated. The objective is to verify the applicability of this hybrid system in structural members for curtain walls. Different specimens types were employed in order to investigate on: the compatibility of the bonding system (shear tests on GFRP-steel single lap joints); the response to the local stresses of the bonding system (puncture tests on GFRP-steel squared tubular short profiles); the response to flexural stresses of the bonding system (three-point bending tests on GFRP-steel squared tubular long profiles). The effects of two environmental ageing, continuous condensation and UV radiations, were also analysed. The results demonstrated the compatibility of the bonding system and the stiffness increase of GFRP profiles when the steel reinforcements were applied. Analytical studies were comparable with those observed in the experimental tests, confirming the advantageous method of hybridization. With regard to artificial ageing, the continuous condensation demonstrated the worst effects on the specimens, while better results were registered after the UV radiations. The combinations of the two ageing conditions showed unexpectedly better results, with the enhancement of the mechanical performance of the joints.

Nomenclature

AF	Adhesive failure	L	Steel plate positioned on the lower side of the GFRP profile
A_{GFRP}	Section area of the GFRP profile	$LFTF$	Light-Fiber-Tear Failure
A_{STEEL}	Section area of the steel plate	MF	Mixed failure
A_t	Application temperature	NO	No detachment
B_e	External dimension of the section area's base	$P.D.$	Partial detachment
B_i	Internal dimension of the section area's base	S	Displacement
CF	Cohesive failure	S_t	Service temperature
DIC		$T.D.$	Total detachment
DSC	Differential scanning calorimeter	T_0	Un-aged conditions
$EPX1$	First epoxy adhesive	T_{cc}	Artificial ageing in climatic chamber
$EPX2$	Second epoxy adhesive	T_{eig}	Extrapolated onset temperature
$EPX3$	Third epoxy adhesive	T_{efg}	Extrapolated end temperature
E_t	Young modulus in tension	T_g	Glass transition temperature
E_{GFRP}	Young modulus of GFRP profiles in tension	T_{uv}	Artificial ageing under UV rays
E_{STEEL}	Young modulus of steel plates in tension	U	Steel plate positioned on the upper side of the GFRP profile
F	Load carrying capacity	$U\text{-}I$	Steel plates positioned in the upper-inner side of GFRP profile
H_e	External dimension of the section area's height	UV	Ultraviolet radiations
H_i	Internal dimension of the section area's height	W_t	Working time at 22 °C
I_{GFRP}	Moment of inertia of the GFRP profiles section area	X	The distance of the neutral axis from the barycentre
I_{STEEL}	Moment of inertia of the steel plate section area	ε_t	Tensile strain
k_{GFRP}	Stiffness of the GFRP sample	σ_t	Tensile strength
k_{STEEL}	Stiffness of the steel plate	σ_{ys}	Tensile yield strength
l	Span length	τ	Average shear strength
$K1_{GFRP\text{-}STEEL}$	Stiffness of the GFRP-steel specimen: materials work together		
$k2_{GFRP\text{-}STEEL}$	Stiffness of the GFRP-steel specimen: materials do not collaborate		

5.2 Introduction

Despite the several advantages, it is well known in the literature that GFRP profiles present low elastic modulus with respect to steel (up to ten times lower) [1-4], preventing its use in the civil construction sector [5-7] especially when small profiles size is required, such as in curtain walls.
For this reason, it is necessary to develop suitable approaches to improve the stiffness of the GFRP pultruded material, and some authors demonstrate that coupling GFRP profiles with higher mechanical performances materials, especially steel, is an advantageous method [1,3]. However, to the authors knowledge, validated data for designers are still scarce and there has been little research on the comparison of different types of adhesives used for the joining of GFRP and steel profiles. Furthermore, the evaluation of the influence of environmental ageing was not presented, even if it is well known that bonding connections are adversely influenced by environmental conditions [8-10].

In the present work, an experimental campaign on the connection of GFRP pultruded profiles and steel laminates through three different epoxy adhesives is proposed. The objective is to investigate on three different aspects. (1) The first is the compatibility of the bonding system, through shear tests conducted on small-scale specimens (GFRP-steel single lap joints), also deepening on the effects of two environmental ageing. (2) The second is the response to the local stresses of the bonding system, through puncture resistance tests on full-scale specimens (GFRP-steel squared tubular short profiles) which simulate the local stress transmitted by the curtain panels bolted to the structural members; the effects of two environmental ageing is also carried out. (3) The third is the response to flexural stresses of the bonding system, through three-point bending tests on full-scale specimens (GFRP-steel squared tubular long profiles) which simulate the flexural stresses, undergoes by the whole structural members in curtain walls (i.e. the wind load).

5.3 Methods

5.3.1) Phases

The research includes experimental and analytical studies, divided into the following phases:

- *Experimental tests* were carried out to evaluate both the GFRP-steel compatibility and the steel contribution to enhancing the mechanical performances of the GFRP profiles. The experimental programme comprised: (i) material characterization tests, (ii) shear tests on adhesively bonded GFPR-steel single lap joints, (iii) puncture tests on GFPR-steel squared tubular short specimens and (iv) three-point bending tests on GFPR-steel squared tubular long specimens. The GFRP tubular specimens used in the two latter experimental tests (iii, iv) were adhesively joined to steel plates in three configurations, with the steel plates

positioned in the upper, lower and "upper-inner" sides of the GFRP profiles (Fig.5.1), which are alternative positions of steel laminates with respect to the loading direction. Furthermore, the effect of two environmental ageing, namely continuous condensation and UV exposures, were analysed in steps (ii, iii) of the experimental programme.

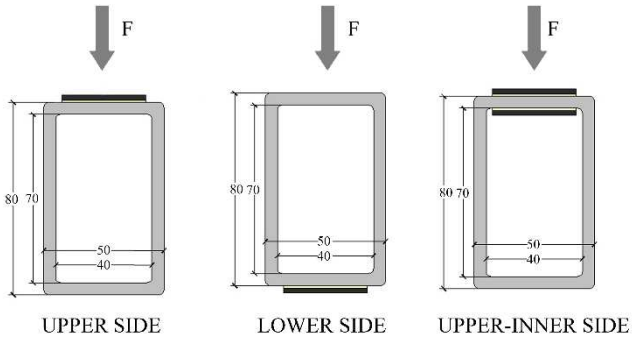

Figure 5.1. GFRP-steel squared tubular specimens in three different configurations, with the steel plates positioned in the upper, lower and "upper-inner" sides of the GFRP profiles.

(i) The materials (GFRP profiles and three epoxy adhesives) characterization tests provided the main mechanical properties of the different components involved in the GFPR-steel composite systems, namely their elasticity modulus, tensile strength, and elongation. The steel mechanical properties (reported in Table 5.1) were obtained from the manufacturer's data sheet.

Table 5.1. GFRP profiles and steel mechanical properties according to manufacturer's data sheets.

GFRP PROFILES [a]			*STEEL PROFILES* [b]			
E_t *(GPa)*	σ_t *(Mpa)*	ε_t *(%)*	E_t *(GPa)*	σ_{ys} *(Mpa)*	σ_t *(Mpa)*	ε_t *(%)*
25.0	250-450	1.0-1.8	198.0	326.7	385.5	29.1

[a] According to ASTM D638 / UNI 5819
[b] According to EN 10025-2: 2004

(ii) The shear tests allowed to evaluate the compatibility between the GFRP and steel and to compare the mechanical behaviour of the single lap joints bonded with three epoxy adhesives, namely their load carrying capacity, displacement, and stiffness.

(iii) The puncture tests permitted to simulate the local stress transmitted by the curtain panels bolted to the GFRP structural members, comparing the load carrying capacity, the displacement and the stiffness of GFRP-steel squared tubular short specimens (with a length of 400 mm) bonded with three epoxy adhesives, in three configurations (Fig.5.1). The

steel plates are used with aim of reinforcing the GFRP bolted area, weakened by the drilling that cuts the composite's fibres.

(iv) The three-point bending tests were performed to simulate the stress of the whole structural member that occurred in curtain walls (when it is subjected to the wind load), comparing the load carrying capacities, the displacements and the stiffness of GFPR-steel squared tubular long specimens (with a length of 1000 mm) bonded with the best adhesive resulted in the previous tests, in three different configurations (Fig.5.1). The steel plates are used with aim of enhancing the flexural stiffness of GFRP profiles.

- *Analytical studies* were carried out to validate the contribution of the steel, adhesively joined to GFRP squared tubular specimens, to the stiffness increase of the GFRP profiles (without reinforcements) in the elastic range. These comprised the calculation of:

- the elastic modulus of the GFRP squared tubular samples without steel plates;
- the stiffness of the GFRP squared tubular samples without steel plates;
- the stiffness of the GFRP-steel squared tubular specimens in two different hypothesis: in the first situation the GFRP and the steel perfectly work together; in the second one, the two material do not collaborate. These calculations were performed for the three different configurations (Fig. 5.1).

The results were finally compared with those obtained through experimental tests (iv).

5.3.2) Experimental tests

5.3.2.1) Material characterization tests

Adherents

The first material is the pultruded E-glass fibre reinforced polyester composite, supplied by Fibrolux, Germany. This material consists of alternating layers of unidirectional fibre roving and chopped strand mat embedded in an isophthalic polyester matrix. A polyester surface veil is used to protect the matrix against environmental actions. The material properties according to manufacturer's data sheet are reported in Table 5.1.

As a result of the pultrusion process, the fibre roving is not uniformly distributed. In order to determine the mechanical properties, GFRP laminates were tested in tension, according to [11,12]. The width of laminates was 25 mm, the thickness 5 mm and the length 100 mm. The free length was 70 mm and the gauge length of the extensometer was set to 50 mm. The tests were performed with a Zwick/Roell Z050 testing machine, using an extensometer to measure the strain and applying a displacement rate of 5 mm/min. Because of the small size of the used specimens, some of them may contain more fibre roving than others, and this produces a scatter in the mechanical properties. For this reason, three specimens were used for each considered ageing conditions that are: no ageing (T_0), exposure to severe humidity and high temperatures (T_{cc}), and exposure to UV radiation (T_{uv}) [8]. The results are summarised in Table 5.2.

The second material is the S235JR steel grade supplied by Termoforgia, Italy. The material properties according to manufacturer data sheet are reported in Table 5.1.

Table 5.2. Mechanical properties in tension of GFRP and steel materials.

Artificial exposure	*GFRP PROFILES*		
	E_t *(GPa)*	σ_t *(Mpa)*	ε_t *(%)*
T_0	29.8 ±2.6	168.8 ±31.1	0.7 ±0.2
T_{cc}	27.1 ±2.6	251.8 ±61.9	0.9 ±0.2
T_{uv}	27.8 ±6.5	199.4 ±91.6	0.8 ±0.3

Adhesives

Three epoxy adhesives were considered in the experimental program, designated EPX1, EPX2, and EPX3. Table 5.3 presents the relative technical and mechanical characteristics, reported from manufacturers. Some technical data were not available.

Table 5.3. Technical and mechanical characteristics of the epoxy adhesives reported by manufacturers.

Adhesive	***EPX1***	***EPX2***	***EPX2***
Chemical base	two-part epoxy adhesive	two-part epoxy adhesive	two-part epoxy adhesive
Consistency	controlled flow	pasty	fluid
W_t *(min)*	>300	120	5-20
A_t *(°C)*	15 to 25	15 to 25	20
S_t *(°C)*	-40+120	-40+80	-40+100
T_g *(°C)*	/	71	/
Surface treatment	sand	sand and degrease	sand and degrease
τ* *(MPa)*	33.5	15	/
σ_t *(Mpa)*	/	17	17
E_t *(MPa)*	/	1700	/
ε_t *(%)*	3	5	/
Use	structural	semi-structural	semi-structural

*On aluminium/steel adherents

In order to determine adhesives mechanical properties, five specimens of each type of adhesive were tested in tension, according to [11, 13]. The dimensions of the dumbbell specimens are shown in Fig. 5.2.

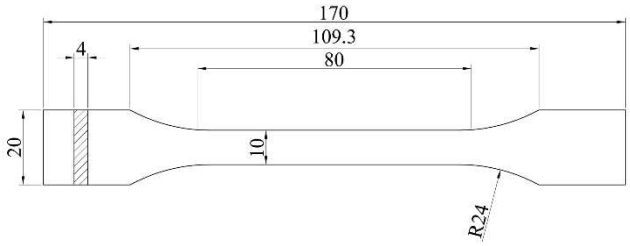

Figure 5.2. Dumbbell specimens dimensions.

All specimens were cured at room temperature for about one month. The results (Table 5.4) were consistent with the data reported by manufacturers, confirming the highest performance of the first epoxy adhesive and the worst load bearing capacity of EPX3, which showed the highest deformability among the tested adhesives.
In order to determine adhesives glass transition temperature (T_g), three samples of each type of adhesive were tested with a differential scanning calorimeter (*DSC*), according to the standard [14]. DSC plots were obtained by heating samples from 25 °C to 120 °C at a rate of 20 °C/min under an inert gas flow of 100 ml/min. The samples weights were in the range of 10 to 15 mg with a precision of 0.01 mg. The T_g was determined (according to procedure 10.2.9 of [14]) as the midpoint temperature between the extrapolated onset temperature (T_{eig}) and the extrapolated end temperature (T_{efg}). The results (Table 5.4) showed that among structural adhesives, EPX2 had the highest T_g (on average 67 °C) and similar temperatures were obtained for EPX1.

Table 5.4. Mechanical properties in tension and glass transition temperatures of the adhesives.

Series	E_t *(MPa)*	σ_t *(Mpa)*	ε_t *(%)*	T_g *(°C)*
EPX1	2966.39 ± 44.12	27.34 ± 0.77	2.39 ± 0.65	61.07 ± 3.34
EPX2	1774.03 ± 30.28	17.11 ± 0.70	3.81 ± 0.23	66.87 ± 0.45
EPX3	648.60 ± 29.56	11.13 ± 1.02	7.26 ± 0.56	46.90 ± 0.63

5.3.2.2) Mechanical tests

Shear tests

The s*ingle lap joints* were manufactured from GFRP and steel laminates bonded with three epoxy adhesives. The geometry of the specimens was manufactured according to [D 4896 –

01]. The width of laminates was 25.4 mm and the length 100 mm; the overlap length was 25.4 mm. The thickness of the GFRP and steel adherents were respectively 5 mm and 3 mm. The test program consisted of a series of twelve specimens per adhesive type, as illustrated in Table 5.5, subdivided according to the ageing condition: four without ageing (T_0), four after exposure to a hot-wet environment (T_{cc}), and four after exposure to UV radiations (T_{uv}). Furthermore, since the tested joints bonded with the EPX1 and EPX2 adhesives resulted in having the best performances, other six specimens per these adhesive types were subjected to two further combined ageing. Three joints were exposed first to the hot-wet environment, and later under UV radiations (T_{cc}+T_{uv}); three joints were subjected first to UV radiations and later to the hot-wet environment (T_{uv}+T_{cc}).
A different bonding thickness among three epoxy adhesives was employed, respectively 0.3 mm, 2 mm and 1mm for EPX1, EPX2 and EPX3 adhesives, as recommended by manufacturers.

Table 5.5. Test programme

Samples	*Adhesive*	*Configuration*	T_0	T_{cc}	T_{uv}	T_{cc}+T_{uv}	T_{uv}+T_{cc}
Single lap joints	EPX1	/	4	4	4	3	3
	EPX2	/	4	4	4	3	3
	EPX3	/	4	4	4	-	-
GFRP-steel squared tubular short specimens	EPX1	U[a]	3	3	-		
		L[b]	3	3	-	-	-
		U-I[c]	3	3	3		
	EPX2	U	3	3	-		
		L	3	3	-	-	-
		U-I	3	3	3		
	EPX3	U	3	3	-		
		L	3	3	-	-	-
		U-I	3	3	3		
	without steel	/	3	-	-	-	-
GFRP-steel squared tubular long specimens	EPX1	U	3				
		L	3	-	-	-	-
		U-I	3				
	without steel	/	3	-	-	-	-

[a] the steel plate positioned on the upper side of the GFRP profile
[b] the steel plate positioned on the lower side of the GFRP profile
[c] the steel plates positioned in the upper-inner side of the GFRP profile

All the tests were implemented on a Zwick/Roell Z050 testing machine of 50 kN capacity under displacements control. Fig. 5.3a shows the setup where specimens were subjected to the shear test. The load was applied at the slow rate of 1.25 mm/min. The elongation was measured by extensometer and the gauge length was set to 55 mm. All specimens were loaded up to the joint failure.

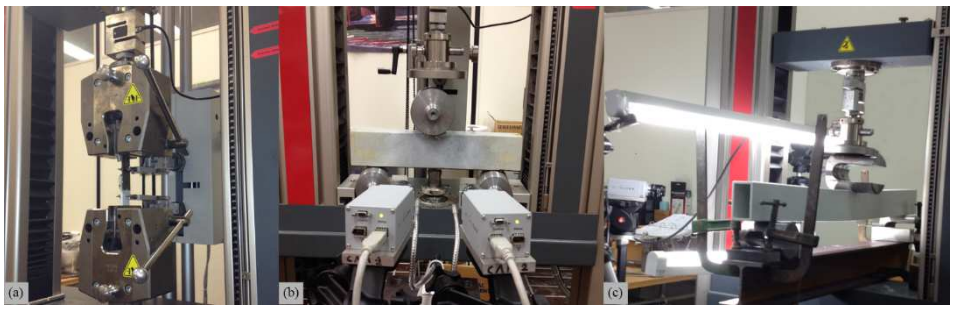

Figure 5.3. Experimental setup: tensile test on GFRP-steel single lap joints (a), puncture resistance test on GFRP-steel squared tubular short specimens (b), bending test on GFRP-steel squared tubular long specimens (c).

Puncture tests

The *GFRP-steel squared tubular short specimens* were manufactured from GFRP squared tubular profiles and steel laminates bonded with three epoxy adhesives. The production method of the specimens was according to a previous study, which studied different joining configuration of steel profiles and CFRP laminates [15]. In the present study the GFRP tubular profiles were adhesively joined to steel plates in three different configurations: with the steel plates positioned in the upper (Fig.5.1a), lower (Fig.5.1b) and "upper-inner" (Fig.5.1c) sides of the GFRP profiles. The section area of the GFRP profiles was 50 X 80 mm^2, the thickness was 5 mm, and the length of the profiles was 400 mm. The geometry of the steel plates was 35 X 400 mm^2, and the thickness was 2 mm.
The test program consisted of a series of twenty-one specimens per adhesive type, as illustrated in Table 5.5, subdivided according to the ageing condition: nine without ageing (T_0), nine after exposure to a hot-wet environment (T_{cc}), and three after exposure to UV radiations (T_{uv}). The influence of the UV exposure was analysed only on the specimens in the "upper-inner" configuration, which presented the highest amount of adhesive. For the three adhesives, the same bonding thickness used in the single lap joints was employed.
To the sake of comparison, three GFRP squared tubular specimens without the steel reinforcement (with the same geometry) were tested.
All the tests were implemented on a Zwick/Roell Z050 testing machine of 50 kN capacity under displacements control. Fig. 5.3b shows the three-point bending setup where specimens were subjected to the puncture test. The load was applied at the slow rate of 3 mm/min. The displacement in the lower side of the profiles was recorded every 1.68 s using two video camera data logger (Fig. 5.3b), (DIC method), until the specimens failure.

Three-point bending tests

The *GFRP-steel squared tubular long specimens* were manufactured from GFRP squared tubular profiles and steel laminates bonded with the best adhesive (EPX1) resulted in the previous tests. The same production method of the specimens studied in the puncture resistance test was followed. The section area of the GFRP profiles was 50 X 80 mm^2, the thickness was 5 mm, and the length of the profiles was 1000 mm. The geometry of the steel plates was 35 X 1000 mm^2, and the thickness was 2 mm.
The test program (Table 5.5) consisted of a series of nine specimens subdivided according to the geometry configuration: three with the steel plates positioned on the upper side (Fig. 5.1a), three on the lower side (Fig. 5.1b) and three on the "upper-inner" side (Fig. 5.1c) of the GFRP profiles. The 0.3 mm bonding thickness was employed for all the specimens.
To the sake of comparison, three GFRP squared tubular specimens without the steel reinforcement (with the same geometry) were tested.
All the tests were implemented on a Zwick/Roell Z050 testing machine of 50 kN capacity under displacements control. Fig. 5.3c shows the three-point bending setup where specimens, in all the different configurations, were subjected to the bending test. The load was applied at the slow rate of 3 mm/min. The displacement in the lower side of the profiles was recorded every 1.68 s using two video camera data logger (Fig. 5.3c), (DIC method), until the specimens failure.

5.3.2.3) Artificial ageing

Two types of ageing were taken into account, one to reproduce the external environment exposure (T_{cc}) and another to reproduce the UV irradiation effect (T_{uv}).
The simultaneous exposure to heat and high humidity levels is one of the most harmful condition of adhesives and plastics [9, 10]. This external environment exposure (T_{cc}) was simulated using a climatic chamber "Angelantoni" CST-130 S model (Fig. 5.4a). A total number of thirty-nine samples (twelve single lap joints and twenty-seven squared tubular short specimens) were aged at the constant temperature of 40 °C and at the relative humidity of 100 %, according to ISO 6270-2 [16], for six months without interruption.
The exposition to UV radiations can dissociate the molecule bonds in most polymers, leading to the degradation of polymeric materials [17]. This ageing type (T_{uv}) was simulated using eight fluorescent UV lamps (Philips Actinic BL TL-D). A total number of eleven samples (five single lap joints and six squared tubular short specimens) were aged according to [18] with some adaptations. In fact, as highlighted in a previous work [8], the effects of high temperatures (40 °C) are much more relevant than those of UV rays. So these two extreme environmental conditions should be separately analysed to deepen the UV influence alone. The specimens were subjected to high UV radiations but under laboratory conditions (temperature of 21 °C, relative humidity of 33 %). The recorded temperature on specimens surface was about 26 °C. The samples were placed inside a wooden structure equipped with three lamps at the top, three at the bottom and two at the sides (Fig. 5.4b), in order to guarantee a uniform distribution of irradiation on the bonding area. The lamps emitted on a

wavelength in the range of 340-400 nm [19], with a peak at 370 nm, producing a UV irradiance between 41 and 45 W/m² on the specimens surfaces. Cycle II of 24 hours [18] was repeated 42 times (overall 1000 hours) without interruption.
Furthermore, the coupling of the two previous artificial exposures was investigated, in order to analyse the effects of the combined ageing conditions in single lap joints bonded with the two adhesives resulted with the best performance (EPX1 and EPX2), also in different sequences (T_{cc}+T_{uv}, T_{uv}+T_{cc}). The test programme per each adhesive is the following (see Table 5.5): three samples were firstly subjected to high humidity and temperatures levels (for six months), and later under UV radiations (for 1000 hours); other three samples underwent UV radiations (for 1000 hours) and then they were exposed to high humidity and temperatures levels (for six months).

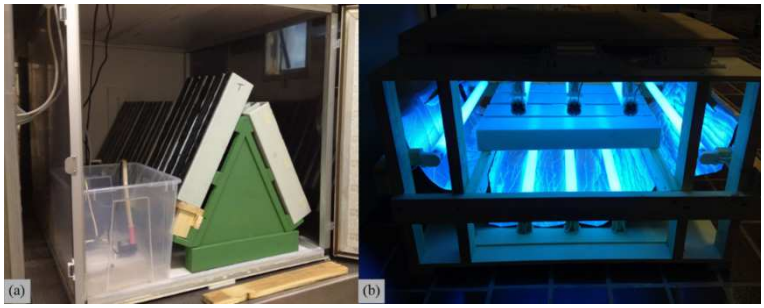

Figure 5.4. Specimens subjected to the ageing conditions: the hot-wet environment in the climatic chamber (a) and the UV radiation in the wooden structure equipped with lamps (b).

5.3.3) Analytical studies

Analytical calculations of the samples stiffness aim to check the results obtained through the previous experimental tests and to validate the contribution of the steel, adhesively joined to GFRP squared tubular specimens, to the increase of the stiffness of the GFRP profiles in the elastic range. The following parameters were calculated:

1. The elastic modulus of the GFRP squared tubular long profiles.

The elastic modulus $\mathbf{E_{GFRP}}$ [MPa] of the GFRP profiles was obtained through the following formula:

$$E_{GFRP} = l^3 F / (48 I_{GFRP} S) \quad (1)$$

where: l [mm] is the span length, F [N] is the load carrying capacity and s [mm] is the displacement of the GFRP profiles: these latter two parameters are the maximum values registered after experimental tests in the elastic ranges. $\mathbf{I_{GFRP}}$ [mm^4] is the moment of inertia

of the GFRP profiles section areas that, in this case, is symmetrical with respect to both x and y-axis, and it is calculated through the following formula:

$$\boldsymbol{I_{GFRP}} = B_e H_e^3 /12 - B_i H_i^3 /12 \quad (2)$$

where: B_e and B_i [mm] are respectively the external and internal dimension of the section area's base, H_e and H_i [mm] are respectively the external and internal dimension of the section area's height.

2. The stiffness of the GFRP squared tubular long profiles.

The stiffness $\mathbf{k_{GFRP}}$ [N/mm] of the GFRP samples without the steel reinforcement was calculated through the following formula:

$$\boldsymbol{k_{GFRP}} = 48\, E_{GFRP}\, I_{GFRP} / l^3 \quad (3)$$

3. The stiffness of the GFRP-steel squared tubular long profiles.

The stiffness $\mathbf{k_{GFRP\text{-}STEEL}}$ [N/mm] of the GFRP-steel bonding system was calculated in two different hypothesis: in the first case, the GFRP and the steel perfectly work together **($\mathbf{k1_{GFRP\text{-}STEEL}}$)**; in the second one, the two material do not collaborate **($\mathbf{k2_{GFRP\text{-}STEEL}}$)**. These calculations were performed for the three different configurations of the specimens (Fig. 5.1): the formulas used in the upper and in the lower configurations differ from those employed in the upper-inner configuration, due to the relative different distance of the neutral axis from the barycentre of the sections (see Fig. 5.5).

3.1 Upper and lower configurations: GFRP and steel work together

$$\boldsymbol{k1^{UL}_{GFRP\text{-}STEEL}} = k^{UL}_{GFRP} + k^{UL}_{STEEL} = 48\, E_{GFRP}\, I^{UL}_{GFRP} / l^3 + 48\, E_{STEEL}\, I^{UL}_{STEEL} / l^3 \quad (4)$$

where: E_{STEEL} [MPa] is the elastic modulus of the steel (see Table 1); $\mathbf{I^{UL}_{GFRP}}$ [mm^4] and $\mathbf{I^{UL}_{STEEL}}$ [mm^4] are respectively the moments of inertia of the GFRP and steel profiles section areas; the latter two parameters were calculated through the following formulas:

$$\boldsymbol{I^{UL}_{GFRP}} = I_{GFRP} + A_{GFRP} X^2 \quad (5)$$

$$\boldsymbol{I^{UL}_{STEEL}} = I_{STEEL} + A_{STEEL}[(H_e/2 - X) + (S_{STEEL}/2)]^2 = (B_i\, S^3{}_{STEEL})/12 + A_{STEEL}[(H_e/2 - X) + (S_{STEEL}/2)]^2 \quad (6)$$

where: A_{GFRP} [mm^2] and A_{STEEL} [mm^2] are respectively the section areas of the GFRP and steel profiles; S_{STEEL} [mm] is the thickness of the steel profile; $\mathbf{X^{UL}}$ [mm] is the distance of

the neutral axis from the barycentre calculated through the following formula (see Fig. 5a and 5b):

$$\boldsymbol{X^{UL}} = (E_{STEEL}\, B_i\, S_{STEEL}\, H_e/2 + E_{STEEL}\, B_i\, S^2_{STEEL}/2) / (2E_{GFRP}\, H_e\, S_{GFRP} + 2E_{GFRP}\, B_i\, S_{GFRP} + E_{STEEL}\, B_i\, S_{STEEL}) \quad (7)$$

where: S_{GFRP} [mm] is the thickness of the GFRP profile.

3.2 Upper and lower configurations: GFRP and steel do not collaborate

$$\boldsymbol{k2^{UL}_{GFRP\text{-}STEEL}} = k_{GFRP} + k_{STEEL} = 48\, E_{GFRP}\, I_{GFRP}/l^3 + 48\, E_{STEEL}\, I_{STEEL}/l^3 \quad (8)$$

3.3 Upper-inner configuration: GFRP and steel work together

$$\boldsymbol{k1^{UI}_{GFRP\text{-}STEEL}} = k^{UI}_{GFRP} + k^{UI}_{STEEL} = 48\, E_{GFRP}\, I^{UI}_{GFRP}/l^3 + 48\, E_{STEEL}\, I^{UI}_{STEEL}/l^3 \quad (9)$$

where: $\mathbf{I^{UI}_{GFRP}}$ [mm^4] and $\mathbf{I^{UI}_{STEEL}}$ [mm^4] are respectively the moments of inertia of the GFRP and steel profiles section areas; the latter two parameters were calculated through the following formulas:

$$\boldsymbol{I^{UI}_{GFRP}} = I_{GFRP} + A_{GFRP} X^2 \quad (10)$$

$$\boldsymbol{I^{UI}_{STEEL}} = I^{UI1}_{STEEL} + I^{UI2}_{STEEL} =$$

$$I_{STEEL} + A_{STEEL}[(H_e/2 - X) + (S_{STEEL}/2)]^2 + I_{STEEL} + A_{STEEL}(H_e/2 - X - S_{GFRP} - S_{STEEL}/2)^2 \quad (11)$$

where: $\mathbf{X^{UI}}$ [mm] is the distance of the neutral axis from the barycentre calculated through the following formula (see Fig. 5c):

$$\mathbf{X^{UI}} = (E_{STEEL}\, B_i\, S_{STEEL}\, H_e - E_{STEEL}\, B_i\, S_{GFRP}\, S_{STEEL}) / (2E_{GFRP}\, H_e\, S_{GFRP} + 2E_{GFRP}\, B_i\, S_{GFRP} + 2E_{STEEL}\, B_i\, S_{STEEL}) \quad (12)$$

3.4 Upper-inner configuration: GFRP and steel do not collaborate

$$\boldsymbol{k2^{UI}_{GFRP\text{-}STEEL}} = k_{GFRP} + 2\, k_{STEEL} = 48\, E_{GFRP}\, I_{GFRP}/l^3 + 2\,(48\, E_{STEEL}\, I_{STEEL}/L^3) \quad (13)$$

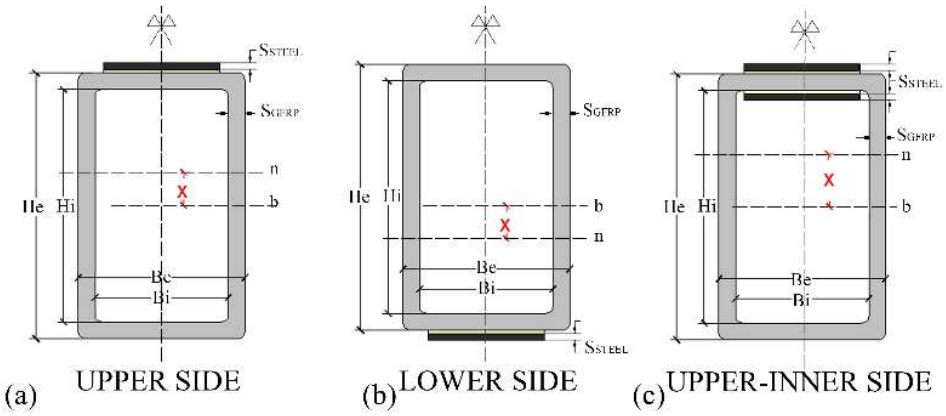

Figure 5.5. GFRP-steel squared tubular specimens in three different configurations: different positions of the neutral axis (n) with respect to the barycentre (b).

5.4 Experimental results

In this section, the mechanical responses and the failure modes of all the GFRP-steel specimens (single lap joints, squared tubular short and long profiles) are presented and analysed. The results are subdivided according to mechanical tests typology.

5.4.1) Shear tests

5.4.1.1) Mechanical performance

Table 5.6 shows the average results of un-aged (as produced) and aged GFRP-steel single lap joints, subjected to shear tests: the load carrying capacities (N), the displacements (mm) and the stiffness (kN/mm) are presented. The load-displacement trends of the specimens bonded with the three epoxy adhesives are showed in figure 5.6.
With regard to *un-aged samples* (T_0), the *load* carrying capacity of the specimens bonded with the first epoxy adhesive (EPX1) resulted in the highest value, in particular twice than the EPX3 joints. However, the latter adhesive registered the best *stiffness* result, with a value of about 32500 N/mm. Very similar data were observed in the other two adhesives.
With regard to *aged* samples, the continuous condensation treatment (T_{cc}) demonstrated higher negative effects on the mechanical responses of the joints than the UV exposure (T_{uv}). In the previous ageing condition, in fact, all the joints, registered *load* decreasing values, up to 50 % for EPX3 adhesive, while in the latter one (T_{uv}), increments of the data were showed (especially for EPX3).

Table 5.6. Mechanical properties of GFRP-steel single lap joints bonded with three different adhesives: results before (T_0) and after (T_{cc}, T_{uv}, T_{cc}+T_{uv}, T_{uv}+T_{cc}) the ageing treatments.

Adhesive	*Ageing condition*	*EPX1*	*EPX2*	*EPX3*
LOAD	T_0 (N)	5052.70 ± 1505.86	2818.54 ± 774.91	2480.49 ± 253.30
	T_{cc} (%)	- 15.20	- 25.70	- 51.49
	T_{uv} (%)	+ 15.54	+ 21.37	+ 24.63
	T_{cc} + T_{uv} (%)	+ 29.12	- 15.95	-
	T_{uv} + T_{cc} (%)	+ 21.65	+ 36.60	-
DISPL.	T_0 (mm)	0.20 ± 0.06	0.12 ± 0.03	0.10 ± 0.01
	T_{cc} (%)	+ 92.96	+ 68.94	+ 561.97
	T_{uv} (%)	+ 6.58	+ 88.82	+ 78.71
	T_{cc} + T_{uv} (%)	+ 18.70	- 15.39	-
	T_{uv} + T_{cc} (%)	+ 12.79	+ 20.62	-
STIFFNESS	T_0 (N/mm)	30694.25 ± 4291.36	30909.75 ± 2557.24	32549.75 ± 2736.74
	T_{cc} (%)	- 93.53	- 84.96	- 92.45
	T_{uv} (%)	- 20.03	- 32.13	- 37.63
	T_{cc} + T_{uv} (%)	+ 19.80	- 14.41	-
	T_{uv} + T_{cc} (%)	+ 11.26	+ 6.71	-

The *displacements* recorded by the specimens showed very high increments in both the ageing treatments, especially after the hot-wet (T_{cc}) exposure. The only exception was the first epoxy adhesive after the UV treatment that demonstrated a slight increment of 6.58 %.
The *stiffness* of the joints, after the continuous condensation treatment, resulted considerably worsened, with decrements of about 90 % for all the adhesives. Better results (about -30 %) were observed for the specimens that underwent the UV radiations and EPX1 adhesive showed the best behaviour.

With regard to the *combination* of the *environmental conditions*, both the ageing treatments (T_{cc}+T_{uv} and T_{uv}+T_{cc}) showed better effects on the mechanical responses of the joints than those registered in the previous ageing conditions (T_{cc} and T_{uv}). The best results were obtained after the T_{uv}+T_{cc} exposure: the load carrying capacity registered increments up to 36 % for the second epoxy adhesive (EPX2) and increased stiffness were observed for all the joints. In the other environmental condition (T_{cc}+T_{uv}), the best results were registered by EPX1, both in the load carrying capacity (+29 %) and the stiffness (+20 %) values, while negative effects were showed by EPX2 (respectively of -16% and -14 %).
By comparing the tested adhesives, EPX1 demonstrated the best mechanical performance both in un-aged and aged conditions, registering the highest load carrying capacity. With regard to the stiffness, after the hot wet condition, it showed lower decreasing values than those registered under the UV radiations. Both the ageing combinations improved the mechanical properties of the adhesive, especially when the specimens were firstly subjected to high humidity and temperatures levels and later under UV radiations (T_{cc}+T_{uv}).

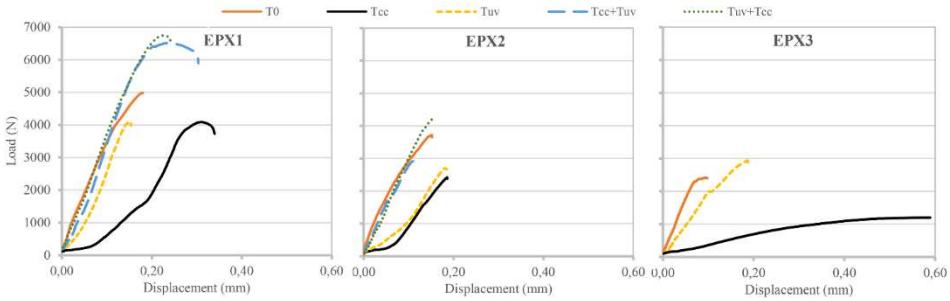

Figure 5.6. Representative load-displacement trends of GFRP-steel single lap joints before (T_0) and after the ageing treatments (T_{cc}, T_{uv}, T_{cc}+T_{uv}, T_{uv}+T_{cc}): comparison of three different epoxy adhesives.

5.4.1.2) Failure modes

Fig. 5.7 shows four types of failure modes occurred during specimens mechanical tests and classified according to [19]. The first is an "Adhesive Failure" (*AF* - Fig. 5.7a) and occurred at the interface between the adherend and the adhesive, this is usually not accepted in adhesive technology [20]. The second is a "Cohesive Failure" (*CF* - Fig. 5.7b), occurring within the adhesive layer: this reveals a good compatibility between adhesive and adherents. In the third figure (Fig. 5.7c) a "Light-Fiber-Tear Failure" (*LFTF*) is presented and occurred within the GFRP adherent, with few glass fibres transferred from the adherent to the adhesive. In Fig. 5.7d there is an example of "Mixed Failure" (*MF*), combining two of the failure modes described above.

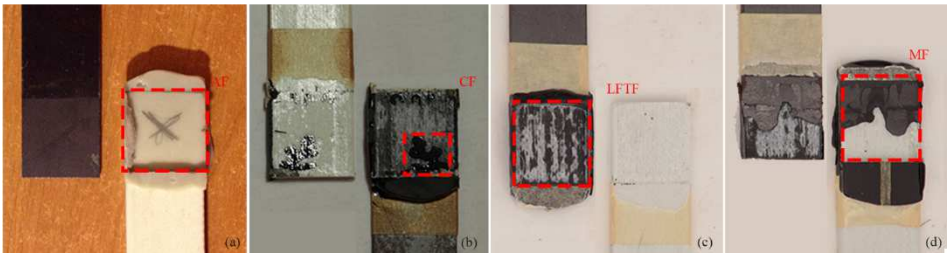

Figure 5.7. Failure modes of GFRP-steel single lap joints: adhesive AF (a), cohesive CF (b), light-fiber-tear LFTF (c) mixed MF (d) failures.

The percentage of fracture mode was evaluated by a graphical estimation. Table 5.7 shows the results of un-aged and aged specimens.
In the *un-aged* condition (T_0), the joints bonded with EPX1 showed the best performance since the LFTF failure modes mostly occurred. In this case, in fact, the optimum adhesion

between the adherents led to the delamination of the GFRP profiles. The worst behaviour was registered by EPX3 that showed all adhesive failures.
After the *ageing* treatments (T_{cc} and T_{uv}), very similar effects were registered by all the adhesives. The first epoxy showed slight worsening of the performance especially after the UV exposure, with almost adhesive – light fibre tear failures. EPX2 joints presented a decrease of the data with all adhesive fractures and, EPX3 confirmed the un-aged results.
After the *combination* of the *ageing* treatments (T_{cc}+T_{uv} and T_{uv}+T_{cc}), all the specimens showed a slight enhancement of the performance than those registered in the previous ageing conditions (T_{cc} and T_{uv}). Similar results were registered in the two artificial exposures: the first epoxy adhesive presented almost all mixed failure modes, with a high percentage of the LFTF type. The second epoxy showed little percentages of cohesive failures even if the main fracture type remained the adhesive one.

Table 5.7. Failure modes of GFRP-steel single lap joints: results before (T_0) and after the ageing (T_{cc}, T_{uv}, T_{cc}+T_{uv}, T_{uv}+T_{cc}) treatments: adhesive (AF), cohesive (CF), mixed (MF), light-fiber-tear (LFTF) failures.

	T_0	T_{cc}	T_{uv}	$T_{cc} + T_{uv}$	$T_{uv} + T_{cc}$
EPX1	3 LFTF 1 MF (20% LFTF, 80% AF)	2 LFTF 1 MF (90% LFTF, 10% AF) 1 MF (85% LFTF, 15% AF)	1 LFTF 2 MF (40% LFTF, 60% AF) 1 MF (20% LFTF, 80% AF)	1 LFTF 1 MF (50% LFTF, 50% AF) 1 MF (95% LFTF, 5% CF)	1 LFTF 2 MF (80% LFTF, 20% AF)
EPX2	1 LFTF 3 AF	4 AF	4 AF	1 AF 1 MF (90% AF, 10% CF) 1 M (95% AF, 5% CF)	2 AF 1 MF (95% AF; 5% CF)
EPX3	4 AF	4 AF	4 AF	/	/

Table 5.8. Mechanical properties of GFRP squared short specimens, with and without the steel reinforcement: results before (T_0) and after (T_{cc}, T_{uv}) the ageing treatments.

Adhesive	***Configuration***	***Load***				***Displacement***				***Stiffness***			
		T_0 (N)	dev.st.	T_{cc} (%)	T_{uv} (%)	T_0 (mm)	dev.st.	T_{cc} (%)	T_{uv} (%)	T_0 (N/mm)	dev.st.	T_{cc} (%)	T_{uv} (%)
EPX1	U	15859,21	±2434.83	-17,38	-	0,98	±0.21	+28,32	-	18599,89	±1906.98	-30,41	-
	L	12338,46	±1603.75	-3,26	-	0,79	±0.14	+74,48	-	18249,46	±2611.05	-36,05	-
	U-I	11238,64	±2363.16	+5,39	+18,81	0,61	±0.09	+60,36	+57,72	22552,05	±4389.90	-43,63	-40,04
EPX2	U	11900,37	±782.53	-25,95	-	0,78	±0.07	+11,34	-	16282,86	±1630.84	-40,33	-
	L	13874,00	±1173.74	-16,71	-	1,01	±0.04	+37,28	-	15041,12	±816.01	-9,35	-
	U-I	12351,41	±810.21	-31,74	-22,13	0,62	±0.04	-13,54	-7,27	21554,12	±991.69	-30,17	-19,73
EPX3	U	7959,96	±1794.53	-29,02	-	0,48	±0.06	-3,81	-	19861,34	±2744.33	-9,31	-
	L	13974,55	±417.86	-24,56	-	1,76	±0.14	+17,15	-	15512,10	±264.05	-49,71	-
	U-I	7643,22	±313.21	-20,42	+1,78	0,50	±0.21	-8,38	-1,97	20345,13	±6162.22	-28,23	-17,56
Without steel		14556,56	±347.10	-	-	1,06	±0.06	-	-	12647,50	±92.63		

5.4.2 Puncture tests

5.4.2.1 Mechanical performance

Table 5.8 shows the average results of un-aged (as produced) and aged GFRP-steel squared tubular short specimens, subjected to puncture tests: the load carrying capacities (N), the displacements (mm) and the stiffness (kN/mm) are presented. The considered values are the maximum data recorded in the elastic range. Per each adhesive type, all the specimen's configurations (upper, lower and upper-inner) are compared to GFRP profiles tested without the steel reinforcements.

With regard to *un-aged samples* (T_0), the *load* carrying capacity of the hybrid specimens resulted always lower than those of the un-reinforced GFRP profiles: this is because, during the load application, the steel plates penetrated inside the samples, indenting the composite's surfaces and weakening the performance of the bonding systems. The only exceptions were the specimens in the upper configuration bonded with EPX1 adhesive, registering the best behaviour. With regard to EPX2 and EPX3, the specimens in the lower configuration showed the highest results, with very similar values.

The *displacements* recorded by the GFRP-steel samples presented almost all lower values than the un-reinforced ones, especially the specimens bonded with EPX3 adhesive in the upper and upper-inner configurations.

The *stiffness*, as expected, of the steel reinforced specimens were always higher than the un-reinforced ones, for every configuration and tested adhesives. The best results were showed by specimens in the upper-inner configurations, and the highest value was again registered by EPX1 adhesive.

The same conclusions could be drawn analysing the load-displacement trends, in the elastic range (Fig. 5.8), of representative specimens. On the other hand, in the plastic range, the un-reinforced GFRP profile showed better performance than the hybrid ones, declaring mostly higher load carrying capacity and stiffness values. This is because of the steel plates, indenting the GFRP surfaces, worsened the mechanical response of the composites profiles, in the long term.

With regard to *aged* samples (T_{cc} and T_{uv}), the two artificial treatments had similar effects on the mechanical responses of the hybrid specimens, which resulted generally worsened. A lowered *load* carrying capacity was showed, with decrements up to 30 %, with some exceptions: the UV treatments, in fact, increased the performance of the samples bonded with EPX1 adhesive of about 19 % and a little increment was also registered by EPX3 adhesive.

The *displacements* resulted increased in almost all the GFRP-steel specimens, and the highest results were recorded by the samples bonded with EPX1 adhesive (of about 60 %), both after T_{cc} and T_{uv} treatments. Therefore, very high *stiffness* decrease was registered by the hybrid specimens, for all the configurations and tested adhesives.

On the other hand, as showed in figures 5.9 and 5.10, aged specimens maintained higher stiffness in the elastic range than un-reinforced GFRP samples, especially after UV

radiations. The only exceptions were presented by the hybrid profiles in the lower configuration, which showed the lowest trend also in initial conditions (T_0).

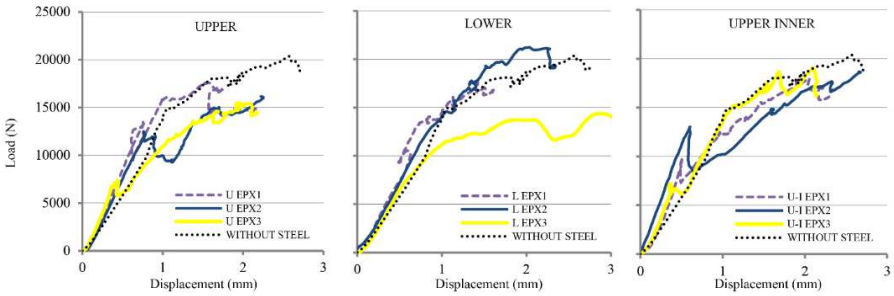

Figure 5.8. Representative load-displacement trends of GFRP-steel squared tubular short specimens, bonded with three epoxy adhesives, in un-aged condition (T_0): comparison of the three different configurations with the un-reinforced profile.

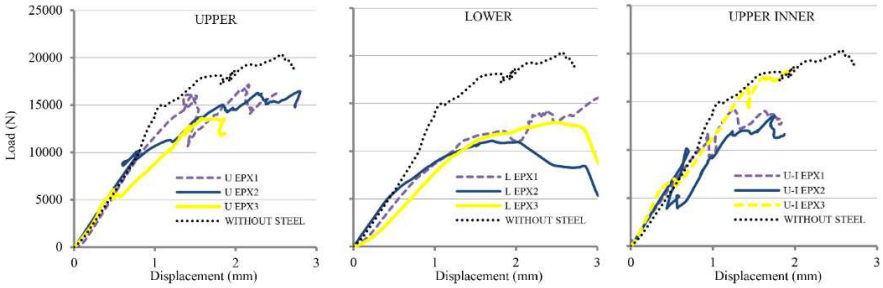

Figure 5.9. Representative load-displacement trends of GFRP-steel squared tubular short specimens, bonded with three epoxy adhesives, after the continuous condensation treatment (T_{cc}): comparison of the three different configurations with the un-reinforced profile.

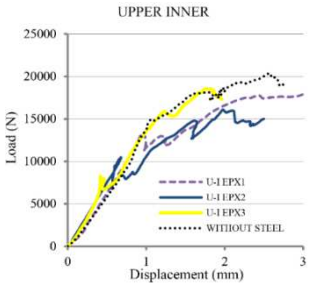

Figure 5.10. Representative load-displacement trends of GFRP-steel squared tubular short specimens in the upper-inner configuration, after the UV exposure (T_{uv}): comparison of three epoxy adhesives with the un-reinforced profile.

These results confirmed the advantageous method of hybridization, even when the bonding system is exposed to adverse environmental conditions. By comparing the tested adhesives, EPX1 demonstrated the best mechanical characteristics in un-aged condition and, even if it presented the highest decrements after ageing, it maintained the better performance in terms of load carrying capacity and stiffness values, with respect to the other tested adhesives.

5.4.2.2) Failure modes

Fig. 5.11a presents the typical cracks occurred in GFRP profiles, both in un-reinforced and hybrid specimens after puncture tests: in the compression zone, the loading member caused structural deformations along the z-axis and web-flange separations with a 45° interlaminar shear crack at each corner of the pultruded GFRP section occurred [1]. As showed in Fig. 5.11b, the GFRP-steel specimens in the upper and upper-inner configurations presented greater structural deformations, since the steel laminate penetrated inside the GFRP profile during the load application.

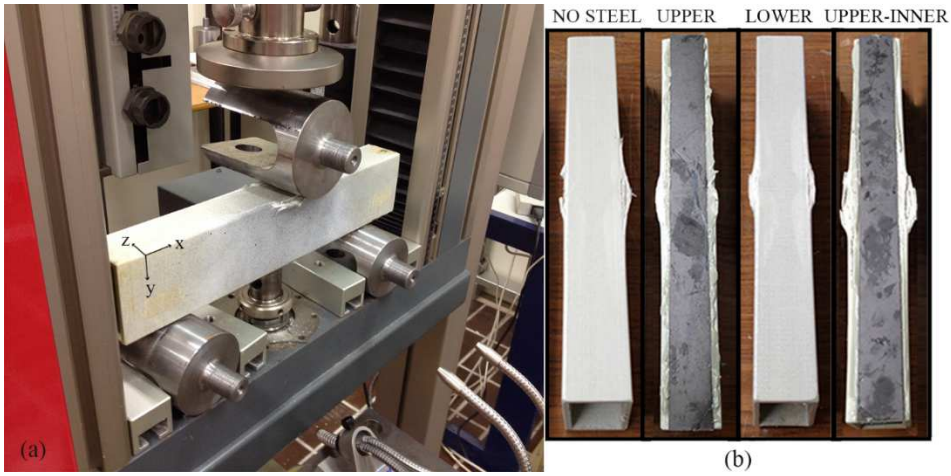

Figure 5.11. Failure modes of GFRP-steel squared tubular short specimens: typical cracks (a) and comparison of un-reinforcement samples with reinforced ones in the three different configurations (b).

With regard to GFRP-steel bonding conjunctions, the failure modes occurred always in the "adhesive" type (according to the classification of ASTM D5573-99 [19]). The hybrid specimens, for the tested adhesive in three different configurations, registered different behaviours. Table 5.9 shows the results before and after the ageing treatments.

Table 5.9. Failure modes of GFRP squared short specimens with the steel reinforcement: results before (T_0) and after (T_{cc}, T_{uv}) the ageing treatments: partial detachment (P.D.), total detachment (T.D), no detachment (NO) of the steel laminates.

	T_0			T_{cc}			T_{uv}
	U	**L**	**U-I***	**U**	**L**	**U-I***	**U-I***
EPX1	NO	NO	75% P.D.	NO	NO	P. D.	50% P.D.
EPX2	NO	NO	P.D.	NO	NO	50% P.D. 50% T.D.	50% P.D.
EPX3	35% P.D.	P.D.	T.D.	NO	P.D.	NO	T.D.

*The detachment occurred only for the steel laminate positioned in the inner side of the squared tubular profiles.

In the *un-aged* condition (T_0), EPX1 and EPX2 presented very similar behaviours: in the upper and lower configurations, any detachment occurred between GFRP and steel profiles, while in the upper-inner configuration the first epoxy adhesive showed a better performance of about 25%. The worst results were registered by EPX3 with the separation of the steel laminate in all the cases.
After the *continuous condensation* (T_{cc}) treatment, very similar results than the un-aged condition were showed by EPX1 and EPX2, with a slight worsening of the failure modes in the upper-inner configuration. An unexpected behaviour was observed for EPX3 that improved its performance when the steel laminates were positioned in the upper and upper-inner sides of the GFRP profiles.
After the *UV* (T_{uv}) exposure, better results than the un-aged condition were registered by EPX1 and EPX2, while EPX3 showed the same behaviour.

5.4.3) Three-point bending tests

5.4.3.1) Mechanical performance

Table 5.10 shows the average results of GFRP-steel squared tubular long specimens subjected to three-point bending test: the load carrying capacities (N), the displacements (mm) and the stiffness (kN/mm) are presented. The considered values are the maximum data recorded in the elastic range. All the specimen's configurations (upper, lower and upper-inner), bonded with the best adhesive resulted in the previous experiments, are compared to GFRP profiles tested without the steel reinforcements.
The *load* carrying capacity of the hybrid specimens was higher than the un-reinforced GFRP profiles for the upper and lower configurations, respectively of about 7 % and 10 %. For the samples with the steel laminates positioned in the upper-inner side of the GFRP profile, the result was very similar.
The *displacements* recorded by the GFRP-steel samples presented all lower values than the un-reinforced ones, especially the specimens in the upper-inner configuration.

The *stiffness* of the steel reinforced specimens was always the highest, for every configuration.
The specimens in the lower configuration registered the best increment, of about 80 %. In fact, the lower side of the GFRP profile was subjected to the tensile stresses and the steel reinforcement allowed higher containment of the deformations than in the other positions.
To summarise, also in the three-point bending tests, the steel reinforcement allowed to increase the mechanical performance of the GFRP squared tubular profiles, in particular in the lower configuration.

Table 5.10. Mechanical properties of GFRP squared long specimens, with and without the steel reinforcement.

Adhesive	***Configuration***	***Load*** (N)			***Displacement*** (mm)			***Stiffness*** (N/mm)		
		medium	dev.st.	Δ*(%)	medium	dev.st.	Δ*(%)	medium	dev.st.	Δ*(%)
EPX1	U	15493.99	±1147.18	+7.14	6.60	±0.59	-16.82	3466.85	±42.64	+30.52
	L	15909.07	±846.70	+10.01	6.92	±0.67	-12.75	4834.80	±685.26	+82.02
	U-I	14429.68	±531.00	-0.22	5.64	±0.82	-28.92	3925.90	±14.00	+47.80
Without steel		14462.12	±766.92	-	7.94	±1.29	-	2656.15	±21.28	-

* the percentage variation is respect to the un-reinforced specimens (without steel).

5.4.3.2) Failure modes

After three-point bending tests, similar failure modes occurred in GFRP profiles, both in un-reinforced and hybrid specimens. Analogue failures than the squared tubular short profiles (section 5.4.2.2) were observed, with the only difference of the cracks propagation length. In this case, in fact, the high stiffness due to the geometry of the profiles (length of 1000 mm) allowed obtaining lower structural deformations than the shorter ones (400 mm). Furthermore, with respect to the previous puncture tests, any detachment of the steel plates was observed for all the configurations.

5.5 Analytical results

The stiffness results for the GFRP-steel squared tubular long specimens, obtained through analytical calculations, were comparable with those observed in the experimental tests and confirmed the enhancement of the GFRP mechanical response thanks to the steel contribution.
With regard to the *un-reinforced* GFRP profile, the stiffness calculation was consistent with the experimental result, respectively 2664.50 N/mm and 2656.15 N/mm.
About the *reinforced* specimens, the stiffness obtained in the case of the GFRP-steel perfect collaboration demonstrated the highest value in the upper-inner configuration (4877.65

N/mm). In all the configurations lower results were calculated when the two materials do not work together, and they were comparable with those registered by the un-reinforced specimens in the experimental test.
The stiffness data recorded during experimental tests are included among the values calculated in analytical studies, as showed in Figure 5.12. The only exception was observed in the lower configuration, where the experimental value is slightly higher than the analytical one when the steel and GFRP work together.

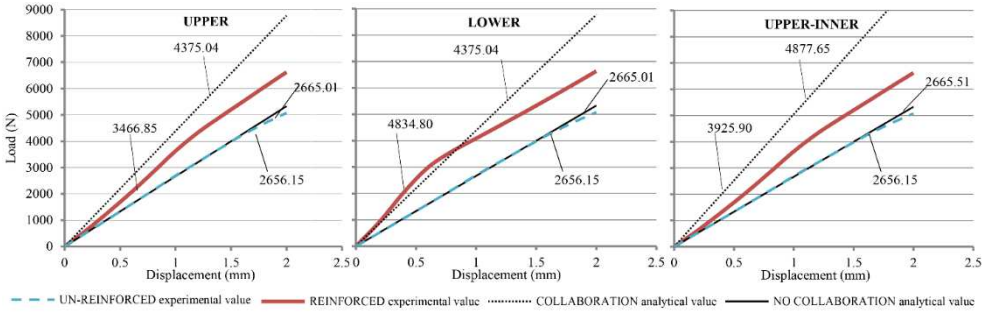

Figure 5.12. Comparison of experimental and analytical stiffness results of GFRP squared long specimens.

5.6 Discussion

The present study aims to evaluate both the GFRP-steel compatibility and the steel contribution to enhancing the mechanical performances of the GFRP profiles, also considering the effects of different environmental ageing conditions.

Regarding the mechanical performance in *un-aged* condition, the *bonding compatibility* between GFRP profiles and steel laminates was confirmed by the results obtained through *shear tests* on the single lap joints. The values were consistent with the data reported by manufacturers, confirming the highest performance of the first epoxy adhesive (EPX1). The *hybridization method*, consisting of GRFP squared tubular profiles adhesively joined to steel plates, resulted advantageously since it enhanced the *stiffness of* GFRP specimens subjected both to local and to flexural stresses.
The *puncture tests* revealed that the stiffness of the reinforced samples, with the steel laminates positioned in the three different configurations (upper, lower, upper-inner sides of the GFRP profiles), were higher than the un-reinforced ones, especially where a double reinforcement was applied. This result is consistent with other authors findings, which demonstrated the higher performance of hybrid specimens with respect to those without reinforcements [2, 3]. On the other hand, the load carrying capacity of the hybrid samples resulted lower than those of the un-reinforced GFRP profiles: during the load application, the steel plates penetrated inside the samples, indenting the composite's surfaces and weakening

the performance of the bonding systems. The only exception was showed by the first epoxy adhesives in the upper configuration, which resulted in the best performance of the tested adhesive.
The *three-point bending tests* demonstrated the best performance of the hybrid specimens in terms of both loads carrying capacity and stiffness, especially when the steel laminate was positioned in the lower configuration. In fact, the lower side of the GFRP profile was subjected to the tensile stresses and the steel reinforcement allowed higher containment of the deformations than in the other positions.
The *analytical stiffness results* of the GFRP-steel squared tubular long specimens were comparable with those observed in the experimental tests and confirmed the steel contribution to the enhancement of the GFRP mechanical response.
Regarding the effects of the two *ageing conditions*, the continuous condensation and UV exposures, similar results were observed in all the tested specimens: single lap joints and short tubular squared profiles. The *load* carrying capacity registered a decrease after the hot-wet exposure, while the UV exposure led to the opposite results. This is because, as stated in another study [8], during the UV ageing the specimens were inevitably heated by radiations, reaching surface temperature values of about 26 ˚C. This even small temperature increase could have determined a slight increase of the load carrying capacity, thanks to the cross-linking of the polymer network [17]. The *stiffness*, after both the environmental conditions, showed decreasing trends, especially after the continuous condensation treatment. In fact, some authors stated that adhesively bonded joints exposed to different temperatures and humidity levels registered high stiffness degradation, even without reaching the adhesive's glass transition temperature [9]. With regard to specimens exposed to the UV radiations, all the tested adhesives demonstrated a scarce UV resistance. This is because of the wavelength of UV radiation, in the range of 90–400 nm, usually cause polymers bond dissociation and the consequent decrease in adhesives elastic modulus [17, 22].
However, hybrid squared tubular specimens subjected to ageing treatments maintained higher stiffness in the elastic range than un-reinforced GFRP samples, especially after UV radiations, up to 36 % for the second epoxy adhesive. These results confirmed the advantageous method of hybridization, even when the bonding system is exposed to adverse environmental conditions.

Regarding the *combination* of the two *ageing conditions*, the effects on the single lap joints were better than the previous artificial treatments separately analysed. The best results were observed for the samples firstly subjected to UV radiations and later under high humidity and temperatures levels: both the *load* carrying capacity and the *stiffness* of the two adhesives registered increasing values respect to the un-aged ones. This could be explained by the effects of the UV radiations: as showed in the single ageing treatment, the UV exposure led to an increase of the load carrying capacity of the joints thanks to the cross-linking of the adhesives polymers. This previous effect resulted beneficially also after the exposition to the hot-wet exposure, which was the highest damaging conditions for the joints.
Regarding the second combination (when the sample were exposed to high humidity and temperatures levels and later underwent UV radiations), the first epoxy adhesive showed higher results with respect to the initial conditions, while the second one registered decreasing

data, although it maintained good performance thanks to the enhancement of its mechanical properties after the UV exposure. The aim of a future work is to deepen into the chemical compositions of the two epoxy adhesives, to analyse the effects of the combined artificial ageing.

5.7 Conclusions

In the present study, an experimental campaign on the bonding connection of GFRP pultruded profiles and steel laminates through three different epoxy adhesives is proposed. The contribution in terms of stiffness increase and deformations control by coupling steel laminates to GFRP pultruded profiles was analysed with the objective to verify the applicability of this hybrid system in structural members for curtain walls. Mechanical tests (shear, puncture and flexural) were performed on different specimens types and the effects of two environmental conditions, continuous condensation and UV radiations, were investigated.
The main outcomes are:

- Shear tests allowed demonstrating the compatibility of the GFRP-steel bonding system and the best mechanical performance of the first epoxy adhesive (EPX1) was observed, both in un-aged and aged conditions.
Between the two ageing treatments, the continuous condensation demonstrated higher negative effects on the joints, registering stiffness decreasing values up to 93 %. Instead, after the UV radiations, the load carrying capacity of the joints were increased thanks to a further polymerization of adhesives for slightly high (26 °C) temperatures.
The specimens were also subjected to the combinations of the continuous condensation and the UV radiations, in two different sequences: in the previous, the samples were firstly subjected to high humidity and temperatures levels and later under UV radiations (T_{cc}+T_{uv}); in the latter, the samples underwent UV radiations and then they were exposed to high humidity and temperatures levels (T_{uv}+T_{cc}). Both the ageing treatments showed better effects on the mechanical responses of the joints than those registered in the ageing conditions separately analysed, and the best results were obtained after the T_{uv}+T_{cc} exposure in terms of load carrying capacity and stiffness increases.

- Puncture tests permitted to simulate the local stress transmitted by the curtain panels bolted to the GFRP structural members, demonstrating that the stiffness of the GFRP reinforced profiles, with the steel laminates positioned in the three different configurations (upper, lower, upper-inner sides of the GFRP profiles), was higher than the un-reinforced ones. In the plastic range, instead, the un-reinforced GFRP profile showed better performance than the hybrid ones. This is because of the steel plates, indenting the GFRP surfaces, worsened the mechanical response of the composites profiles, in the long term.
EPX1 showed the best mechanical characteristics in un-aged condition, overall maintaining better performance than the other adhesives after the two artificial exposures.

The two ageing treatments demonstrated negative effects on the specimens, especially the continuous condensation one. However, hybrid squared tubular profiles subjected to ageing treatments maintained higher stiffness in the elastic range than un-reinforced GFRP.

- Flexural tests were performed to simulate the stress of the whole structural member that occurred in curtain walls (when it is subjected to the wind load), demonstrating that the best performance of the hybrid specimens in terms of both loads carrying capacity and stiffness, especially when the steel laminate was positioned in the lower configuration. In fact, the lower side of the GFRP profile was subjected to the tensile stresses and the steel reinforcement allowed higher containment of the deformations than in the other positions.
The analytical stiffness results of the GFRP-steel squared tubular long specimens were comparable with those observed in the experimental tests and confirmed the steel contribution to the enhancement of the GFRP mechanical response.

These results confirmed the reliability of the *Structural Member* for curtain walls basic principle, i.e. the hybrid system of GFRP pultruded profiles bonded with steel laminates. This result allows enhancing the GFRPs flexural performance and the containment of deformations, even maintaining small transversal areas.

5.8 References

[1] Wu C, Bai Y, Zhao X-L. Improved bearing capacities of pultruded glass fibre reinforced polymer square hollow sections strengthened by thin-walled steel or CFRP. *Thin-Walled Structures* 89 (2015) 67–75

[2] Haoa Q, Wangb Y, Oua J. Design recommendations for bond between GFRP/steel wire composite rebars and concrete. *Engineering Structures* 30 (2008) 3239-3246

[3] Kim H-Y, Lee S-Y. A steel-reinforced hybrid GFRP deck panel for temporary bridges. *Construction and Building Materials* 34 (2012) 192–200

[4] J. Qureshi, J. T. Mottramb. Behaviour of pultruded beam-to-column joints using steel web cleats. *Thin-Walled Structures* 73 (2013) 48–56

[5] Wu C, Bai Y. Web crippling behavior of pultruded glass fibre reinforced polymer sections. *Composite Structures* 108 (2014) 789–800

[6] Borowicz DT, Bank LC. Behavior of pultruded fiber-reinforced polymer beams subjected to concentrated loads in the plane of the web. *Journal of Composites for Constructions* 15(2) (2010) 229–38

[7] Turvey GJ, ZhangY. Characterisation of the rotational stiffness and strength of web–flange junctions of pultruded GRP WF-sections via web bending tests. *Composites Part A* 37(2) (2006) 152–64

[8] Stazi F, Giampaoli M., Rossi M, Munafo P. Environmental ageing on GFRP pultruded joints: Comparison between different adhesives. *Composite Structures* 133 (2015) 404–414

[9] Zhang Y, Vassilopoulos A. P, Keller T. Environmental effects on fatigue behavior of adhesively-bonded pultruded structural joints. *Composite Science and Technology* 69 (2009) 1022-1028

[10] Zhang Y, Vassilopoulos A. P, Keller T. Effect of low and high temperatures on tensile behavior of adhesively-bonded GFRP joints. *Composite Structures* 92 (2010) 1631-1639

[11] EN ISO 527-1:2012. Plastics -Determination of tensile properties – Part 1: General principles

[12] ISO 527-4:2012. Plastics -Determination of tensile properties – Part 4: Test conditions for isotropic and orthotropic fibre-reinforced plastic composites

[13] EN ISO 527-2:2012. Plastics -Determination of tensile properties – Part 2: Test conditions for moulding and extrusion plastics

[14] ASTM D 3418-03. Standard test method for Transition Temperatures of Polymers By Differential Scanning Calorimetry

[15] Elchalakani M. CFRP strengthening and rehabilitation of degraded steel welded RHS beams under combined bending and bearing. *Thin-Walled Structures* 77 (2014) 86–108

[16] ISO 6270-2:2005. Paints and varnishes — Determination of resistance to humidity — Part 2: Procedure for exposing test specimens in condensation-water atmospheres

[17] Nguyen T, Bai Y, Zhao X, Al-Mahaidi R. Effects of ultraviolet radiation and associated elevated temperature on mechanical performance of steel/CFRP double strap joints. *Composite Structures* 94 (2012) 3563–3573

[18] ASTM D904-99. Standard Practice for Exposure of Adhesive Specimens to Artificial Light

[19] ASTM D5573-99 Standard practice for classifying failure modes in fiber-reinforced-plastic (FRP) joints

[20] De Castro J. Experiments on double-lap joints with Epoxy, polyurethane and ADP adhesives. *Composite Construction Laboratory, Appendix B* – Technical Report n. CCLab2000.1 b/2

[21] Grassie N, Scott G. Polymer degradation and stabilization. Cambridge: *Cambridge University Press* (1988)

5.9 List of tables and figures

Chapter 6

On different types of glass coatings: physical, chemical, optical and energy performances before and after the ageing treatments

One of the main objective of the *Full Glass* window and of the *Structural Member* for curtain walls is the thermal transmittance reduction, approximating the double glass values. Therefore, the durability of the thermal performance of glass coatings is the subject of the present study. The contents of this chapter were published in a previous work: "*Durability of different glass coatings in humid and saline environments, ageing impact on heat-light transmission and thermal comfort"* [1].

6.1 Abstract

The present study investigates the durability of different types of glass coatings (four solar control, two low- emissivity and one self-cleaning) with various metal compositions. In the experimental phase, physical, chemical, optical and energy properties were evaluated, before and after two ageing treatments: hot-wet and salt-spray. In the numerical phase, the energy performance of a double glazing with the selected coatings was compared by adopting an office room as a case study. Heating, cooling, artificial lighting consumptions, solar gains, daylighting factors and summer comfort levels were analysed. Further, the environmental impact in the use phase was assessed. The salt-spray environment resulted in having the highest incidence on the film performance. In the physical and chemical tests, the worst resistance was shown by the coatings with the highest silver percentages, with the consequent significant decay of the light transmittance. The films with niobium and titanium showed the best durability. On the other hand, the silver-based coatings demonstrated the best solar selectivity and the highest performance in term of energy consumptions, comfort levels, and CO_2 emissions, both before and after ageing.

6.2 Introduction

In the buildings external envelope, glazing surfaces are the main responsible of the thermal exchanges between indoor and outdoor and, to achieve energy saving, they should satisfy contrasting requirements: optimize the solar gains in the winter season and prevent overheating in summer. On this respect, multifunctional coatings (such as low-emissivity, solar control, etc. [2-4]) are commonly applied on the windows and curtain walls glazing surfaces, to which this work is addressed.
Silver is one of the most used metal element in coatings, thanks to its electrical properties [5-7]. However, it is established in the literature that silver-based coatings are not so durable against moisture [8-14], which could cause degradation phenomena during transport and storage phases. Results on the durability of coatings made up of metals, other than silver, are very scarce in literature even if some authors stressed the importance of this topic [15].

The aim of the present study is the evaluation of the degradation phenomena occurring on different types of several coatings subjected to hot-wet and salt-spray environments. In the experimental phase, physical, chemical and optical decay were analysed. In the numerical phase, the samples were compared in terms of energy consumption, comfort levels, and environmental impact, also considering the effort of the performance decay.

Nomenclature			
Ag	Silver	$R_e(\lambda)$ [%]	Solar reflectance (double glass)
Al	Aluminum	$R_v(\lambda)$ [%]	Light reflectance (double glass)
BCLEAN	Self-cleaning coating	***Si***	Silicium
Ca	Calcium	***Sn***	Tin
Cl	Chloride	$T_e(\lambda)$ [%]	Solar transmittance (double glass)
CSOL1	First solar control coating	***Ti***	Titanium
CSOL2	Second solar control coating	$T_v(\lambda)$ [%]	Light transmittance (double glass)
CSOL3	Third solar control coating	***U*** [W/m²K]	Thermal transmittance (double glass)
CSOL4	Fourth solar control coating	***Zn***	Zinc
g [-]	Solar factor (double glass)	ε_n [-]	Normal emissivity (single glass) measured in the direction of the incident radiation
K	Potassium	ρ_e [%]	Solar reflectance (single glass) measured in the direction of the incident radiation [%]
LCA	LCA analysis	ρ'_e [%]	Solar reflectance (single glass) measured in the direction opposite to the incident radiation
LOWE1	First low emissivity coating	ρ_v [%]	Light reflectance (single glass) measured in the direction of the incident radiation
LOWE2	Second low emissivity coating	ρ'_v [%]	Light reflectance (single glass) measured in the direction opposite to the incident radiation
Mg	Magnesium	τ_e [%]	Solar transmittance (single glass)
Na	Sodium	τ_v [%]	Light transmittance (single glass)
Nb	Niobium	ϕ[W/m²K]	Linear thermal transmittance

6.3 Methodologies

6.3.1) Case studies

The function of glass coatings is the control of solar radiation, i.e. the spectral selectivity, by varying the amount of visual and thermal waves entering through the glass. The *solar control* and the *low-emissivity* coatings are two of the widely used types. The solar control one reduces the solar and infrared transmitted radiation, maintaining high transparency on the visible spectrum [16, 17]. This coating shows good reflectance properties in the range of $0.7<\lambda<50$ μm. The low-emissivity coating, instead, maintains high transmittance properties both in visible and solar range, while it is infrared radiations reflecting [13]. Another type is the *self-cleaning* coating, well known for its photocatalytic and hydrophilic performance. However, it is well established in the literature that it has also solar selectivity properties [18]: in fact, the titanium element, usually employed in this film, enhances the transmittance in the visible region and the reflectance in the infrared range [8].
In the present study, different types of double-glass coatings were investigated: four solar control with different compositions (CSOL1, CSOL2, CSOL3, and CSOL4), two low-emissivity (LOWE1 and LOWE2) and one self-cleaning (BCLEAN). The film positions are respectively 2, 3 and 1 (Fig. 6.1). The coated glasses were extracted from double-glass commercial specimens (Table 6.1).

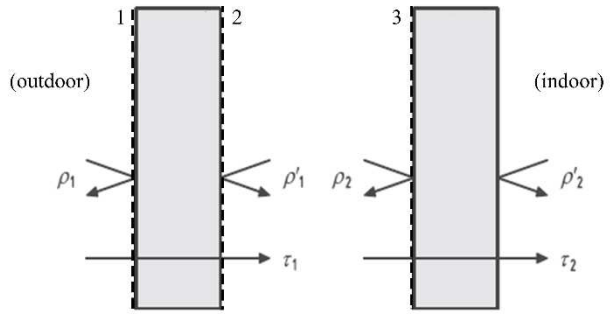

Figure 6.1. Different coatings positions (1=outdoor; 2=inside the cavity, in the outer glass pane; 3=inside the cavity, in the inner glass pane) and transmittance and reflectance in a double glazing insulating glass unit (EN 410)

Coatings are made up of multi-layered films of metal oxides, deposited by a magnetron sputtering method. The content in metal elements of different coated glasses was evaluated by energy dispersive X-ray analysis (EDXA) using a high-resolution scanning electron microscope ZEISS – SUPRA 40. Table 6.2 reports the content in metal elements as % by

weight, subdivided into elements belonging to the coatings and to the glass substrates. Note that the % by weight of each metal element was calculated with respect to the sum of the weights of only metal elements detected by EDXA. Most of the coatings (CSOL1, CSOL2, CSOL4, LOWE1, and LOWE2) presented both silver (Ag) and zinc (Zn) elements, in different percentage, to enhance both electrical and optical properties [5,7]. In CSOL4 the tin (Sn) addition improves the transmittance in the visible range and the reflectance in the infrared region, as stated by other authors [6,19]. Further, the two low-E coatings envisage the presence of titanium (Ti) which forms, instead, the only metal oxide of the self-cleaning film (BCLEAN). CSOL3 is the sole solar-control coating without Ag and Zn elements, including only the niobium (Nb) element. This metal is usually employed in electrochromic devices [20], showing different optic properties (colours) depending on the incident radiation.

Table 6.1. Features of the seven double glass specimens.

Double glass commercial samples	***Composition*** *(mm)*	***Gas***	***Film position***
CSOL1	6/12/6	air	2
CSOL2	6/12/6	air	2
CSOL3	6/12/6	air	2
CSOL4	6/12/6	air	2
LOWE1	6/12/4	air	3
LOWE2	6/12/6	air	3
BCLEAN	4/12/4	air	1

6.3.2) Phases

The research includes experimental and numerical studies, divided into the following phases:

- *Laboratory tests* to investigate the durability of the coatings. Physical, chemical, optical and energy properties were evaluated before and after two types of artificial ageing (hot-wet and salt-spray treatments), in order to compare the results and assess the performance decay respect to the initial conditions.

- N*umerical simulations* to analyse one double glass for each coating type. The energy consumptions, comfort levels, solar gains and daylighting parameters, before and after the two ageing treatments, were compared with the aid of Energy Plus software; the environmental impact for the use phase of each double glass coating was evaluated through SimaPro software.

6.3.2.1) Laboratory tests

Each sample (10x15 cm) was exposed to hot-wet and salt-spray aging for 21 days, according to UNI EN 1096-2 [21]. Firstly, the specimens were subjected to a hot-wet treatment in a thermostatic chamber (W86-KW Apparecchi Scientifici), with 90 % relative humidity at 40 °C. Other specimens were exposed to a saline solution at 40 °C in a salt-spray machine (DCTC 600 P ACS Environmental test chamber - Angelantoni Industrie). Both ageing chambers are transparent to natural light.
The tests were carried out to investigate the:

a) Physical deterioration. Identification of the white dots defects in analogy with [9,12], to evaluate the silver aggregation and the peeling of the metal layer after the two ageing treatments. The test consisted in counting the white spots larger than 0.2 mm. However, given that some stains tend to merge with the adjacent ones generating a single stain, the percentage of the degraded area was also evaluated. The region was analysed with a stereo microscope (Wild Makroskop M420) and an optical zoom 12.5X was employed to identify the most degraded areas. A raster graphics software (Autocad) was employed for the pixel count.

b) Change in chemical composition. Evaluation of the films chemical composition before and after the two ageing treatments to identify any chemical variation (Table 6.2). The tests were carried out through energy dispersive X-ray analysis (EDXA) using a high-resolution scanning electron microscope ZEISS – SUPRA 40.

c) Optical performance decay. Spectrophotometric tests were done on single glasses with all coating types to investigate the transmittance (τ) and reflectance properties (ρ, ρ'), in the visible (370 – 780 nm) and in the solar range (300 – 2500 nm), before and after the two ageing treatments. The tests were carried out using Jasco V-670 UV-VIS-NIR spectrophotometer.

d) Energy performance reduction. Spectrophotometric tests were done on single glasses to investigate the emissivity properties ε, in the medium and far infrared region (5000-50000 nm), before and after the hot-wet and the salt-spray treatments. The tests were carried out using PerkinElmer Spectrum GX FT-IR System.

6.3.2.2) Calculation of optical and energy parameters

The data processing on the optical and energy performance allowed calculating the light and solar transmittance, the light, and solar reflectance and the emissivity values on a small area of each coating. The latter was selected through the identification of the most degraded portion, using a scanning technique. The samples were scanned at a resolution of 600 dpi and an image processing program (Imagej) was used to convert the RGB images to greyscale images. An image editing software (Photoshop) was used for the pixel counting and the total

percentage of the degraded area was then evaluated (Fig. 6.2a and Table 6.3). Five specimens (CSOL3-HW, CSOL3-SAL, LOWE2-HW, BCLEAN-HW, BCLEAN-SAL) were characterized by a quite uniform degradation and the percentage of the degraded area was evaluated to be less than 50 % of the total sample surface (Fig. 6.2b). For such specimens, spectrophotometric tests were carried out in three different sections and the mean values were obtained.

Table 6.2. Chemical composition (metal content) of the coated glasses in un-aged condition, as detected by EDXA.

Samples	***Film composition [%]***			***Glass composition [%]***
	Ag	***Zn***	***Other***	
CSOL1	35.2 *81.1**	8.2 *18.9**	-	Si (37.7) – Na (8.6) – Ca(6.2) – Al (2.2) – Mg (1.9)
CSOL2	24.4 *61.7**	15.1 *38.3**	-	Si (39.1) – Na (7.6) – Ca (6.3) – Al (4.1) – Mg (3.4)
CSOL3	-	-	Nb (33.4) *100**	Si (52.6) – Ca(8.2) – Al (2.6) – Na (2.4) – Mg (0.8)
CSOL4	12.2 *23.4**	10.7 *20.5**	Sn (29.2) *56.1**	Si (24.5) – Na (8.1) – Ca (7.1) – Mg (4.6) – Al (3.6)
LOWE1	33.6 *64.8**	14.0 *27.1**	Ti (4.2) *8.1**	Si (34.2) – Na (6.7) – Ca (4.1) – Al (1.5) – Mg(1.1) – K(0.6)
LOWE2	25.1 *72.9**	7.6 *21.9**	Ti (1.8) *5.2**	Si (30.0) – Ca (15.0) – Na (13.5) – Mg (3.3) – Al (1.9) – K (1.8)
BCLEAN	-	-	Ti (1.8) *100**	Si (61.7) – Ca (15.6) – Na (14.1) – Mg (5.1) – Al (1.0) – K(0.7)

*The starred values represent the percentage of each metal element by considering only the coating layer materials (excluding glass)

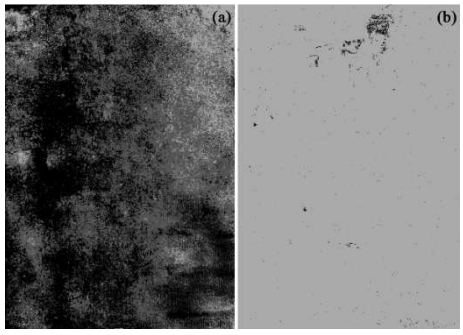

Figure 6.2. Grey-scale images of coated glasses after the ageing treatment: an almost uniform degraded sample (a) and a spotted degraded sample (b)

The following parameters were calculated:

1) *The light transmittance τ_v [%].* It is the fraction of the incident light that is transmitted by the glass. It was calculated according to Formula (1) and Table 1 of UNI EN 410:2011 [22]. The higher is the τ_v value the higher is the natural indoor illumination with a consequent reduction of electric lighting consumption.

2) *The solar transmittance τ_e [%].* It is the fraction of incident solar radiation that is directly transmitted by the glass. It was calculated according to Formula (10) and Table 2 of UNI EN 410:2011 [22]. This parameter affects the calculation of the total solar energy transmittance (g value), therefore, in Mediterranean climate, it is crucial to select windows with low τ_e in order to keep the solar heat gains as low as possible [23].

3) *The light reflectance ρ_v [%].* It is the fraction of the incident light that is reflected by the glass. It was calculated according to Formula (4) and Table 1 of UNI EN 410:2011 [22]. This parameter has the opposite behaviour of the light transmittance τ_v, so it should be beneficially reduced (see point 1).

4) *The solar reflectance ρ_e [%].* It is the fraction of the incident solar radiation that is reflected by the glass. It was calculated according to Formula (11) and Table 2 of UNI EN 410:2011 [22]. This parameter has the opposite behaviour of the solar transmittance τ_e, so it should be beneficially increased.

5) *The normal emissivity ε_n [-].* It is the ratio, in a direction normal to the surface, of the emissive power of the surface of the glass to the emissive power of a black body (a perfect emitter). It was calculated using Formulas (1-3) and Table A.2 of UNI EN 12898 [24]. The lower the ε_n, the higher the reflecting ability of the pane. This parameter should be beneficially reduced to reflect the room long wave infrared radiations back to the interior in winter and to avoid undesired absorption of the external heat gains into the glass pane in summer [25].

For each glazed insulating units, composed by two single glasses, an internal air gap and the film in the appropriate position, the main optical and energy parameters were also evaluated:

6) *The spectral transmittance and reflectance both in visible $T_v(\lambda)$ [%], $R_v(\lambda)$ [%] and in the solar range $T_e(\lambda)$ [%], $R_e(\lambda)$ [%].* They were obtained respectively from the spectral transmittance and reflectance of the individual glasses, using Formulas (2, 5) of UNI EN 410:2011 [22].

7) *The total solar energy transmittance g [-].* It is the fraction of the incident solar radiation that is totally transmitted by the double glass. It was calculated using Formula (7) of UNI EN 410:2011[22]. This parameter denotes the share of the incoming solar energy, which is

converted into heat inside the indoor space. The lower the g, the less transmitted solar heat and the greater the shading ability. A product with a high g rating is more effective at collecting solar heat during winter, while a product with a low g is more efficient at reducing cooling loads during summer by blocking heat gain from the sun. The optimal g value is determined depending on climate, orientation, and external shading.

8) *The thermal transmittance U [W/m²K]*. It is the parameter of the glazing that characterizes the heat transfer through the central part of the glazing (i.e. without edge effects), and it states the steady-state density of heat transfer rate per temperature difference between the environmental temperatures on each side. It was calculated using Formula (1) of UNI EN 673:2011 [26]. This parameter describes how much heat is transferred through the glazing per square meter and Kelvin temperature difference between inside and outside and it stands for the thermal loss of a glazing [27].

Table 6.3. Percentage of degraded area evaluated in the grey-scale images of the samples.

	CSOL1		***CSOL2***		***CSOL3***		***CSOL4***		***LOWE1***		***LOWE2***		***BCLEAN***	
	HW	***SAL***	***HW***	***SAL***	***HW***	***SAL***	***HW***	***SAL***	***HW***	***SAL***	***HW***	***SAL***	***HW***	***SAL***
Degradation [%]	58.3	84.8	55.3	76.3	0.7	25.6	61.1	64.6	57.8	72.2	46.2	69.6	1.13	25.17

6.3.2.3) Numerical simulations

Numerical simulations were carried out to investigate the *energy consumptions, comfort levels, solar gains* and *daylighting parameters* of each coating type, before and after the two ageing treatments.

Simulations were carried out in a dynamic regime with Energy Plus software by adopting a real case study: an office of the Engineering Faculty of Polytechnic University of Marche monitored in a previous experimental campaign [28]. The building is located in the city of Ancona (eastern coast in the centre of Italy, latitude: 43_N; longitude: 13_E) characterised by a hot-summer Mediterranean climate (Köppen climate classification) and by 1688 degrees days (D.P.R. n.412/93). The experimental activity has been focused on a south-west facing glazed surface. The size of the perimeter office is 6.35 m x 4.43 m. The external facade is characterised by strip windows subdivided into six operable sections by thermal cut aluminium frames (Fig. 6.3). Each isolated section has the following dimensions: 0.75 m x 1.95 m. The double glazing is a solar control glass with dimensions 4/9/4 mm.

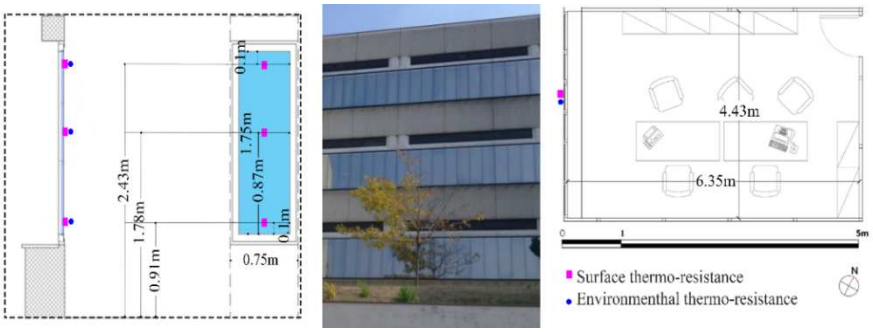

Figure 6.3. Plan of the monitored room: a vertical section with monitoring positions, view of the facade from the external side and plan of the internal room.

The glass and frame thermal, optical and geometrical characteristics are outlined in Table 6.4. The opaque vertical envelope consists of an insulated cavity wall 43 cm thick. The ratio between the glazed area and the total external wall area is about 57%.

Table 6.4. Window glazing and frame parameters

Glazing characteristics (UNI EN ISO 13363-1: 2008)	
U *[W/m²K]*	2.7
g	0.337
τv *[%]*	61.7
ρv *[%]*	15.7
τe *[%]*	31.3
ρe *[%]*	34.0
Frame characteristics (UNI EN ISO 10077: 2006)	
U *[W/m²K]*	2.82
Φ *[W/m²K]*	0.11

The virtual model reproducing the as built solution was realized and it was calibrated through comparison with measured values. A climatic input file containing the measured outdoor conditions was developed and the specific data regarding the real user's profiles for the room were set in the model, as detailed in Table 6.5a. So the correspondence between the monitored and calculated values could be checked. The obtained model reproduces quite well the observed values, as shown in Fig. 6.4.

The calibrated model was used to assess the energy consumptions, comfort-levels, solar gains and daylighting parameters associated with the adoption of different double glass coatings. To ensure that the study was not influenced by the specific use of the room, some input were

Table 6.5. Input values defining the real model (a) and the standard model (b), with respect to geometry, system set-up and efficiency.

Input values	*Real model (a)*	*Standard model (b)*	*Standards*
Ventilation rate	1.48 l/sm² *	0.8 l/sm²	UNI EN 15251:2008
Infiltration	0.7 vol/h	0.3 vol/h	UNI EN 15242:2008
Internal load from equipment	10 W/m²	6 W/m^2	UNI TS 11300-1:2008

subsequently fixed according to the relative standards (Table 6.5b). The simulations were carried out considering a density of 0.1 people/m^2 and the systems turned on during the working hours (08:00-18:00). The set point of the system was set at 20 °C for winter heating and 26 °C for summer cooling. The mechanical ventilation was set at 0.3 vol./h, according to UNI TS 11300-1:2008 [29]. Other input values are reported in Table 6.5b.

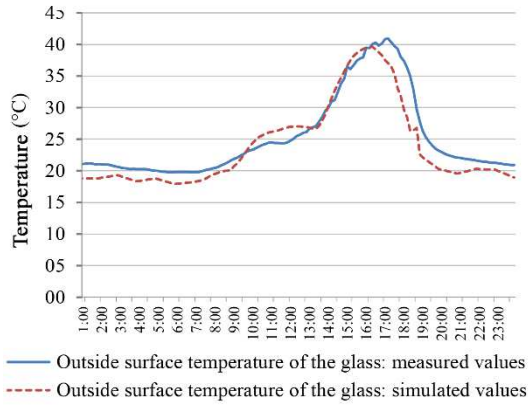

Figure 6.4. Calibration of the simulation model by comparison with the measured data

Parametric variations were subsequently made on the model by comparing different types of un-aged and aged coatings.

The optical and energy characteristics, used as input values, were derived from experimental tests and numerical calculation as explained in 6.3.2.1. For each double glazing type, heating, cooling and artificial lighting consumptions, solar gains, daylighting parameters and internal comfort levels were obtained.

The natural lighting was assessed and compared with the minimum value of 400 lux in the working environment according to UNI EN 12464-1:2011[30] and the additional electric energy necessary to guarantee proper illumination levels was calculated. Fluorescent lamps embedded in the ceiling were adopted with the power of 5 W/m^2 for 100 lux.

The comfort level was determined for the summer period with the adaptive model (UNI EN ISO 15251:2008 [31]), which defines, for the category III (existing buildings), the

upper and lower limit values for indoor operative temperature (T_i) depending on the running mean outdoor temperature (T_{rm}) according to the relation:

$$T_i \text{ max/min} = 0.33 * T_{rm} + 18.8 \pm 4 \qquad (1)$$

The method of "Percentage outside the range" was used (Method A, annex F, UNI EN ISO 15251:2008 [31]), calculating the number and the % of occupied hours in the summer season when the operative temperature is outside the comfort range.

The environmental impact of the use phase of the double glass coatings, before and after the ageing treatment, was evaluated. The Life Cycle Assessment (LCA) analysis was performed with the aid of software SimaPro according to ISO 14040:2006 [32] with the following steps:

1. Goal and scope definition: the *goal* was to compare the environmental impact of the adoption of different glazing systems. The *functional unit* was 1 m² (15 kg) of glass. As regard, the *system boundaries*, in this study the examined unit processes examined in this study were the use phase (heating, cooling and artificial lighting consumptions).

2. Life Cycle Inventory Analysis (LCI): the data for the construction were obtained mainly from Eco-Invent database. Yearly thermal, electric and artificial lighting consumptions were quantified from the dynamic analysis with Energy Plus software (see Table 6.10), assuming to be constant over 30-yr glass life span. The energy needs (Kwh) were calculated for a room with south-west exposure and referred to the functional unit through the multiplication by a factor obtained as the ratio of the functional unit surface (1 m^2) to the total surface of the external vertical wall adjacent to the selected room.

3. Life Cycle Impact Assessment (LCIA): the Global Warming Potential (IPCC 2001 GWP) was used and the results expressed in kg CO_2eq.

6.4 Results

6.4.1) Laboratory tests

6.4.1.1) Physical deterioration

Fig. 6.5 shows the optical microscope images of all samples during and after the durability tests in the humid and salt-spray environment.
After the hot-wet treatment, LOWE2 and CSOL1 showed the worst behaviour, with a percentage of white dots of about 20. LOWE2 showed a rapid deterioration, reaching an almost constant trend after the second day, while CSOL1 demonstrated the highest deterioration rate between the days 10th and 21st. LOWE1 showed a very similar trend with 18 % of white dots at the end of the ageing. The self-cleaning coating (BCLEAN) showed

the best performance until 10 days while, after the 21st day, CSOL3 showed the lowest deterioration (5 %). CSOL2 and CSOL4 obtained intermediate behaviours.
The salt-spray environment resulted in having the highest incidence on the film performance. CSOL2 demonstrated the highest degradation, with 66 % of white dots, followed by LOWE2, CSOL1, and LOWE1. For these samples, the deterioration began in different times of the ageing treatment, even if with very similar curve slopes. Again, the best behaviour was registered by BCLEAN, while CSOL3 and CSOL4 obtained very similar intermediate behaviours.
By an overall assessment, after both ageing treatments, the worst resistance was registered by the low-emissivity (LOWE2 and LOWE1) and the solar control films (CSOL 2 and CSOL1), all characterized by high silver percentages in the chemical compositions (Table 6.2). In fact, as highlighted by different authors [9-13], the moisture penetration produces a silver aggregation, causing the process of peeling and, gradually, the coatings detachment. The better durability of CSOL4 could be ascribed to the addition of a high percentage of tin (29.2 %) to the silver-zinc based coating. In fact, as stated by other authors [9], the use of the doping element in silver-based films results in lowering the film internal stress and, simultaneously, in improving the durability of the coatings. As expected, the best trend was shown by BCLEAN and CSOL3 samples, where only slight degradations were observed.

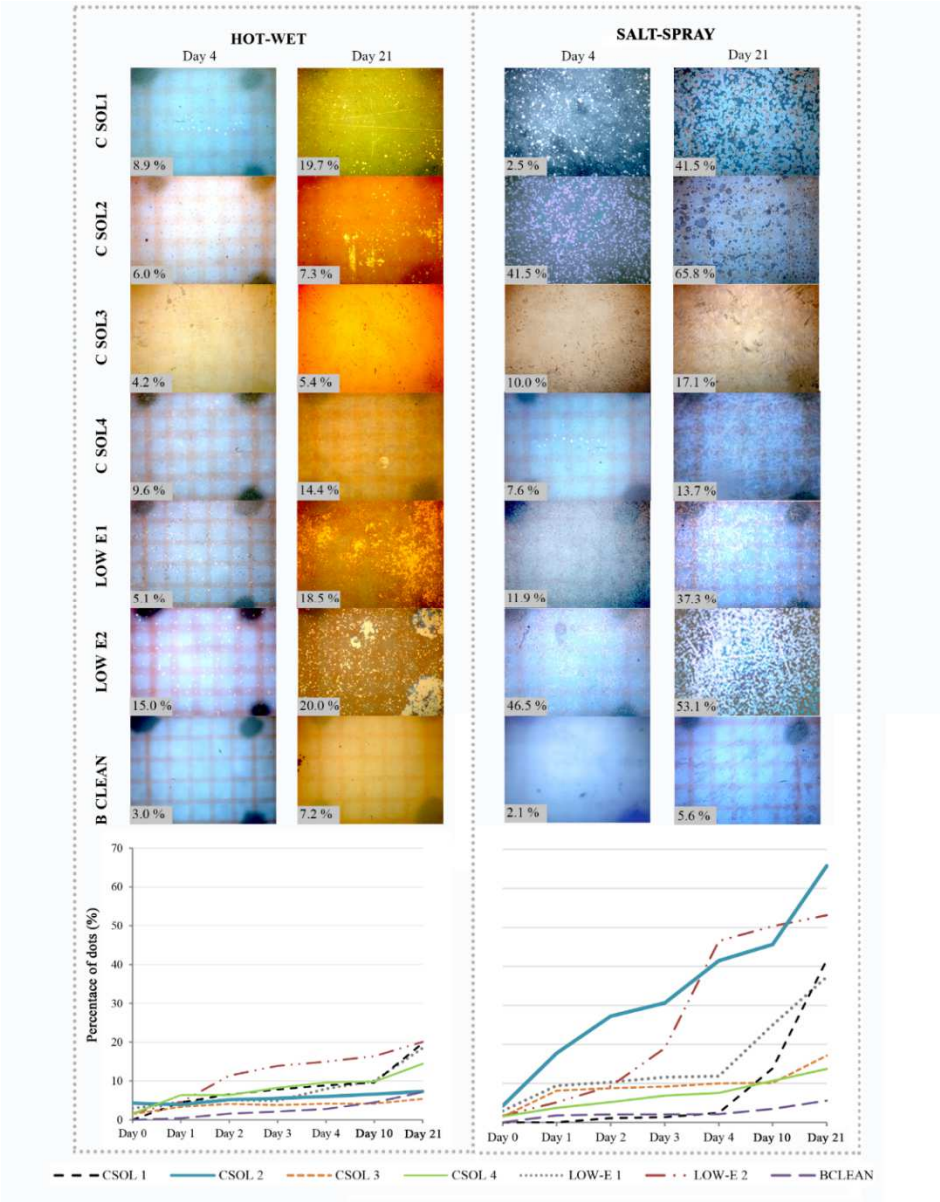

Figure 6.5. Optical microscope images of all samples during (day 4) and after (day 21) the durability tests in the humid and salt-spray environment. Evaluation of the deterioration trend of during the whole ageing treatment.

6.4.1.2) Chemical variation

Table 6.6 shows the variation in the metal elements content of coated glass after the most aggressive test, the salt-spray treatment. The data show a sensible reduction in silver content, of 26 % in the best case (LOWE1) and up to 63 % in the worst case (CSOL2). In the low-emissivity coating LOWE1, the addition of titanium contributed to reducing the silver oxide decay [12]. CSOL4 rerecorded a lower silver reduction than the other two solar control glasses thanks to the elevated tin percentage (56.1 %) in the film composition [9]. The zinc oxide, present within all the samples in combination with the Ag component, has very high percentages of decay. As highlighted by other authors [9-12], probably the moisture decreased the interfacial adhesion force between the top zinc oxide and silver layers. Ti element decayed of 6 % in the best case (BCLEAN) and of 28 % in the worst case (LOWE2). Niobium (Nb) element, the sole metal oxide in CSOL3, showed a decay of 16%. It is established in the literature [20,33] that niobium has excellent chemical stability in both acid and base media.

The results of chemical degradation for silver-based films almost correspond with the physical ones (*6.4.1.1*): the coatings with the highest chemical composition change (CSOL1, CSOL2, and LOWE2) had the worst behaviour in the white dots percentage evaluation too. Instead, LOWE1, which showed one of the worst performance in the previous physical test, unexpectedly revealed a better resistance than the previous coatings in the chemical test. This could be explained with the higher presence of Ti than the other low- emissivity coating, that could have reduced the Ag degradation (chemical aspect), without preventing its migration (physical aspect). This result confirms the positive effect of combining Ag with Ti, as stressed by other authors [34].

Table 6.6. The chemical composition of the coated glasses after the salt-spray treatment, as detected by EDXA.

Samples	***Film composition [%]***			***Glass composition [%]***
	Ag	***Zn***	***Other***	
CSOL1	15.6 *-56*	3.4 *-59*	-	Si (52.1) – Na (12.7) – Ca(10.9) – Mg(3.1) – Al(2.2)
CSOL2	8.9 *-63*	3.4 *-77*	-	Si (56.2) – Ca(13.9) – Na(12.5) – Mg(3.1) – Al(2.0)
CSOL3	-	-	Nb (28.2) *-16*	Si(40.7) – Ca(12.8) – Na(12.5) – Mg(4.2) – Al(1.6)
CSOL4	6.4 *-48*	1.5 *-86*	Sn (24.9) *-15*	Si(42.0) – Ca(12.6) – Na(9.2) – Mg(2.6) – Al(0.8)
LOWE1	24.7 *-26*	10.1 *-28*	Ti (3.1) *-26*	Si(44.9) – Na(6.6) – Ca(5.7) – Al(2.5) – Mg(1.4) – K(1.0)
LOWE2	12.0 *-52*	2.6 *-66*	Ti (1.3) *-28*	Si(37.1) – Na(16.9) – Ca(12.5) – Mg(6.5) – Al(5.7) – K(5.4)
BCLEAN	-	-	Ti (1.7) *-6*	Si(60.1) – Ca(15.9) – Na(15.4) – Mg(4.9) – Al(1.0) – K(1.0)

Values in cursive format represent the percentage reductions with respect to un-aged condition

Similarly, in the two tests, CSOL4 had intermediate results and CSOL3 and BCLEAN had the best performance.

Since after the aging treatments the surface of the samples appeared to be not uniform, a linear scanning by EDXA allowed the detection of the change in the chemical composition of coatings through areas with different colour and morphology. Fig. 6.6 reports the results obtained for CSOL2 and CSOL4 representative of a uniform degraded type and of a spotted degraded type, respectively. The latter presents dark spots where drops of silver (Ag) and tin (Sn) content with the simultaneous growth of the glass substrate chemical elements (silicon (Si) and sodium (Na)) can be observed. Then, in the clear filamentous stains, the peak in the silver content corresponds to an abrupt decrease in the silicon one (Si). This behaviour is typical of an Ag-based coating, in which high moisture concentrations determined a migration from dark areas (in which the elements of underlying glass are highlighted) to white lines or areas (in which the Ag elements are accumulated). For both samples, the zinc spectra were deleted in the graph because of its very reduced amount in the film composition.

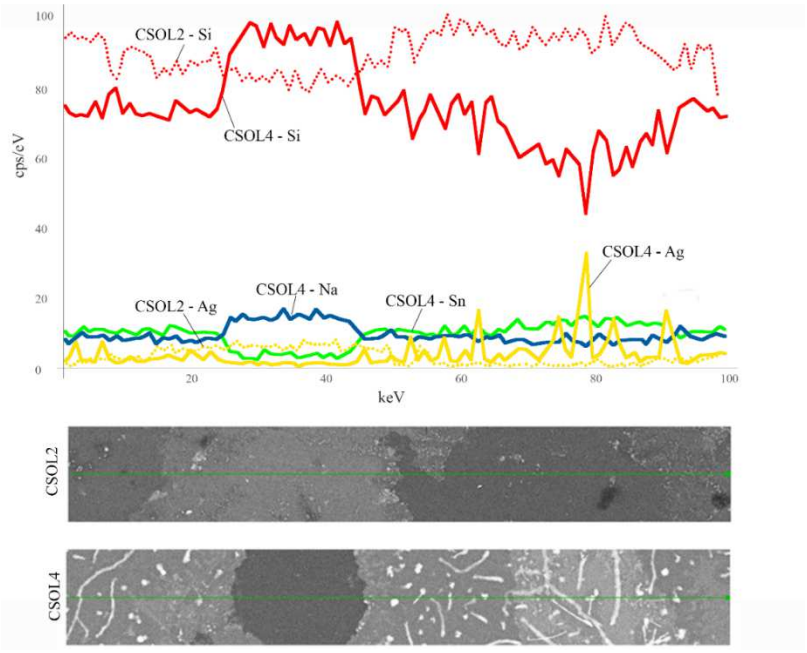

Figure 6.6. Detection of the change in the chemical composition of coatings through areas with different color and morphology by EDXA linear scanning. CSOL2 and CSOL4 are representatives of a uniformly degraded type and of a spotted degraded type, respectively.

6.4.1.3) Optical and energy performance decay

The analyses of optical (transmittance and reflectance) and energy performances (emissivity, total solar energy transmittance and thermal transmittance) were carried out separately for the three coatings typologies (solar control, low-emissivity and self-cleaning) and, in each section, the properties of the samples were compared before and after the two ageing treatments. The transmittance (τ) and reflectance properties (ρ, ρ'), both in the visible and solar region and the emissivity values (ε) are summarized in Tables 6.7, 6.8 and 6.9 for the solar control, low-emissivity and self-cleaning coatings, respectively. The tables also report the calculation of the solar factor (g) and the thermal transmittance (U) for the relative double glass configurations (the latter combining the coated glass with an un-coated one). In aged conditions, the values are highlighted in the tables with a grey hatch.

Solar control coatings

The transmittance and reflectance trend for the four solar control coatings, both in un-aged and aged conditions, are plotted in Fig. 6.7.

In un-aged conditions (Fig. 6.7a), in the visible region (300÷800 nm), CSOL4 revealed the best properties, with the highest value of light transmittance and the lowest reflectance, thanks to the tin addition to the silver based coating. Instead, in the near infrared and in the first part of the medium-infrared (800÷2500 nm), instead, for almost all the coatings the transmittance values were strongly reduced to avoid undesired heat gains and winter heat losses. The best performance was registered by CSOL1, the coating with the highest silver percentage in the film composition and a very similar behaviour was shown by CSOL2. A very different behaviour was shown by CSOL3, which, because of its brown-gray colouring, demonstrated the lowest visible transmittances and the highest trend for high wavelengths. The reflectance, as expected, had inverse behaviours. The same conclusion could be drawn by the study of optical parameters reported in Table 6.7. The sole difference in the film classification could be stressed trough τ_e parameter, that presents a mediated formula between 300 and 2500 nm, including both the visible and the infrared ranges. In this case, CSOL3 showed the lowest solar value instead of the highest one in the infra-red range (as seen in the graph). Regarding the energy performance (between 5000 and 25000 nm), the elaboration of ε value shows that CSOL1 has the best behaviour with the lowest value of 0.013. Very low g and U values were obtained for this coating in the relative double glass configuration. The niobium-based coating CSOL3 is the sole solar control type without Ag metal element and showed the highest emissivity value among all the samples.

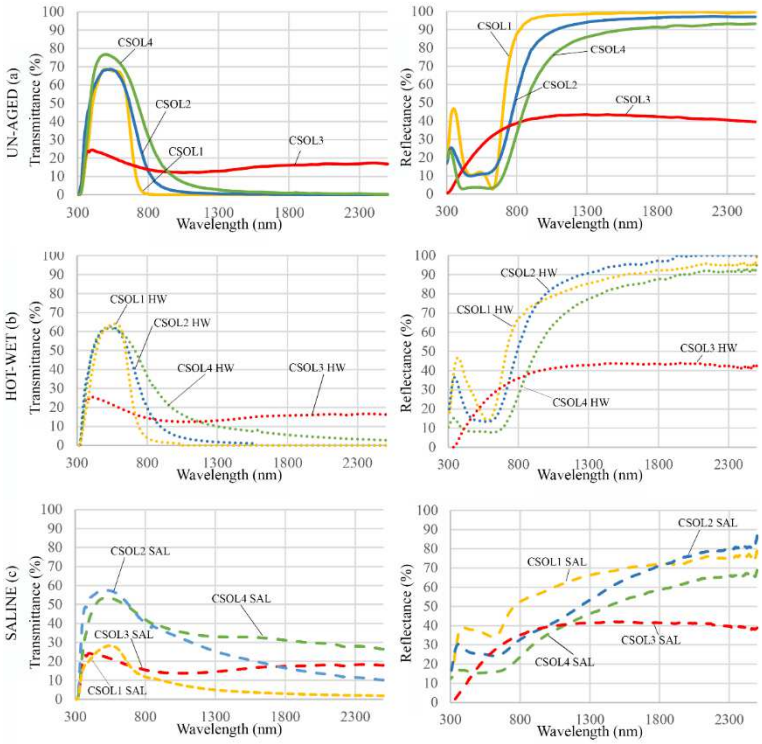

Figure 6.7. Transmittance and reflectance trends for the four solar control coatings, both in un-aged (a) and aged conditions (hot-wet (b) and saline (c) exposures).

With regard to the ageing treatments (Fig. 6.7b,c), the highest decays of coatings performances were registered after the saline exposure. The films with the highest transmittance and reflectance variations, in both visible and solar range, were those with the silver substrate (CSOL1, CSOL2, and CSOL4). In the visible region, CSOL1 showed the worst behaviour with the highest variation of transmittance and reflectance properties. The best durability was identified in CSOL3, for which slight gains of light transmittance values were registered, probably because of the brown coating physical deterioration. In the infrared region (800÷2500 nm), CSOL4 showed the worst resistance in transmittance value, while CSOL3 registered the best durability. The calculation of optical parameters (Table 6.7) confirmed the previous findings with some exceptions, due to the mediated formulas on the entire solar spectrum range (as mentioned above). In particular, in the visible range, the great decrement recorded by CSOL1 strongly contributed to reducing of the global τ_e, which became the lowest.

Regarding the energy performance (between 5000 and 25000 nm), the elaboration of ε value shows that even after ageing CSOL3 had again a very high durability, showing a reduction rather than an increment in emissivity and thermal transmittance properties. On the contrary, CSOL1 revealed the worst resistance, with a very high increment of emissivity value (about 1900 %).

From an overall evaluation, before the ageing treatment, the best behaviour could be assigned to CSOL1 (thanks to high Ag concentration), while the worst one to CSOL3 (without Ag). Inversely, this latter sample registered the highest conservation of optical and energy properties after both aging treatments, confirming the good chemical stability and corrosion resistance of the niobium element. The worst resistance, instead, was shown by CSOL1. However, the latter coating resulted in having the highest performance among the other coatings, even after ageing, for its very high un-aged performance.

Table 6.7. Experimental optical and energy properties of solar control type

	τv %	**T_v** %	**ρ_v** %	**ρ'_v** %	**R_v** %	**τe** %	**T_e** %	**ρ_e** %	**ρ'_e** %	**R_e** %	**ε** -	**g** -	**U** W/m²K
CSOL1	70.3	**64.9**	17.8	18.2	**22.6**	28.6	**26.7**	53.0	37.7	**38.4**	0.013	**0.29**	**1.58**
HW	62.2	**57.4**	17.8	18.0	**21.4**	26.7	**24.8**	51.0	38.7	**39.3**	0.058	**0.28**	**1.69**
%	-12		/	-1		-7		-4	+3		+346	-3	+7
SAL	27.3	**25.5**	30.7	31.7	**32.4**	16.2	**15.0**	47.8	34.3	**34.5**	0.263	**0.20**	**2.11**
%	-61		+72	+74		-43		-10	-9		+1923	-31	+34
CSOL2	70.1	**64.8**	18.9	20.2	**24.5**	33.7	**31.2**	44.0	30.0	**31.0**	0.037	**0.34**	**1.64**
HW	61.2	**57.2**	13.8	14.5	**17.9**	32.6	**30.2**	44.7	32.0	**32.9**	0.041	**0.33**	**1.65**
%	-13		-27	-28		-3		+2	+7		+11	-3	+1
SAL	56.6	**52.6**	24.9	21.9	**24.7**	43.0	**39.4**	35.0	28.0	**29.6**	0.272	**0.43**	**2.13**
%	-19		+31	+8		+28		-20	-7		+365	+26	+30
CSOL3	20.0	**18.6**	26.9	31.6	**32.0**	16.4	**15.0**	34.3	25.7	**25.9**	0.647	**0.22**	**2.65**
HW	21.4	**19.8**	20.6	27.4	**27.8**	17.9	**16.3**	26.4	23.8	**24.1**	0.601	**0.23**	**2.59**
%	+7		-23	-13		+8		-23	-7		-7	+5	-2
SAL	22.0	**20.4**	24.3	30.6	**31.0**	18.7	**17.0**	27.3	26.4	**26.7**	0.622	**0.23**	**2.62**
%	+7		-10	-3		+11		-20	+2		-4	+5	-1
CSOL4	77.2	**70.9**	11.8	13.1	**18.3**	41.9	**38.4**	32.6	22.4	**23.9**	0.080	**0.42**	**1.74**
HW	60.9	**55.7**	8.0	8.6	**11.8**	38.8	**35.5**	31.0	23.6	**24.9**	0.097	**0.39**	**1.78**
%	-21		-32	-34		-7		-5	+5		+21	-7	+2
SAL	52.8	**48.7**	15.6	15.5	**18.0**	42.8	**39.0**	26.1	21.5	**23.1**	0.328	**0.43**	**2.22**
%	-31		+32	+18		+2		-20	-4		+310	+2	+28

Values in cursive format represent the percentage variations with respect to un-aged conditions

Low-emissivity coatings

The transmittance and reflectance trend in the range of 300÷2500 nm of the two low-emissivity coatings, both in un-aged and aged conditions, are plotted in Fig. 6.8.

In un-aged conditions (Fig. 6.8a), in the visible region (300÷800 nm), the best properties were shown by LOWE2, with the highest transmittance and inversely the lowest reflectance. On the contrary, LOWE1 recorded the best performance in the infrared range (800÷2500 nm), for its high reflecting attitude thanks to the elevated percentages of Ag and Ti elements. Moreover, the study of energy performances (Table 6.8) showed that this coating has the lowest values for all the significant parameters: emissivity (ε), total solar energy transmittance (g) and thermal transmittance (U).

After the ageing treatments (Fig. 6.8b), in all the spectrum range (300÷2500 nm) LOWE2 showed the highest decays, both in transmittance and reflectance values, especially after the exposition to the saline environment. The calculations (Table 6.8) only partially confirmed these results, for the above-mentioned reasons (mediated formula). In particular, LOWE1 showed the worst behaviour in solar transmittance τ_e and reflectance ρ_e values after the hot-wet treatment.

Regarding the energy performance (between 5000 and 25000 nm), the elaboration of ε value (Table 6.8) shows that LOWE1-HW recorded the highest increments.

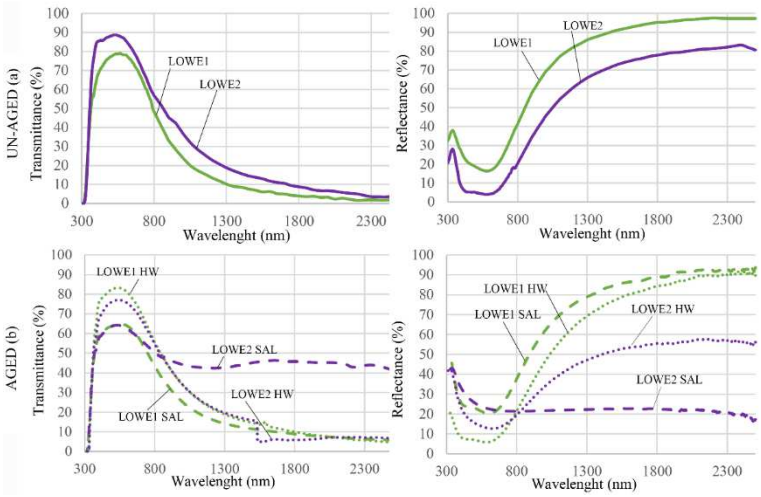

Figure 6.8. Transmittance and reflectance trends for the low-emissivity coatings, both in un-aged (a) and aged conditions (b)

To summarize, the best un-aged behaviour was recorded by LOWE1 for the high silver percentage in the film composition that, on the other hand, determined its worst durability. However the best solution still remains LOWE1 since, having very high un-aged performances, it recorded the best performance even after ageing.

Table 6.8. Experimental optical and energy properties of low emissivity type

	τ_v %	T_v %	ρ_v %	ρ'_v %	R_v %	τ_e %	T_e %	ρ_e %	ρ'_e %	R_e %	ε -	g -	U W/m²K
LOWE1	80.7	**74.5**	17.7	17.4	**23.6**	50.4	**46.5**	42.5	34.7	**43.3**	0.033	**0.51**	**1.33**
HW	82.2	**75.1**	6.3	7.7	**13.9**	56.4	**51.4**	27.0	20.0	**30.2**	0.180	**0.61**	**1.65**
%	*+2*		*-64*	*-55*		*+12*		*-36*	*-42*		*+445*	*+20*	*+24*
SAL	64.0	**59.3**	21.4	23.5	**26.7**	44.2	**40.8**	41.5	35.0	**42.4**	0.094	**0.49**	**1.47**
%	*-21*		*+20*	*+35*		*-12*		*-2*	*+1*		*+185*	*-4*	*+11*
LOWE2	89.3	**81.8**	8.8	10.0	**16.0**	59.8	**54.4**	25.4	18.4	**28.9**	0.206	**0.63**	**1.71**
HW	75.9	**69.7**	12.0	13.6	**18.7**	52.4	**47.8**	27.1	20.6	**30.3**	0.451	**0.60**	**2.18**
%	*-15*		*+36*	*+36*		*-12*		*+7*	*+12*		*+116*	*-5*	*+27*
SAL	63.3	**58.8**	23.8	18.7	**28.8**	53.1	**48.3**	24.3	16.9	**28.0**	0.753	**0.62**	**2.70**
%	*-30*		*+170*	*+87*		*-11*		*-4*	*-8*		*+265*	*-2*	*+58*

Values in cursive format represent the percentage variations with respect to un-aged conditions

Self-cleaning coating

The transmittance and reflectance trend in the range of 300 ÷ 2500 nm of the self-cleaning coating, both in un-aged and aged conditions, are plotted in Fig. 6.9.

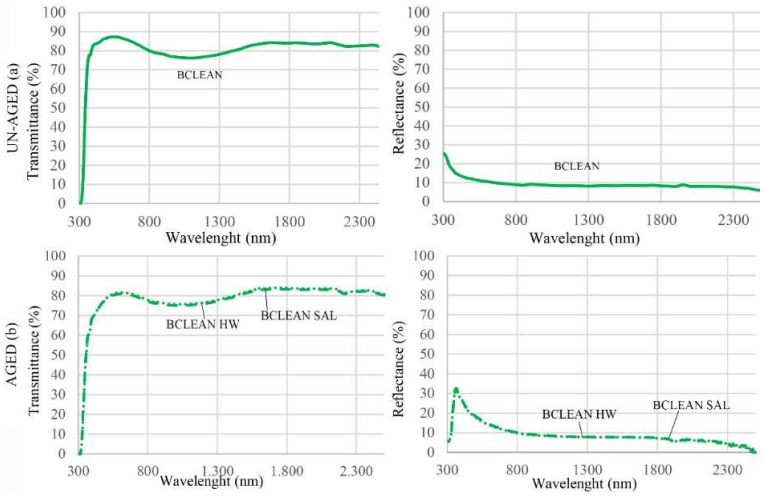

Figure 6.9. Transmittance and reflectance trends for the self-cleaning coating, both in un-aged (a) and aged conditions (b)

In un-aged condition (Fig. 6.9a), this coating type revealed very high both visual and solar transmittance values, allowing the entrance of both light and heat. On the other hand, it

demonstrated low reflectance properties. The energy values (Table 6.9), namely ε, g and U, were the highest among all the tested coatings.

After the two ageing treatments (Fig. 6.9b), the transmittance properties were not affected, confirming the results of the physical and chemical tests, which identified this coating as the most durable among all the tested samples. On the other hand, the reflectance values demonstrated increasing trends, both in visible and solar range. This could be explained by the photocatalytic effect occurred in the titanium nanoparticles (activated by natural radiation in the ageing chambers), that enhanced the film solar reflectance properties.

Table 6.9. Experimental optical and energy properties of self-cleaning type

	τ_v	T_v	ρ_v	ρ'_v	R_v	τ_e	T_e	ρ_e	ρ'_e	R_e	ε	g	U
	%	%	%	%	%	%	%	%	%	%	-	-	W/m²K
BCLEAN	86.9	**79.7**	11.1	10.9	**17.7**	81.8	**73.5**	9.9	9.6	**14.6**	0.837	**0.76**	**2.83**
HW	77.5	**71.4**	16.1	16.0	**21.4**	75.6	**68.2**	14.2	14.9	**19.0**	0.837	**0.71**	**2.83**
%	*-7*		*+41*	*+47*		*-7*		*+43*	*+51*		*0*	*-7*	*0*
SAL	80.2	**74.0**	16.1	16.5	**21.8**	76.0	**68.5**	15.1	13.6	**19.9**	0.837	**0.71**	**2.83**
%	*-8*		*+47*	*+52*		*-7*		*+37*	*+55*		*0*	*-7*	*0*

Values in cursive format represent the percentage variations with respect to un-aged conditions

6.4.2) Numerical results

Tables 6.10 shows the heating, cooling and artificial lighting consumptions, solar gains, daylighting factors and internal thermal comfort levels for the various double-glass coatings, before and after the two ageing treatments. Furthermore, the environmental impacts due to the use phase, evaluated through the LCA analysis, are summarized in the same table.

Table 6.10. Energy saving and comfort in an office room

	Heating consumptions	***Cooling consumptions***	***Artificial lighting consumptions***	***Solar gains***	***Daylighting factor***	***Discomfort Overheating***	***LCA***
	kWh/m²yr	*kWh/m²yr*	*kWh/m²yr*	*kWh/m²yr*	*%*	*hours/season*	*kg CO_2eq*
CSOL1	*37.2*	*32.5*	*2.8*	*34.2*	*3.2*	*1429*	*3342.1*
HW	*38.4*	*31.3*	*3.1*	*31.9*	*2.7*	*1123*	*3310.8*
%	*+3*	*-4*	*+7*	*-7*	*-16*	*+21*	*-1*
SAL	*42.1*	*27.8*	*5.4*	*19.2*	*1.1*	*221*	*3321.0*
%	*+13*	*-15*	*+88*	*-44*	*+66*	*-85*	*-1*
CSOL2	*36.3*	*36.3*	*2.9*	*39.8*	*3.2*	*1854*	*3583.9*
HW	*36.5*	*35.4*	*3.1*	*38.6*	*2.7*	*1743*	*3541.5*
%	*+1*	*-2*	*+8*	*-3*	*-16*	*-6*	*-1*
SAL	*37.8*	*41.6*	*3.2*	*50.3*	*2.6*	*2098*	*4000.2*
%	*+4*	*+15*	*+13*	*+26*	*-19*	*+13*	*+12*
CSOL3	*44.0*	*30.9*	*6.5*	*19.2*	*0.8*	*400*	*3652.5*

HW	*43.4*	*31.6*	*6.3*	*20.7*	*0.8*	*523*	*3671.4*
%	*-1*	*+2*	*-3*	*+8*	*0*	*+31*	*+1*
SAL	*43.6*	*31.5*	*6.2*	*21.6*	*0.9*	*506*	*3662.9*
%	*-1*	*+2*	*-5*	*+13*	*+13*	*+27*	*0*
CSOL4	*35.3*	*41.7*	*2.7*	*48.8*	*3.5*	*2228*	*3911.3*
HW	*35.9*	*39.8*	*3.1*	*45.1*	*2.7*	*2213*	*3824.6*
%	*+2*	*-5*	*+14*	*-8*	*-23*	*-1*	*-2*
SAL	*38.0*	*42.4*	*3.4*	*49.5*	*2.3*	*2113*	*4072.9*
%	*+8*	*+2*	*+23*	*+1*	*-34*	*-5*	*+4*
LOWE1	*32.4*	*49.1*	*2.7*	*59.5*	*3,8*	*2530*	*4340.7*
HW	*32.6*	*56.9*	*2.7*	*65.3*	*3,9*	*2593*	*4873.9*
%	*+1*	*+16*	*0*	*+10*	*+3*	*+3*	*+12*
SAL	*33.4*	*48.4*	*3.0*	*52.1*	*2,9*	*2462*	*4338.4*
%	*+3*	*-2*	*+12*	*-12*	*-24*	*-3*	*0*
LOWE2	*32.7*	*58.0*	*2.6*	*69.1*	*4,2*	*2599*	*4944.0*
HW	*36.2*	*53.9*	*2.8*	*60.6*	*3,5*	*2481*	*4766.6*
%	*+11*	*-7*	*+7*	*-12*	*-17*	*-5*	*-4*
SAL	*38.1*	*53.6*	*3.0*	*61.2*	*2,9*	*2434*	*4806.7*
%	*+16*	*-8*	*+16*	*-11*	*-31*	*-6*	*-3*
BCLEAN	*36.5*	*62.9*	*2.6*	*96.0*	*3.9*	*2591*	*5369.8*
HW	*37.1*	*59.8*	*2.7*	*90.3*	*4.1*	*2562*	*5181.5*
%	*+2*	*-5*	*+4*	*-6*	*+5*	*-1*	*-4*
SAL	*37.3*	*59.3*	*2.7*	*89.5*	*4.0*	*2550*	*5152.6*
%	*+2*	*-6*	*+4*	*-7*	*+3*	*-2*	*-4*

Values in cursive format represent the percentage variations with respect to un-aged conditions

Solar control coatings

Among un-aged samples, CSOL4 obtained the lowest heating consumptions (thanks to its low thermal (U) and high solar (g) transmittances), while CSOL3 had the highest value of energy usage. Intermediate values were shown by the other solutions. An opposite trend was observed in the summer period: the best behaviour was demonstrated by CSOL3 (thanks to its low solar (g) and high thermal (U) transmittances), with the lowest cooling consumptions, while CSOL4 showed the highest energy usage. By an overall winter and summer evaluation, the combination of both minimum values for g and U configures the best solution, which is CSOL1.

As expected, the study of the artificial lighting consumptions showed that the lowest value was reported by CSOL4 for its high light transmission τ_v, while very high energy use for lighting was recorded by CSOL3, characterized by a brown-gray colouring (very low τ_v). Furthermore, the latter coating showed a daylighting factor lower than the threshold value of 2%, as fixed by UNI EN 15193.

The analysis of the adaptive comfort in the summer period showed that the solar control CSOL3 is the best type of coating among all the tested samples. Very higher discomfort levels, due to overheating, were demonstrated by CSOL4.

With regard to the ageing treatments, the highest variations were registered after the saline exposure with one of the worst behaviours obtained by CSOL1. In fact, this sample

showed the highest increments of heating energy and artificial lighting consumptions, with a decrease of the daylighting factor down to 1.1 %. On the other hand, in the summer period, this coating revealed an opposite trend: in fact, after the saline exposure, it showed a high decrement of the solar transmittance property and the solar gains resulted in being very reduced. Therefore, a consistent improvement of the comfort level was registered. After the exposure period, CSOL3 confirmed its best behaviour, with almost unvaried values respect to un-aged ones.
The study with IPCC 2001 GWP method during 30-yr life span demonstrated that CSOL4 causes the highest carbon dioxide emissions among all the un-aged solar control coatings while the lowest CO_2 concentration in the atmosphere was shown by CSOL1. This is also confirmed in aged conditions, especially after the saline treatment, with even lower emissions values. Fig. 6.10 shows the different contributes to cooling, heating, and artificial lighting consumptions to the total amount of CO_2 emissions for CSOL1 and CSOL1-SAL. The greatest share is due to cooling energy for the low efficiency of the electrical power. By comparing the two samples, CSOL1 demonstrated the lowest heating and artificial lighting consumptions but, on the other hand, the highest cooling energy usage.

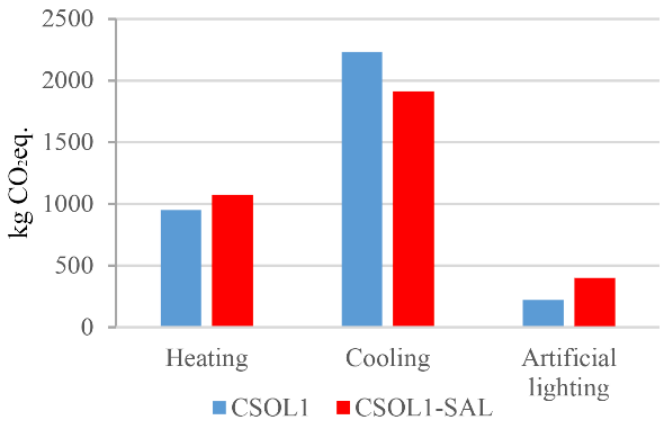

Figure 6.10. Different contributes of cooling, heating and artificial lighting consumptions to the total amount of CO_2 emissions for CSOL1 and CSOL1-SAL

To summarize, the technologies have almost similar values regarding winter consumptions, while they have more variable energy usages for summer consumptions. Globally, the worst solution is that with the highest energy cooling energy demand (and consequent summer discomfort and high environmental impact), namely CSOL4. On the contrary, CSOL1 is the best one minimizing the cooling consumptions and consequently environmental burdens.

Low-emissivity coatings

These coatings showed different performance with respect to the solar control ones, namely higher consumptions in the summer period and lower heating energy needs.

In un-aged conditions, very similar values of heating consumptions were shown by the two samples, while different trends were observed in the summer period: the best behaviour was demonstrated by LOWE1, with the lowest cooling energy usage. As expected, the analysis of the adaptive comfort in the summer period showed that the latter is the best solution, even if it demonstrated a very high discomfort for overheating. In the study of the artificial lighting values, instead, LOWE2 demonstrated the best behaviour thanks to its very high light transmission value.

After the ageing treatments, LOWE1 showed the lowest increments in heating and artificial lighting consumptions, while the other low-emissivity coating (LOWE2) demonstrated decreasing value of cooling energy for both environmental ageing. The analysis of CO_2 emissions revealed that LOWE1 is the best solution.
In summary, LOWE1, characterized by the highest silver percentage in the film composition, is the preferable solution.

Self-cleaning coating

This coating type showed the worst energy and environmental performance among all the tested coatings, because of the very high cooling consumptions registered in the summer period. With regard to heating and artificial lighting energy, very similar values to the solar control and the low-emissivity coatings were observed. After the two ageing treatments, BCLEAN is the sample that showed the lowest variations among all the coatings.

6.5 Discussion

The present section regards the integrated evaluation of the results, by comparing the glass coatings before ageing (i), identifying the effects of the artificial treatments on films components (ii) and the consequent decay of their properties (iii).

(i) Regarding the *comparison between glass coatings before ageing*, the analysis of optical and energy values demonstrates that the coatings with high silver percentage have the highest initial performance, concerning energy consumptions, comfort levels, and CO_2 emissions. The silver-based coatings, in fact, are widely used for insulating glass units, because of their high performance on thermal insulations [9-13].
Among the solar control coatings, the three silver-based showed comparable optical and energy performances to those founded in literature (Fig.6.11): high transmission in the visible spectrum and reduced infrared transmitted radiation [2].

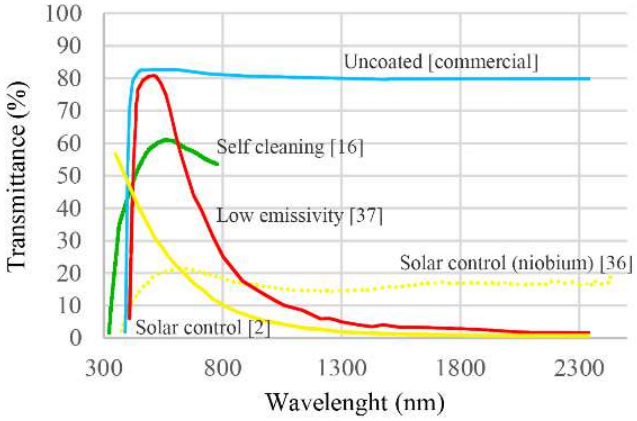

Figure 6.11. Transmittance properties of typical glass coatings founded in literature (solar control type: silver-based [2] and niobium-based [36]; low-emissivity type: silver-based [37]; self-cleaning type: titanium-based [16]) compared with an uncoated one [commercial]

The niobium-based sample, instead, was the sole coating with different optical properties, i.e. very low visible transmittances and higher values for infrared wavelength, confirming other authors findings [35]. Through numerical simulations, it was demonstrated that solar control coatings have low cooling consumptions (as found in [17]) and the lowest value was recorded by the niobium-based coating (CSOL3), thanks to the brown-grey colouring that reduces the solar gains. This coating ensures the best comfort condition, as demonstrated by the comparison of the medium operative temperatures in the summer period (Fig. 6.12a). On the other hand, this solution showed very high artificial lighting and winter heating consumptions. From an overall evaluation, the best energy, and environmental performance was recorded by the solar control coating with the highest Ag percentage (CSOL1).
The two low-emissivity coatings showed higher transmittance properties than the previous type, both in the visible and solar range [36], demonstrating higher consumptions in the summer period and lower heating and artificial lighting usages. Even in this case, the highest Ag concentration determined the highest performance.
The self-cleaning coating, even if having higher solar selectivity properties [18] with respect to an uncoated commercial glass, showed the worst energy and environmental performance among all the tested coatings, because of the very high cooling consumptions registered in the summer period.

(ii) Regarding the *effects of the artificial treatments*, the salt-spray environment resulted in having the highest incidence on the film performance and, after laboratory tests, the worst resistance was registered by the coatings with high silver percentages in the chemical compositions (the low-emissivity and two of the solar control films). This result is consistent

with the findings of other authors [9-13], demonstrating the instability of the silver-based coatings in humid environments. A better durability was shown by the sample doped with tin, thanks to the lowering of the film internal stress induced by the doping element [9]. As expected, the lowest decays were detected in coatings without silver elements, the titanium-based and the niobium-based films, for which only slight degradations were observed. In the previous type (the self-cleaning coating), the good durability could be explained with the super-hydrophilic effect of titanium nanoparticles [2], while the latter (solar control film) confirmed the good stability of niobium element, as stated in the literature [9].

(iii) Regarding the *decay of the films properties*, the detailed study of the performance reductions showed some similarity among coatings of different types.

With regard to optical and energy properties, almost all the samples showed decreasing transmittance values (and inversely increasing reflectance) in the visible range, due to white dots defections and particles deposition after the two ageing treatments. The niobium-based film demonstrated an opposite trend, probably for the physical deterioration of the dark coating. Moreover, all the coatings showed increasing transmittance values (and decreasing reflectance) in the solar range, confirming their insulating properties decay after ageing. The only exception was the self-cleaning sample, which demonstrated to enhance the solar reflectance values thanks to the photocatalytic effect occurred in the titanium nanoparticles. In this case, the results slightly differ with other authors findings [37]. This difference could be assigned to the unequal ageing period adopted, very shorter in the present experimentation. The degradation in the long term could have a negative effect on the films efficiency. Moreover, the improvement of the photocatalytic activity of the film could be ascribed to the high substrate temperature (40 °C in the climatic chamber), that has a great influence on the activity of the titanium nanoparticles [38].

About the energy performance, an increment of the emissivity values was observed for almost all the coatings.

With regard to energy demands and summer discomfort levels, obtained through an office room simulated in dynamic conditions, almost all the samples showed increasing values after ageing, with some exceptions. For each coating, a detailed plot of medium internal operative temperatures in summer for each coating adopted in the model, in aged conditions, is reported in Fig.6.12b. It is clear from the graph that the coatings that undergo the major effect of ageing are CSOL1 (that enhances the comfort properties respect to the initial condition and bringing the temperature down to the comfort range) and CSOL2 (that shows a reduction of comfort levels with increased temperature values). In fact, the solar control coating with the highest percentage of the silver element (CSOL1) demonstrated decreasing cooling energy demand: after the saline treatment, this coating had one of the worst performance in the physical test with stains on the glass surface, preventing the visible and solar transmissions. For this reason, this solar control film registered very lowered CO_2 emissions values. On the contrary, CSOL2 worsened the summer indoor conditions for its high physical degradation due to coating detachment (see *section 6.4.1.1*). As expected, the niobium-based solar control coating was the sole that showed a decrement of artificial lighting consumptions, since its deterioration took advantage of being brown coloured in the initial stage.

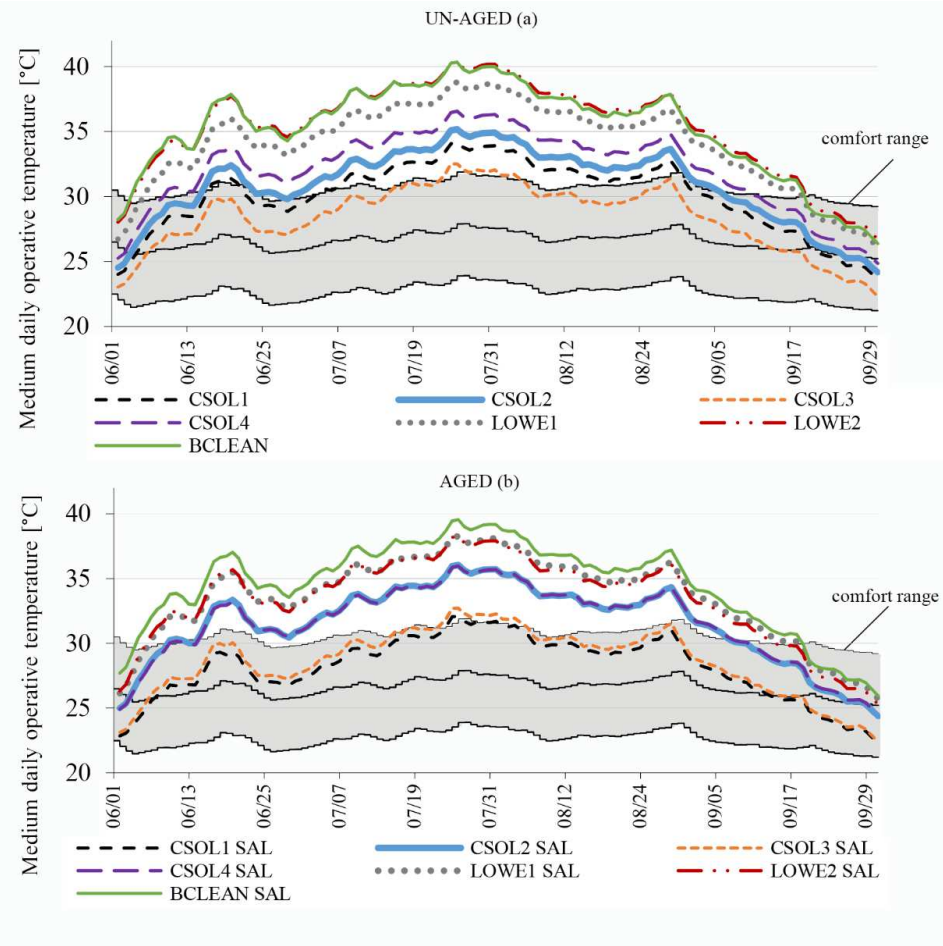

Figure 6.12. Comparison of the medium daily operative temperatures obtained for the coatings, before (a) and after (b) the saline exposure.

6.6 Conclusions

The present study aims to contribute to deepening the knowledge of the durability of three types of glass coatings (solar control, low-emissivity and self-cleaning) made of different metal elements, subjected to two ageing treatments, hot-wet and saline exposures. The performances were evaluated through several experimental tests and physical, chemical, optical and energy features were analysed. Furthermore, numerical simulations were carried

out to investigate the energy consumptions, comfort levels, solar gains and daylighting parameters of a double glazed unit with the selected coatings. Then, the environmental impact of the use phases was then evaluated.
From an overall evaluation the following observations could be drawn:

- The best solutions before ageing are the silver-based coatings. In a temperate climate, the solar control coated glass with the highest Ag percentage (81 %) is recommended for its high visible transmittance and its low energy cooling consumptions and environmental impact. In cold climates, instead, a silver-based Low-E coating is preferable because it guarantees winter and artificial lighting energy savings. The self-cleaning coating with titanium nanoparticles has the worst energy values among all the tested coatings.

- Among the two artificial ageing, the salt-spray environment has the highest incidence of almost all the coating types.

- After ageing, films with elevated silver percentages registered the worst physical and chemical resistances. The use of doping elements in the silver-based coatings improved their durability and, as expected, the best behaviour was registered by the titanium-based and niobium-based films.
Optical and energy features in silver-based coatings were strongly affected by ageing and, on the solar control film with the highest Ag percentage, the saline artificial treatment led to an unacceptable daylighting factor (less than 2 %). On the other hand, the analysis of energy consumptions and environmental impacts showed that the best performance was recorded by the silver-based coatings, even after ageing, because of their very high solar selectivity properties in the initial conditions.

From an overall evaluation in a temperate climate, the preferable solution is the solar control coating with a limit value of the silver percentage (of about 61 %) in the film composition (named CSOL2 in the present work).

According to these results, the longer the double glass components assembly is, the more the performance of the glass coating is reduced. Therefore, for the *Full Glass* window and the *Structural Member* for curtain walls, the optimization of the assembly phase was addressed.

6.7 References

[1] F. Stazi, M. Giampaoli, F. Tittarelli, C. Di Perna, P. Munafò. Durability of different glass coatings in humid and saline environments, ageing impact on heat-light transmission and thermal comfort. Building and Environment 105 (2016) 210-224

[2] C. G. Granqvist. Transparent conductors as solar Energy materials: A panoramic review. *Solar Energy Materials & Solar Cells* 91 (2007) 1529-1598

[3] M.C. Singh, S.N. Garg. R. Jha. Different glazing systems and their impact on human thermal comfort-Indian scenario. *Building and Environment* 43 (2008) 1596-1602

[4] D. Li, F. Huang, S. Ding. Sol-gel preparation and characterization of nanoporous ZnO/SiO_2 coatings with broadband antireflection properties. *Applied Surface Science* 257 (2011) 9752-9756

[5] D. R. Sahu, J. Huang. High quality transparent conductive ZnO/Ag/ZnO multilayer films deposited at room temperature. *Thin Solid Films* 515 (2006) 876-879

[6] K.H. Choi, J.Y. Kim, Y.S. Lee, H.J. Kim. ITO/Ag/ITO multilayer films for the application of a very low resistance transparent electrode. *Thin Solid Films* 341 (1999) 152-155

[7] G. Leftheriotis, S. Papaefthimiou, P. Yianoulis. Integrated low-emittance-electrochromic devices incorporating ZnS/Ag/ZnS coatings as transparent conductors. *Solar Energy Materials & Solar Cells* 61 (2000) 107-112

[8] M. Okada, M. Tazawa, P. Jin, Y. Yamada, K. Yoshimura. Fabrication of photocatalytic heat-mirror with $TiO_2/TiN/TiO_2$ stacked layers. *Vacuum* 80 (2006) 732-735

[9] E. Ando, M. Miyazaki. Durability of doped zinc oxide/silver/doped zinc oxide low emissivity coatings in humid environment. *Thin Solid Films* 516 (2008) 4574-4577

[10] E. Ando, M. Miyazaki. Moisture degradation mechanism of silver-based low-emissivity coatings. *Thin Solid Films* 351 (1999) 30-312

[11] M. Miyazaki, E. Ando. Durability improvement of Ag-based low-emissivity coatings. *Journal of Non-Crystalline Solids* 178 (1994) 245-249

[12] E. Ando, S. Suzuki, N. Aomine, M. Miyazaki, M. Tada. Sputtered silver-based low-emissivity coatings with high moisture durability. *Vacuum* 59 (2000) 792-799

[13] E. Ando, M. Miyazaki. Moisture resistance of the low-emissivity coatings with a layer structure of Al-doped ZnO/Ag/ Al-doped ZnO. *Thin Solid Films* 392 (2001) 289-293

[14] D.R. Sahu, J. Huang. Characteristics of ZnO/Cu/ZnO multilayer films on copper layer properties. *Applied Surface Science* 253 (2006) 827-832

[15] A. Cannavale, F. Fiorito, M. Manca, G. Tortorici, R. Cingolani, G. Gigli. Multifunctional bioinspired sol-gel coatings for architectural glasses. *Building and Environment* 45 (2010) 1233-1243

[16] G. Correa, R. Almanza. Copper based thin films to improve glazing for energy-savings in buildings. *Solar Energy* 76 (2004) 111-115

[17] E. Moretti, E. Belloni. Evaluation of energy, thermal, and daylighting performance of solar control films for a case study in moderate climate. *Building and Environment* 94 (2015) 183-195

[18] T. Tolke, A. Heft, A. Pfuch. Photocatalytically active multi-layer systems with enhanced transmission. *Thin Solid Films* 516 (2008) 4578-4580

[19] M. Batzill, U. Diebold. The surface and materials science of tin oxide. *Progress in Surface Science* 79 (2005) 47–154

[20] N. Ozer, M. D. Rubin, C. M. Lampert. Optical and electrochemical characteristics of niobium oxide films prepared by sol-gel process and magnetron sputtering. A comparison. *Solar Energy Materials and Solar Cells* 40 (1996) 285-296

[21] UNI EN 1096-2:2012. Glass in buildings. Coated glass. Part 2. Requirements and test methods for class A, B and S coatings

[22] UNI EN 410:2011. Glass in buildings. Determination of luminous and solar characteristics of glazing

[23] K. Tsikaloudaki, K. Laskos, T. Theodosiou, D. Bikas. The energy performance of windows in Mediterranean regions. *Energy and Buildings* 92 (2015) 180–187

[24] UNI EN 12898:2002. Glass in buildings. Determination of the emissivity

[25] J. Mohelnıkova. Method for evaluation of radiative properties of glass samples. *Applied Thermal Engineering* 28 (2008) 388–395

[26] UNI EN 673:2011. Glass in buildings. Determination of thermal transmittance (U value). Calculation method

[27] H. Manz, U. Menti. Energy performance of glazings in European climates. *Renewable Energy* 37 (2012) 226-232

[28] F. Stazi, S. Marinelli, C. Di Perna, P. Munafo. Comparison on solar shadings: Monitoring of the thermo-physical behavior, assessment of the energy saving, thermal comfort, natural lighting and environmental impact. *Solar Energy* 105 (2014) 512–528

[29] UNI TS 11300-1:2008. Energy performance of buildings. Part 1: Evaluation of energy need for space heating and cooling

[30] UNI EN 12464-1:2011.Light and lighting. Lighting of work places. Part 1. Indoor work places

[31] UNI EN ISO 15251:2008. Indoor environmental input parameters for design and assessment of energy performance of buildings addressing indoor air quality, thermal environment, lighting and acoustics

[32] ISO 14040:2006. Environmental management. Life cycle assessment. Principles and framework

[33] N. Usha, R. Sivakumar, C. Sanjeeviraja, Y. Kuroki. Effect of substrate temperature on the properties of Nb2O5:MoO3 (90:10) thin films prepared by rf magnetron sputtering technique. *Journal of Alloys and Compounds* 649 (2015) 112-121

[34] W. Tongon, C. Chawengkijwanich, S. Chiarakorn. Multifunctional Ag/TiO_2/MCM-41 nanocomposites film applied for indoor air treatment. *Building and Environment* 82 (2014) 481-489

[35] K. Yoshimura, T. Mild, S. Iwama, S. Tanemura. Characterization of niobium oxide electrochromic thin films prepared by reactive d.c. magnetron sputtering. *Thin Solid Films* 281-282 (1996) 235-238

[36] G. Leftheriotis, P. Yianoulis. *Glazing and coatings* (2012) Elsevier Ltd

[37] A. Chabas, S. Alfaro, T. Lombardo, A. Verney-Carron, E. Da Silva, S. Triquet, H. Cachier, E. Leroy. Long term exposure of self-cleaning and reference glass in an urban environment: A comparative assessment. *Building and Environment* 79 (2014) 57-65

[38] E. I. Cedillo-Gonzalez, R. Riccò, M. Montorsi, M. Montorsi, P. Falcaro, C. Siligardi. Self-cleaning glass prepared from a commercial TiO2 nano-dispersion and its photocatalytic performance under common anthropogenic and atmospheric factors. *Building and Environment* 71 (2014) 7-14

6.8 List of tables and figures

Nomenclature

Figure 6.12. Comparison of the medium daily operative temperatures obtained for the coatings, before (a) and after (b) the saline exposure.

Chapter 7

Effects on the market: *Full Glass* window and *Structural Member* for curtain walls

The aim of this research is the transfer of innovative construction elements to the market, particularly the *Full Glass* window and the *Structural Member* for curtain walls.
In a previous work [1], the research group illustrated the *Full Glass* industrialization process, which included the research activity, the patenting of the idea, the industrialization of the component and the market placement. The results demonstrated the feasibility of this process, which is founded on the "Technological Simplification". The principle is the use of innovative materials (such as GFRP pultruded profiles and structural adhesives) which, thanks to their high mechanical and thermal properties, allow the design and the production of construction elements with less components than the traditional ones. Furthermore, the production process is feasible for manufacturers without changing their production line. The results are ease of production and installation and, simultaneously, the reduction of the environmental impact.
In this section, the market investigation of windows and curtain walls is reported, as well as analysis of the production costs.

7.1 Windows and curtain walls market

With the objective of *Full Glass* and *Structural Member* commercialisation, a market analysis was carried out, both on national and international (Europe and the USA) levels. The market data showed positive trends, both for windows and curtain walls. According to a global research [2], the market will increase exponentially in 2018 and the request will mainly concern high thermal performance products. If only considering the window market, the trade covers over 17 billion euros [3].

7.1.1) The European market

According to the report of Interconnection Consulting [2], the European window market will increase exponentially in 2018.

The wood-metal window market will gain shares from 7,7 % in 2009 to 10,6 % in 2017. A consistent decrease in both the wood window market (-14 %) and the aluminum one (-8,3 %) was predicted. An increase for the PVC-aluminum window market was also forecasted.
The market shares are: wood: 18,7 %, aluminium: 27 %, wood-metal: 10 %, PVC-aluminium: 3,7 %.

7.1.2) The USA market

According to the report of Freedonia Inc. [2], the USA window market will increase with a different requirement: high-energy efficient products, such as triple glasses and thermal-insulated surfaces will increase in demand.
The aluminum window market still remains the market leader until 2018, despite the strong competition from plastic windows, which have lower prices than aluminum ones. The wood window market will increase up to 10,1 billion dollars in 2018.

7.1.3) The Italian market

According to the report of UNICMI [4], despite the actual construction market crisis, the window and curtain walls market are registering positive trends, reaching respectively the values of 1.404 and 474 million euros (Figures 7.1 e 7.2).

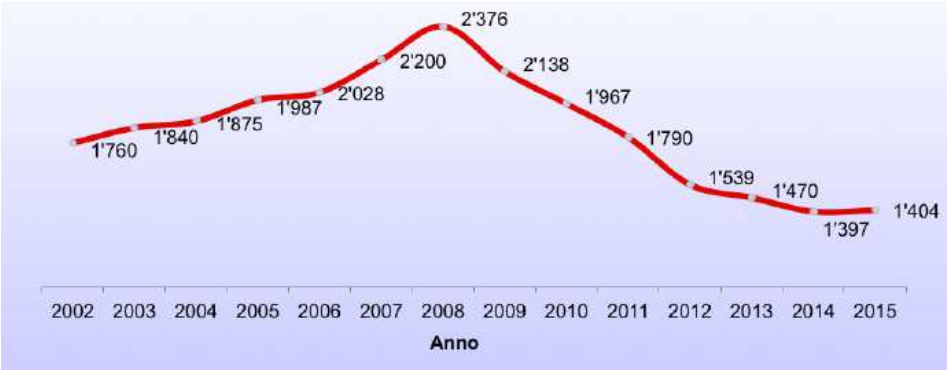

Figure 7.1. Windows market trend (values in millions of euros, UNICMI report 2016 [4]).

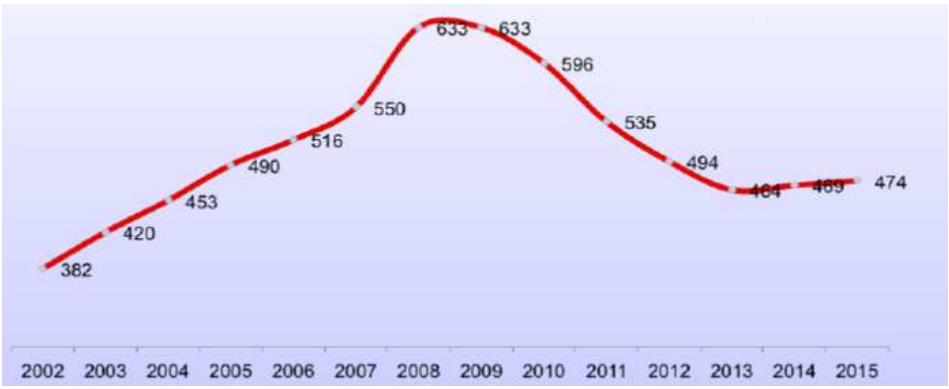

Figure 7.2. Curtain walls market trend (values in millions of euros, UNICMI report 2016 [4]).

Furthermore, the *Full Glass* window and the *Structural Member* for curtain walls are applicable both in new constructions and in restorations, the latter constituting 71,9 % of the total investments in the construction sector.

7.1.3.1) The market sector

The Italian market sector is highly fragmented, due to the prevalence of small size companies. Only 1857, of the total amount of 12000, are capital companies. In this sector, two different groups are distinguished:
- the windows manufacturers, which are small-medium sized companies; the materials used are wood, aluminum, and PVC. The business model is nearly based on an ample and diversified offer, therefore the companies are able to cover several markets sectors (figure 7.3);
- the curtain walls manufacturers, which are medium-large sized companies; they are specialized on the curtain walls construction and they operate also in the international market. The main markets are England, France, South-West Asia, Medium Orient and USA (figure 7.4).

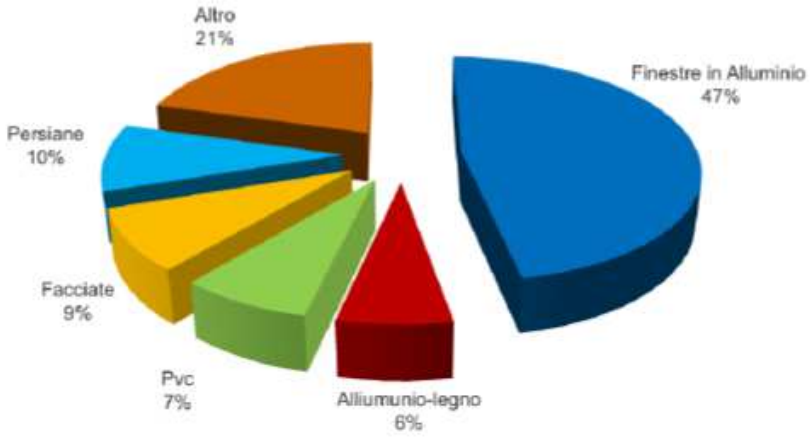

Figure 7.3. The distribution of the windows market (UNICMI report 2016 [4]).

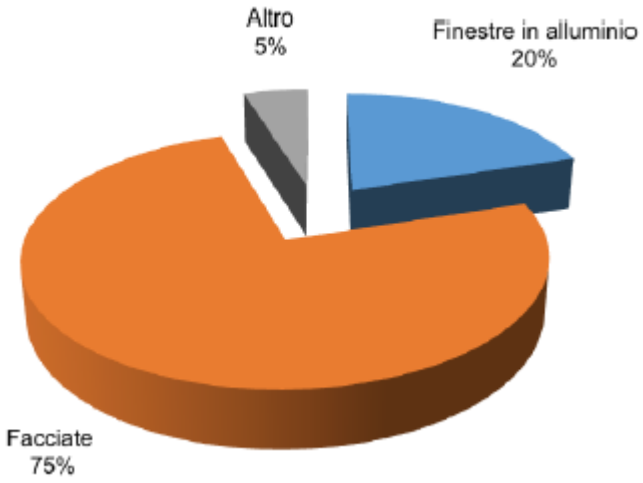

Figure 7.4. The distribution of the curtain walls market (UNICMI report 2016 [4]).

Thanks to the high thermal and mechanical properties of the GFRP profiles, the *Full Glass* window and the *Structural Member* for curtain walls have a special design. The frame section of the *Full Glass* is very reduced, almost invisible, and the glass surfaces of the curtain walls

realized with the *Structural Member* are wider than in the other construction elements available on the market, also with smaller frames sections. Both the products can be used in new constructions and in restorations.
The UNICMI report showed that the customer's choice is in accordance with the maximum ratio of "value for money", and high thermal performance products are mostly preferred. Both the *Full Glass* window and the *Structural Member* for curtain walls are in accordance with this trend since their prices are competitive with those of the other components with similar performances available on the market (see section 7.1.3.4).

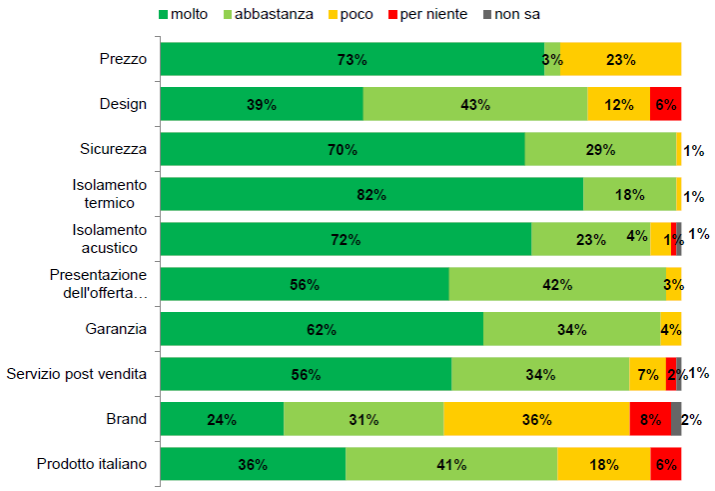

Figure 7.5. Windows customer's choice parameters (UNICMI report 2016 [4]).

7.1.3.2) The possible competitors

Very few Italian manufacturers produce windows with GFRP pultruded frames. These companies (Tip Top Fenster, Agostini e Levante serramenti) are aluminum and plastic window manufacturers that decided to widen the range of products with innovative materials (such as GFRP pultruded profiles) following the traditional technical/constructional concept (the large window frame sizes). The number of international manufacturers is higher than the national one, especially in the European (Germany, Denmark, Finland) and North American countries, which operate in the world market.
With regard to curtain walls, the Italian market is not covered and the main manufacturers (Metra, Aluk, Zanetti, Wicona) produce aluminum frames. The same conclusion can be drawn from the analysis of the international market.

7.1.3.3) The possible customers

The possible customers of the *Full Glass* window and the *Structural Member* for curtain walls are:
- the manufacturers of window and curtain walls. Even though they are possible competitors, they could sell the two patents in order to increase and innovate their products;
- the manufacturers of GFRP pultruded profiles and double glass. They could be interested in creating an inner section dedicated to the production of windows and curtain walls;
- engineers and architects, which could be interested in employing the two construction elements in building design.

7.1.3.4) Production costs and sales prices

The production costs of the *Full Glass* window and the *Structural Member* for curtain walls were evaluated by adding together the individual costs of their components.

With regard to the *Full Glass*, the following components were taken into account: the GFRP profiles constituting the mobile and fixed frames, the double glass, the steel counter frame, the adhesive, the mobile frame-double glass installation, the handling systems, gaskets and metallic parts (excluding the costs of the on-site installation.
As shown in Table 7.1, the production costs of the *Full Glass* window are lower than aluminum windows with thermal break with the same double glass break (available on the market). Furthermore, the innovative window has better thermal performance than the aluminum one.

Table 7.1. Production costs comparison of the Full Glass and one of the best aluminum thermal break windows available on the market (Schuco).

	FULL GLASS GFRP profiles frame, two-wing window				***SCHUCO*** Aluminium thermal break frame, two-wing window		
	Mobile and fixed GFRP frames + steel counter frame + assembly	Complete frame	Complete frame + laminated double glass	Complete frame + laminated double glass + coating and gas	Aluminum frame + steel counter frame + assembly	Complete frame + laminated double glass	Complete frame + laminated double glass + coating and gas
Costs (euros/kit)	206,00	243,00	353,00	511,00	270,00	417,00	573,00

With regard to the *Structural Member* for curtain walls, the following components were taken into account: the GFRP profiles (C and double T sections), the steel wires (one/four), the adhesive, the steel laminates and the steel connection systems.
As shown in Table 7.2, the production costs of the *Structural Member* are competitive with respect to an aluminum frame for curtain walls only for the C-section, while the GFRP frame with double T-section is more expensive. On the other hand, the number of GFRP frames is lower than the aluminum ones (of about 10 %) thanks to the high mechanical properties of the fibre-reinforced composite material. Furthermore, the GFRP profiles section areas are very reduced, in favor of the aesthetic of functional aspects.

Table 7.2. Production costs comparison of the Structural Member and one of the best aluminum frame for curtain walls available on the market (Metra).

	Structural Member for curtain walls GFRP		***METRA frame for curtain walls*** Aluminium
	C-section with 1 steel wire	Double-T section with 4 steel wires	Squared tubular section
Costs (euros/m)	35,00	90,00	20,00

With regard to sales prices, considering the high quality of the *Full Glass* and the *Structural Member*, some profit margins were assumed. However, the resulting prices are competitive with similar products available on the market.
- *Full Glass* two-wing window with laminated double glass: ***455 euro/mq*** + IVA (production cost of 360 euro/mq);
- *Full Glass* two-wing window with laminated double glass + argon gas: ***610 euro/mq*** + IVA (production cost of 510 euro/mq);
- *Structural Member*, C-section with 1 steel wire: ***70 euro/m*** + IVA (production cost of 35 euro/ml);
- *Structural Member*, double-T section with 4 steel wires: ***180 euro/m*** + IVA (production cost of 90 euro/ml).

7.2 References

[1] M. Giampaoli, V. Terlizzi, P. Munafò. Risultanze di un processo di industrializzazione di un'idea brevettuale: finestra di solo vetro senza telaio "Full Glass". *Colloqui.AT.e* Artec (2016) 120-121

[2] www.puntodfv.it

[3] Ulisse Magazine. Il commercio mondiale di finestre e portefinestre in legno (2013)

[4] UNICMI. Rapporto sul mercato italiano dell'involucro edilizio. Uncsaal servizi srl (2016)

7.3 List of tables and figures

Chapter 8

Conclusions

Thanks to the numerous advantageous properties innovative materials, such as GFRP pultruded profiles, structural adhesives and solar selective coatings, can be used to lower the number of pieces of construction elements. This concept demonstrates the feasibility of the "Technological Simplification" principle in the design of the components, which led to much easier production and installation phases and to the reduction of environmental impact thanks to lower CO_2 emissions, in both the production and the durability aspects [1].
In this work, the applicability of these innovative materials on construction elements, such as windows and curtain walls, is demonstrated through the validation of the basic principles of the patents designed by the research group, the *Full Glass* window (patent n. PCT/IB2014/066098) and the *Structural Member* for curtain walls (patent application n. 102015000087569).
The experimental studies demonstrated that:

(i) The mechanical performance of the GFRP profiles with polyester matrix was only slightly affected by high moisture levels, especially the tensile properties that showed decrements of about 5 % with respect to the un-aged values [2]. **These results confirmed the applicability of GFRP pultruded profiles on windows and curtain walls.**

(ii) Results showed epoxies as the best adhesive for joining GFRP profiles, in terms of load carrying capacity and stiffness. However, it is necessary to consider the high deformations (+70÷90 %) that can occur when the joints subjected to high temperatures and moisture levels and after UV irradiation [3]. **Therefore, in order to avoid undesired deformations of the bonding conjunctions, small metal "L" profiles were inserted in the mobile frame.**

(iii) The compatibility between GFRP and steel profiles was stated and the method of hybridization resulted advantageous in the stiffness of GFRP profiles, even when the bonding system is exposed to adverse environmental conditions (high temperatures and moisture levels and after UV irradiation). **These results confirmed the reliability of the *Structural Member* for curtain walls basic principle.**

(iv) The solar selective coatings with high quantities of silver are recommended for their high visible transmittance, low energy consumptions, and environmental impact. On the other

hand, these film types are strongly affected by the ageing treatments, especially by the saline spray, and a limit value of the silver percentage (of about 61%) in the film composition was stated [4]. **According to this result, the longer the double glass components assembly is, the more the performance of the glass coating is reduced. Therefore, for the *Full Glass* window and the *Structural Member* for curtain walls, the optimization of the assembly phase was addressed.**

The results obtained through experimental tests on GFRP profiles-glass bonded specimens, which is **the basic principle of the Full Glass patent**, are currently being assessed and analysed. **The data showed that the bonded joints are able to withstand the maximum working stresses to which a window may be subjected, with an adequate coefficient of safety, also after the ageing treatments.**

After the validation of the patents basic systems, the research activity addressed the *industrialization process* of the Full Glass window [5]. The aim was to demonstrate the feasibility of the window's series production, with the objective to its national and international commercialization.

For this purpose, the *design and optimization of the components* (profiles and gaskets) were carried out. These phases were necessary to verify and to define the assembly and the geometries of the components, in connection with the industrial production process.
Firstly, a 3d model was realized with the aid of Autocad software. Later, the prototype of the mobile-fixed frames conjunction was done, through a 3d printing technique. This model was useful to modify the previous technical drawings and to enhance the thermal performance of the system.
Subsequently, the design phase of the profiles was performed, according to the industrialization production process, and it was developed in cooperation with manufacturers. The pultrusion process takes place through the use of steel dies (the tools) which mold the GFRP profiles. In this phase, some design rules are necessary for the proper production, such as: curve radii, tolerances, gaps, minimum thicknesses, resin, roving, and mat. Moreover, the addition of additives to the matrix resin and the protection film positioned on the profiles surfaces was considered.
The objective of the entire phase was the *prototype realization* in a real scale, in order to certify the *Full glass* window. This process also allowed to define the components series production, maintaining a standard quality within a specific range.

Furthermore, the *window market analysis* and the *production costs evaluation* were carried out, demonstrating that the Full Glass window is competitive with the analogous windows, with higher design and thermal insulation qualities.

With regard to the *commercializatio*n step, the use of electronic labelling was evaluated to protect industrial properties rights. The objectives are the suppression of the falsification, the control of sales and the management of the warehouse, in order to have a proper understanding of the current situation.

In extreme summary, **the research activity allowed to reach the main objective, i.e. to verify the feasibility of a research result (the Full Glass window patent n. PCT/IB2014/066098) transfer to the production world and, then, to the market.** The industrialization process of the *Structural Member* for curtain walls will be the aim of the next phase.

8.1 References

[1] P. Munafò. Considerazioni sulle tematiche di ricerca del Settore Scientifico Disciplinare di Architettura Tecnica. *Colloqui.AT.e* Artec (2015) 21-24

[2] F. Stazi, M. Giampaoli, L. Nisi, M. Rossi, P. Munafò. Mechanical performance reduction of GFRP specimens with polyester matrix exposed to continuous condensation. *Composites Part B* 99 (2016) 330-339

[3] Stazi F, Giampaoli M., Rossi M, Munafo P. Environmental ageing on GFRP pultruded joints: Comparison between different adhesives. *Composite Structures* 133 (2015) 404–414

[4] F. Stazi, M. Giampaoli, F. Tittarelli, C. Di Perna, P. Munafò. Durability of different glass coatings in humid and saline environments, ageing impact on heat-light transmission and thermal comfort. *Building and Environment* 105 (2016) 210-224

[5] M. Giampaoli, V. Terlizzi, P. Munafò. Risultanze di un processo di industrializzazione di un'idea brevettuale: finestra di solo vetro senza telaio "Full Glass". *Colloqui.AT.e* Artec (2016) 120-121

Appendix 1

Fibre Reinforced Polymers

Some contents of this chapter are extracted from the Fibreglass internet website: www.moldedfibreglass.com.

1.1 Composite materials – FRP and GFRP

Composite materials are a combination of two or more materials with significantly different physical or chemical properties, which remain separate and distinct within the finished structure. Composite properties are determined by chemical and mechanical interaction of the combined materials and the objective is usually to make a component that is strong and stiff, often with a low density.

Modern composites are usually made of two components, fibres, and matrix, known as *Fibre-Reinforced Polymers (FRP)*. The fibres are most often glass, but sometimes Kevlar, carbon fibre, or polyethylene. The matrix, which is weaker and less stiff than fibres, is usually an epoxy, vinyl ester or polyester thermosetting plastic. The fibres are embedded in the matrix in order to make the matrix stronger [1].

Figure 1.1. The combination of fibres and matrix in FRP composites.

The applications of FRP (Fig. 1.1) are:
- Marine transportation components.
- Architectural cladding components.
- Aerospace transportation and weapons components.

- Automotive components.
- Energy sector components (wind turbines).
- Static structural components (buildings/bridges).

Figure 1.2. Different applications of FRP composites

The most common fibre-reinforced polymer composites are based on glass fibres, mat, or roving embedded in a matrix of an epoxy or polyester resin. *Glass Fibre Reinforced Polymers (GFRP)* profiles were developed commercially after World War II and, since that time, their use has grown rapidly. This is because this advanced material combines excellent mechanical/physical performances and high cost- effectiveness, with environmental sustainability. The main advantages respect to metallic materials are the reduction in weight up to 60 %, the improved surface quality and the decrease in components by combining parts and forms into simpler molded shapes [1].

1.2 Benefits and features of FRP materials

The use of FRP materials led to numerous advantages and these beneficial properties should be considered in the design processes.

Corrosion resistance. FRP materials do not rust, corrode or rot, and they resist attack from most industrial and household chemicals. This quality has been responsible for applications in corrosive environments such as those found in the chemical processing and water treatment industries. Resistance to corrosion provides long life and low maintenance in marine applications from sailboats and minesweepers to seawalls and offshore oil platforms.

High strength, lightweight. FRP materials provide high strength to weight ratios exceeding those of aluminum or steel. High strength, lightweight FRP materials are a rational choice whenever weight savings are desired, such as components for the transportation industry.

Dimensional stability. FRP materials have high dimensional stability under varying physical, environmental, and thermal stresses. This is one of the most useful properties of FRP materials.

Parts consolidation and tooling minimization. A single FRP composite molding often replaces an assembly of several metal parts and associated fasteners, reducing assembly and handling time, simplifying inventory, and reducing manufacturing costs. A single FRP profile tool can replace several progressive tools required in metal stamping.

High dielectric strength and low moisture absorption. The excellent electrical insulating properties and low moisture absorption of FRP materials qualify them for use in primary support applications such as circuit breaker housings, and where low moisture absorption is required.

Minimum finishing required. FRP materials can be pigmented as part of the mixing operation or coated as part of the molding process, often eliminating the need for painting. This is particularly cost effective for large components such as tub/shower units. Also, on critical appearance components, a class "A" surface is achieved.

Low to moderate tooling costs. Regardless of the molding method selected, tooling for FRP materials usually represents a small part of the product cost. For either large-volume mass-production or limited runs, tooling cost is normally substantially lower than that of the multiple forming tools required to produce a similar finished part in metal.

Design flexibility. No other major material system offers the design flexibility of FRP materials. Present applications vary widely. They range from commercial fishing boat hulls and decks to truck fenders, from parabolic TV antennas to transit seating, and from the outdoor lamp, housings to seed hoppers. What the future holds depends on the imagination of today's design engineers as they develop even more innovative applications for FRP materials.

1.3 Classification of FRP materials

There are two classification systems for composite materials. One of them is based on the matrix material and the second is based on the reinforcement material type and structure.

1.3.1) The matrix

The matrix or resin is the other major component of an FRP material. Resin systems are selected for their chemical, electrical and thermal properties. The two major classes of resins are thermosets and thermoplastics.

1.3.1.1) Thermoset resins

Thermosetting polymers are usually liquid or low melting point solids that can easily combine with fibres or fillers prior to curing. Thermosets feature cross-linked polymer chains that become solid during a chemical reaction or "cure" with the application of a catalyst and

heat. The high level of cross-linking provides for reduced creep compared to thermoplastics. The thermoset reaction is essentially irreversible.

Among the thermoset resins for FRP materials, the family of unsaturated *polyesters* is by far the most widely used. These resins are suitable for practically every molding process available for thermosets. Polyesters offer ease of handling, low cost, dimensional stability, and a balance of good mechanical, chemical, and electrical properties. They can be formulated for high resistance to acids, weak alkalies, and organic solvents. They are not recommended for use with strong alkalis. Other formulations are designed for low or high-temperature processing, for room temperature or high-temperature cure, or for flexible or rigid end products.

Vinyl esters provide excellent resistance to water, organic solvents, and alkalis, but less resistance to acids than polyesters. Vinyl esters are stronger than polyesters and more resilient than epoxies. Molding conditions for vinyl esters are similar to those for polyesters.

Epoxies are another family of thermoset resins used in FRP materials. They have excellent adhesion properties and are suited for service at higher temperatures – some as high as 500ºF. Epoxy-matrix FRP materials are processed by any of the thermoset methods. Epoxies are more expensive than polyesters, and cure times are longer, but their extended range of properties can make them the cost/performance choice for critical applications. Epoxy/fibre structures have generally higher fatigue properties than polyesters.

Polyurethanes are a family of resins that offer very high toughness, high elongation, faster cure times and good coupling to a variety of reinforcements. Polyurethanes are easily foamed in a controlled process to produce a wide range of densities. Additives are easily incorporated into resin systems to provide pigmentation, flame retardance, weather resistance, superior surface finish, low shrinkage and other desirable properties.

Gel coats consisting of a special resin formulation provide an extremely smooth next-to-mold surface finish on FRP materials. They are commonly applied in hand lay-up and spray-up processes to produce a tough, resilient, weather-resistant surface. Gel coats, which may be pigmented, are sprayed onto the mold before the reinforcement and resin are introduced.

Other thermosetting resin systems, generally formulated with chopped strand or milled fibre reinforcement for compression or transfer molding are:
Phenolics: good acid resistance, good fire/smoke, and thermal properties.
Silicones: highest heat resistance, low water absorption, excellent dielectric properties.
Melamines: good heat resistance, high impact strength.
*Diallyl phthalates: g*ood electrical insulation, low water absorption.

1.3.1.2) Thermoplastic resins

Thermoplastic polymers can soften and become viscous liquids when heated for processing and then become solid when cooled. The process is reversible allowing a reasonable level of process waste and recycled material to be reused without significant effect on the end product. Thermoplastic resins allow for faster molding cycle times because there is no

chemical reaction in the curing process. Parts may be formed as fast as heat can be transferred into and out of the molding compound.

Polypropylene and *polyethylene* are the most common thermoplastic resins used in FRP materials. They have excellent resistance to acids and alkalies and have good resistance to organic solvents. Their relatively low melting points allow for rapid processing at a lower cost.

Nylon and *Acetal* are highly resistant to organic solvents and may also be used where increased mechanical properties are required.

1.3.2) Reinforcements

Much of the strength of FRP materials is due to the type, amount and arrangement of the fibre reinforcement. While over 90% of the reinforcements in use are glass fibres, other reinforcements have established a critical niche.

The *glass* fibres are the most commonly used reinforcement type. It is strong, has good heat resistance, and high electrical properties.

Carbon fibres (graphite) are available in a wide range of properties and costs. These fibres combine light weight with very high strength and modulus of elasticity. The modulus of elasticity is a measure of the stiffness or rigidity in a material. For high stiffness applications, these reinforcements are hard to beat, with a modulus of elasticity that can equal steel. FRP materials with carbon fibre reinforcement also have excellent fatigue properties. The primary use of carbon fibres is in aircraft and aerospace, in which weight savings are a major objective. While its cost limits carbon's use in commercial applications, it is used extensively where material content is low, such as sporting equipment.

Aramid or aromatic polyamide fibres provide high strength and low density (40% lower than glass) as well as the high modulus. These fibres can be incorporated in many polymers and are extensively used in high impact applications, including ballistic resistance.

Natural fibres such as Sisal, Hemp and Flax have been used for many applications with low strength
requirements. They are limited to applications not requiring resistance to moisture or high humidity.

The *arrangement* of the glass fibres - how the individual strands are positioned – determines both direction and level of strength achieved in a molded FRP/Composite. The three basic arrangements of glass
fibre reinforcement are unidirectional, bidirectional and multidirectional.

Unidirectional arrangements provide the greatest strength in the direction of the fibres. Unidirectional fibres can be continuous or intermittent, depending on specific needs determined by part shape and process used. This arrangement permits very high reinforcement loading for maximum strengths.

The fibres in *a bidirectional* arrangement are in two directions – usually at 90^0 to each other, thus providing the highest strength in those directions. The same number of fibres need not necessarily be used in both directions. High fibre loading can be obtained in woven bidirectional reinforcements.

Multidirectional or random arrangements provide essentially equal strength in all directions of the finished part.

1.3.2.1) Reinforcement forms

Reinforcements are supplied in several basic forms to provide flexibility in cost, strength, compatibility with the resin system, and process requirements. Regardless of the final form, all fibre reinforcements originate as single filaments. A large number of filaments are formed simultaneously and gathered into a strand. A surface treatment is then applied to facilitate subsequent processing, maintain fibre integrity, and provide compatibility with specific resin systems. After this treatment, the strands are further processed into various forms of reinforcements for use in molding FRP materials.

Continuous strand roving. This basic form of reinforcement is supplied as untwisted strands wound into a cylindrical package for further processing. Continuous roving is typically chopped for spray-up, preform or sheet molding compounds. In the continuous form, it is used in pultrusion and filament winding processes.

Woven roving. Woven from continuous roving, this is a heavy, drapable fabric available in various widths, thicknesses, and weights. Woven roving costs less than conventional woven fabric and is used to provide high strength in large
structural components such as tanks and boat hulls. Woven roving is used primarily in hand lay-up processing.

*Woven fabrics.*Made from fibre yarns, woven fabrics are of a finer texture than woven roving. They are available in a broad range of sizes and in weights from 21/2 to 18 oz./sq. yd. Various strength orientations are also available.

Reinforcing mat. Made from either continuous strands laid down in a swirl pattern or from chopped strands, reinforcing mat is held together with a resinous binder or mechanically stitched. These mats are used for medium strength FRP materials. Combination mat, consisting of woven roving and chopped strand mat bonded together, is used to save time in hand lay-up operations. Hybrid mats of glass and carbon and aramid fibres are also available for higher-strength reinforced products.

*Surfacing mat***.** Surfacing mat or veil is a thin fibre mat made of monofilament and is not considered a reinforcing material. Rather, its purpose is to provide a good surface finish because of its effectiveness in blocking out the fibre pattern of the underlying mat or fabric. Surfacing mat is also used on the inside layer of corrosion-resistant FRP/Composite products to produce a smooth, resin-rich surface.

Chopped fibres. Chopped strands or fibres are available in lengths from 1/8" to 2" for blending with resins and additives to prepare molding compounds for compression or injection molding and other processes. Various surface treatments are applied to ensure optimum compatibility with different resin systems.

Figure 1.3. Continuous strand roving, woven roving and chopped fibres.

1.4 The surface interaction of fibre and resin

The mechanical performance of a composite material is highly dependent upon the quality of the fibre–matrix interface. This region is an anisotropic transition region which is required to provide chemical and physical bonding between the fibre and the polymer. The primary aim of a fibre reinforced matrix composite
material is to provide an average behaviour of the composite from the properties of the components which must act compositely for the material to be efficient. It is well known that the application of a coupling agent to a glass fibre surface will improve fibre–matrix adhesion in that composite but in addition, and to a greater degree, it is the mixing of the processing additives; this contribution to composite properties is not well understood. The interfacial region of the composite will, therefore, be affected not only by the composition of the coating but also by its distribution on the glass fibre surface and in the composite matrix [2].

1.5 The pultrusion process

The process whereby fibrous materials are bonded with the matrix is called the molding process. There are different forms of composites moldings, and one well-known method is the pultrusion, whereby industrialized profiles are realised. In this process, fibre bundles and slit fabrics are pulled through a wet bath of resin and formed into the rough part shape. The saturated material is extruded from a heated closed die curing while being continuously pulled through die. Some of the end products of the pultrusion process are structural shapes,

i.e. beam, angle, channel and flat sheet. These materials can be used to create all sorts of fibre structures such as ladders, platforms, handrail systems tank, pipe, and pump supports [1].

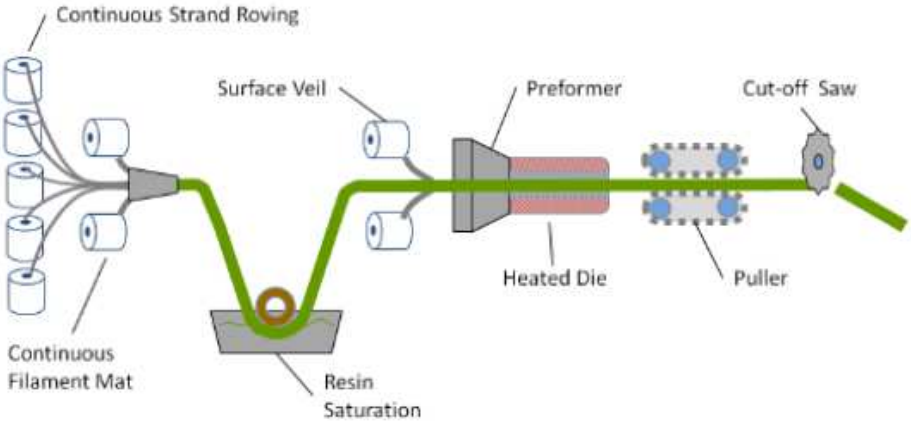

Figure 1.4. Scheme of the pultrusion process.

1.6 References

[1] Masuelli M. A. Introduction of Fibre-Reinforced Polymers – Polymers and Composites: Concepts, Properties and Processes. ISBN 978-953-51-0938-9, Argentina (2013)

[2] Hollaway L.C. A review of the present and future utilisation of FRP composites in the civil infrastructure with reference to their important in-service properties. *Construction and Building Materials* 24 (2010) 2419–2445

1.7 List of figures

Appendix 2

Adhesives

Some contents of this chapter are extracted from the Fibreglass internet website: www.adhesives.org.

2.1 Adhesives

An adhesive may be defined as a material which can join the surfaces together and resist their separation [1]. Recent advances in adhesive technology have led to a rapid growth in the use of adhesives in load-bearing joints, achieving structural performances and being used in civil engineering applications. The use of adhesives, in fact, can prove more convenient, less expensive, stronger, and more durable than traditional methods of joining [1].

Figure 2.1. The use of adhesives in the building/construction field.

2.2 Benefits of adhesives

The development of new materials with diverse applications puts additional challenges on processing technology. This is particularly so when different materials have to be joined to make components which retain their individual beneficial properties in the composite product. Traditional joining techniques have well-known disadvantages. With thermal techniques such as welding, the specific properties of the material alter within the heat-

affected zone. Mechanical techniques such as riveting or the use of screws in their turn only allow force transfer at points; in addition, it is necessary to drill holes in the workpieces that are being joined, and this "damages" and hence weakens the materials. In contrast, bonding technology will assume an ever more important role in industry and the handicraft sector in the future. There are four key reasons for this:

1. Material: with the specialist application, bonding technology can be used to bond virtually any desired combination of materials with each other, creating long-lasting bonds.

2. *Processing:* the use of bonding technology in production processes, in general, allows the material properties of the substrates to be retained. Compared to welding and soldering/brazing, the bonding process requires relatively little heat input. No damage occurs, unlike when rivets or screws are used.

3. *Joining:* **i**n product manufacture, the two aforementioned considerations enable the specific material properties of substrates to be optimally utilized in components. This allows new construction methods to be employed.

4. *Design*: it is also possible to use bonding technology to introduce customized additional properties into the component via the actual joining. In addition, the use of bonding technology in industrial production can lead to time savings, can accelerate the production process and hence give rise to specific economic benefits. In shipbuilding, for example, the inside decks can nowadays be bonded into the primary structure, so eliminating time-consuming straightening work that would be required if the inside decks were attached by welding.

Bonding technology also has the following *further advantages:*

- Transfer of high lap shear stresses due to the large bonding areas.
- Removal of unevenness on material surfaces; greater tolerances possible using gap-filling adhesives.
- Prevention of contact corrosion for metal bonds, in contrast to when rivets or screws are used (the adhesive functions as an insulator).

2.3 Classification of adhesives

There are a large number of adhesive types for various applications. They may be classified in a variety of ways depending on their chemistries, their form, their cure mechanism, or their load carrying capability.

2.3.1) Load carrying capacity

2.3.1.1) Structural

Structural adhesives refer to relatively strong adhesives that are normally used well below their glass transition temperature, an important property for polymeric materials, above which polymers are rubbery and below which they are glassy. Common examples of structural adhesives include epoxies, cyanoacrylates, and certain urethanes and acrylic

adhesives. Such adhesives can carry significant stresses, and lend themselves to structural applications.

2.3.1.2) Semi-structural and non-structural

For many engineering applications, semi-structural (applications where failure would be less critical) and non-structural (applications of facades, etc. for aesthetic purposes) are also of significant interest to the design engineer and provide cost-effective means required for assembly of finished products. These include contact adhesives where a solution or emulsion containing an elastomeric adhesive is coated onto both adherents, the solvent is allowed to evaporate, and then the two adherents are brought into contact. Examples include rubber cement and adhesives used to bond laminates to countertops.

2.3.1.3) Pressure sensitive

Pressure sensitive adhesives are very low modulus elastomers, which deform easily under small pressures, permitting them to wet surfaces. When the substrate and adhesive are brought into intimate contact, van der Waals forces are sufficient to maintain the contact and can provide relatively durable bonds for lightly loaded applications. Pressure sensitive adhesives are normally purchased as tapes or labels for non-structural applications, although can also come as double-sided foam tapes which can be used in semi-structural applications. As the name implies, hot melts become liquid when heated, wetting the surfaces and then cooling into a solid polymer. These materials are increasing used in a wide array of engineering applications using more sophisticated versions of the glue guns widely used by consumers. Anaerobic adhesives cure within narrow spaces deprived of oxygen; such materials has been widely used in mechanical engineering applications to lock bolts or bearings in place. Cure in other adhesives may be induced by exposure to ultraviolet light or electron beams, or may be catalyzed by certain materials such as water, which are ubiquitous on many surfaces.

2.3.2) Cure mechanisms

2.3.2.1) Physically hardening

Physically hardening adhesives are adhesives which, on the application, are already present in their final chemical state. Only polymers that can be liquefied can be used for this category of adhesive, namely thermoplastics that can be melted, soluble thermoplastics or elastomers, or polymer dispersions. Although poorly crosslinked elastomers with good swelling properties are strictly speaking insoluble, they can still be used in certain cases to produce adhesives if they swell enough for the substrates to be wetted. Physically hardening adhesives provide a wide range of adhesive properties, generally good bond flexibility, and are used in a variety of applications. Four physically hardening adhesives are:

- Hot melts;
- Organic solvent adhesives;
- Plastisols;
- Water-based adhesives.

2.3.2.2) Chemically curing

Chemically curing adhesives are reactive materials that require a chemical reaction to convert them from the liquid (or thermoplastic) to solid. Once cured, these adhesives generally provide high strength, flexible to rigid bond lines that resist temperature, humidity, and many chemicals. They may be classified into two groups:

- Single component. With single component adhesives, the adhesive components are premixed in their final proportions. However, they are chemically blocked. As long as they are not subjected to the specific conditions, which activate the hardener, they will not bond. They require either high temperature or substances or media (light, humidity) from the surroundings to initiate the curing mechanism. The containers in which this type of adhesive are transported and stored must be carefully chosen to prevent any undesired reactions. These adhesives are usually 100% solid systems. The six major subclasses are Anaerobic, Cyanoacrylates, Heat Cure, Moisture Cure, Radiation Cure, Silicones.

- Two-component. Two-component adhesives are 100% solids systems that obtain their storage stability by separating the reactive components. They are supplied as “resin” and “hardener” in separate containers. It is important to maintain the prescribed ratio of the resin and hardener in order to obtain the desired cure and physical properties of the adhesive. The two components are only mixed together to form the adhesive a short time before application with cure occurring at room temperature. Since the reaction typically begins immediately upon mixing the two components, the viscosity of the mixed adhesive increases with time until the adhesive can no longer be applied to the substrate or bond strength is decreased due to diminished wetting of the substrate. Formulations are available with a variety of cure speeds providing various working times (work life) after mixing and rates of strength build-up after bonding. Final strength is reached in minutes to weeks after bonding depending on the formulation. Adhesive must be cleaned from mixing and application equipment before cure has progressed to the point where the adhesive is no longer soluble. Depending on work life, two component adhesives can be applied by trowel, bead or ribbon, spray, or roller. Assemblies are usually fixture until sufficient strength is obtained to allow further processing. If the faster rate of cure (strength build-up) is desired, heat can be used to accelerate the cure. This is particularly useful when parts need to be processed more quickly after bonding or additional work life is needed but a slower rate of strength build-up cannot be accommodated. When cured, two component adhesives are typically tough and rigid with good temperature and chemical resistance.

Two-component adhesives can be mixed and applied by hand for small applications. However, this requires considerable care to ensure the proper ratio of the components and sufficient mixing to ensure proper cure and performance. There is usually considerable waste involved in hand mixing as well. As a result, adhesive suppliers have developed packaging

that allows the components to remain separate for storage and also provides a means for dispensing a mixed adhesive, e.g. side-by-side syringes, concentric cartridges. The package is typically inserted into an applicator handle and the adhesive is dispensed through a disposable mixing nozzle. The proper ratio of components is maintained by virtue of the design of the package and proper mixing is ensured by the use of the mixing nozzle. The adhesive can be dispensed from these packages multiple times provided the time between uses does not exceed the work life of the adhesive. If the work life is exceeded, a new mixing nozzle must be used. For larger applications, meter-mix equipment is available to meter, mix, and dispense adhesive packaged in containers ranging from quarts to drums. Four major types of two-component adhesives include: Epoxies, Methyl Methacrylates, Silicone Adhesives, Urethanes.

2.3.2.3) Pressure sensitive

The special feature of pressure sensitive adhesives is that they do not solidify to form a solid material, but remain viscous. As a result, they remain permanently tacky and have the ability to wet surfaces on contact. Bonds are made by bringing the adhesive film in contact with the substrate and applying pressure. If the inadequate pressure is applied or the processing temperature is too low, bonding faults such as bubbles or detachment can occur. Since these adhesives are not true solids, the strength of pressure sensitive adhesives decreases when the temperature is increased. Pressure sensitive adhesives also exhibit a tendency to undergo creep when subjected to loads. They are typically formulated from natural rubber, certain synthetic rubbers, and polyacrylates.
Pressure sensitive adhesives can be supplied dissolved in organic solvents, as an aqueous dispersion, as a hot melt, or coated on a release liner as tape. Liquid applied (solvent or water based, hot melt) pressure sensitive adhesives can be applied in bead or ribbon, sprayed, or roll coated. After coating (and drying of solvent or water based systems), parts can be bonded or the adhesive covered with release liner for bonding later. The adhesive can be coated in a pattern to provide bonded and unbounded areas, e.g. assembly of membrane switches, filter frames. Pressure sensitive adhesives are often used to temporarily hold components like gaskets in position during assembly.

2.3.3) Forms

Adhesives of various chemistries are available in many different forms as well. For structural applications, adhesives are available as pastes, liquids, films, and supported films. The latter are supported on loose knit or mat-scrim cloth to improve the handling properties and also to offer some measure of thickness control. Many of these adhesives produce little or no outgassing when cured, significantly reducing the likelihood of voids within the adhesive. It is important that these adhesives be kept dry, as absorbed moisture can create significant void problems.
Thermosetting structural adhesives are normally available in two-part forms that are mixed through carefully

controlled stoichiometry into a product that cures within the desired time window. One part forms are also available in which the resin and hardener (crosslinking agent) are already mixed together. These one part forms must be kept at sufficiently low temperature that the reaction does not occur prematurely, sometimes utilizing latent crosslinking agents that are not active at low temperatures. One part thermosetting adhesives often have limited shelf life, and often must be stored at low temperatures, but do offer very high-performance capabilities. Pot life refers to the time after a two-part adhesive is mixed during which it is workable and will still make a satisfactory bond. Materials with too short of a pot life will harden too fast, and do not give the workers sufficient time to assemble the product. An excessively long pot life may delay the cure time and slow the assembly process.
Adhesives may be applied in a variety of ways depending on the form it comes in. Adhesives may be spread on a surface manually, or may be dispensed using a variety of sophisticated nozzles and robotic equipment that is currently available. Maintaining adherent cleanliness, providing proper jigs and fixturing during cure, and providing adequate cure conditions may all be important considerations for certain types of adhesives.

2.4 Epoxy adhesives

Because of their ability to adhere to a wide variety of materials, their high strength, their resistance to chemicals and environments, and their ability to resist creep under sustained load, epoxies are the most widely used structural adhesive. They are available in one component, heat curing, and two-component, room temperature curing systems. Unmodified epoxies cure to hard, brittle solids. Most adhesive formulations include modifiers to increase flexibility or toughness of the cured adhesive. This results in bond lines that are able to resist more peel and cleavage stress as well as impact.

Figure 2.2. Application of epoxy adhesives in aircraft

One component systems typically cure at temperatures from 250 to 350ºF (120 to 175ºF). Cold storage is required to provide sufficient shelf life. They provide rigid but tough bond lines and have excellent adhesion to metals. Chemical and environmental resistance are excellent. Most formulations have a paste consistency and can be applied by trowel or extruded as beads. They easily fill gaps and provide excellent sealing properties particularly against harsh chemicals. They are often used as alternatives to welding and rivets. Some

formulations can tolerate processing oil on the substrate and still obtain satisfactory bond strength.

One component heat curing film adhesives are typically based on epoxy resin formulated with curative and modifiers. They are very high-performance adhesives providing high strength, high fatigue resistance, and high-temperature resistance. These curing film adhesives require cold storage and have limited shelf-life after warming to room temperature. They are especially suited for bonding and laminating large areas. Epoxy film adhesives find most of their applications in the aerospace industry for assemblies of components such as aircraft panels and helicopter rotor blades. To obtain optimal performance and durability, aluminum substrates are usually chemically treated.

Two component epoxy adhesives are found in all market segments. The work life (time adhesive can be processed and bonded after mixing) can vary from a few minutes to several hours. Assemblies must be fixtured until the adhesive has cured sufficiently to have enough strength for handling and additional processing. Final cure and ultimate strength are obtained over hours to weeks depending on the formulation. High ambient temperature accelerates the rate of cure and shortens the work life. Low ambient temperature slows the rate of cure and extends the time before assemblies can be further processed. In general, adhesives that cure faster have lower final strength than those that cure more slowly. The major advantage of two component epoxy adhesives is that they are suitable for bonding nearly all substrates - metal, plastic, glass and ceramic, wood and wood products, and many types of rubber. In general, they have high resistance to physical and chemical influences and in addition, they have high long-term stability because they only have a limited tendency to undergo creep. Depending on the type, they can withstand continuous temperatures from 200oF (95°C) up to 390 ºF (200°C). Cured adhesives are typically hard and rigid and range from brittle to tough depending on the formulation.

Figure 2.3. One component and two component commercial epoxy adhesives.

2.5 Glass transition temperature

The glass transition temperature (T_g) is one of the most important properties of any polymer and refers to the temperature vicinity in which the amorphous portion of the polymer transitions from a hard, glassy material to soft, rubbery material. Although specific temperatures are often quoted for the glass transition temperature, it is important to remember that this transition temperature is a rate dependent process. For thermosetting structural adhesives, the glass transition temperature should normally be 50°C higher than the expected service temperature. Unless there are significant exotherms associated with the cure process, the glass transition temperature of an adhesive seldom exceeds the cure temperature. High-performance structural bonds often require an elevated temperature cure to provide a sufficiently high T_g in a reasonable cure time. One concern with such conditions, however, are the residual stresses which may develop with an assembled joint is cooled from the cure temperature to the service conditions.

2.6 Reference

[1] Mays G. C, Hutchinson A. R. Adhesives in Civil Engineering. ISBN 052132677X, *Cambridge University Press* (1992)

2.7 List of figures

Appendix 3

Glass coatings

Windows are essential components of buildings, which provide vision, air ventilation, passive solar gain, daylighting and the opportunity to leave the building in extreme situations. However, they play an important role in total energy consumed in buildings due to their remarkably higher U-values compared to other components of building envelope. For a typical building, the U-values of the roof, floor, external walls and windows are around 0.16, 0.25, 0.30 and 2.00 W/m^2 K, respectively [1]. Therefore, windows play a significant role in determining the heating and cooling load of a building, particularly when their overall area is large.

The incorporation of various thin film coatings (such as low emissivity, reflective, self-cleaning) has improved the energy performance of the glazing products. A basic reason is that they can show transparency in a limited and well-defined range, normally encompassing visible light in the $0.4<\lambda<0.7$ μm wavelength interval. In the infrared (IR) their metallic property leads to reflectance and at sufficiently short wavelengths, in the ultraviolet (UV), they become absorbing due to excitations across an energy gap. If the reflectance is in the range of thermal radiation, i.e., $3<\lambda<50$ μm at normal temperature, the emission of heat is impeded. If reflectance prevails at $0.7<\lambda<3$ μm, covering the IR part of the solar spectrum which carries about 50% of the solar energy, one can combine visible transmittance with the rejection of a large part of the solar energy and at the same time have low thermal emittance [2].

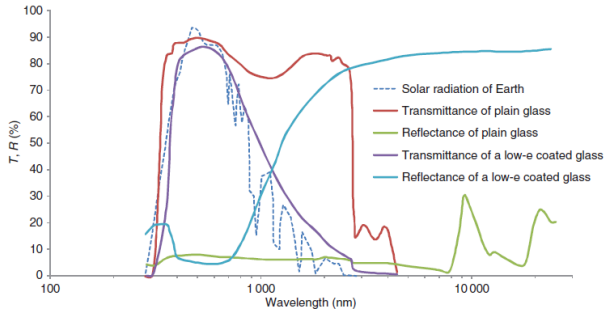

Figure 3.1. Optical properties of plain glass and a typical low-e coating [3].

However, it is important to say that windows do not comprise merely of the glazing component but also the frame, which has aspects of both heat transmission and air tightness to consider. In this regard, it is important to identify appropriate technologies to manufacture energy efficient windows, which will also improve the visual and thermal comfort of the occupants [1].

3.1 Glazing types

State-of-the-art glass coatings aim to provide high-performance thermal insulation, solar gain control, daylighting solutions or a combination. In the following sections, various glass coatings types are evaluated in terms of main performance parameters.

3.1.1) Low-emittance

Low-emittance coatings are basically metals or metallic oxides and aim at allowing a great proportion of the visible light in the solar spectrum to be transmitted while blocking much of the other wavelengths responsible for undesired solar heat gain. They can be split into two categories as hard and soft Low-E coatings. The soft Low-E coatings are less durable than the hard Low-E coatings, hence require extra protective layers. However, they are more transparent and have higher infrared.
Recent works clearly reveal that the Low-E coatings are capable of reducing heat gain through windows up to 48%. Therefore, they are widely used in modern architecture for thermal regulation of buildings. A significant amount of heat transport through thermal radiation can be mitigated by retrofitting existing conventional windows with Low-E coatings. Commercialized Low-E coatings are usually classified with respect to the ratio of visible to solar transmittance. Greater values of this ratio mean cooler daylighting. The best product in this respect has a VT value of 0.66 and an SHGC value of 0.34. A disadvantage is their currently high cost of production [1].

3.1.2) Smart

Smart glazing is a unique technology, which enables to change the visible and thermal transmittance characteristics to be able to obtain a desired level of lighting or heating from solar energy. Smart windows can be split into three categories as chromic materials, liquid crystals and suspended particle devices. To be able to control the optical properties of smart windows, it is required to utilize chromogenic materials.
Chromic materials based smart windows are the most reliable and up-and-coming of the three technologies. There are two states for electrochromic windows called transparent and colored. In the transparent state, the objective is to achieve as high visible transmittance as possible to be able to maximize the daylighting penetrating into the building. On the other hand, visible transmittance needs to be as low as possible in the colored state. Similarly, solar heat gain coefficient is expected to be as high and low as possible in the transparent and

colored state, respectively. One of the most promising advantages of the electrochromic windows is the possibility of retrofitting of the existing conventional windows. They have a remarkable potential to be widely implemented into existing windows and save the cost of new glass and glazing production. However, it needs to be noted that the electrochromic windows are incapable of providing full control of the uncomfortable direct sunlight effects, such as disability glare and high-luminance spots.
The most challenging point of smart windows at the moment is their higher cost compared to the other glazing technologies [1].

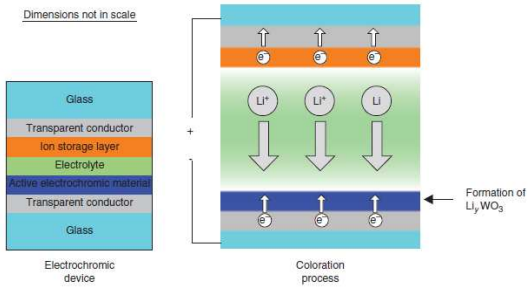

Figure 3.2. Structure and operation of a typical electrochromic device [3].

3.1.3) Photovoltaic

Photovoltaic glazing is a novel concept for modern architecture, and has the potential of mitigating greenhouse gas emissions from buildings. Utilizing photovoltaic cells in a window construction provides shading as well as electricity production. In this respect, total glazing area is an important parameter for this type of window. The technology is based on spraying a coating of silicon nanoparticles onto the window, which work as photovoltaic cells. Former photovoltaic glazing market is based on opaque c photovoltaic cells, which make them inefficient to utilize in residential buildings. Following the developments in semitransparent a-Si photovoltaic cell technology, photovoltaic glazing products become widespread in the market. In the production of the a-Si based photovoltaic glazing, the cells are made thin by adding a regular pattern of tiny holes. The solar transmittance of the photovoltaic glazing is adjusted by changing the area of these holes. The reduction in power outputs therefore related to the visual transmittance of the photovoltaic glazing. A recent work reveals that more than 50% of the undesired solar heat gain through conventional windows in summer can be reduced via photovoltaic glazing [1].

3.1.4) Self-cleaning

The TiO2 surface can decompose organic contamination with the aid of ultraviolet light. This concept has been used for many years in the covers of highway tunnel lamps in Japan. The

ratio of decontamination to contamination is crucial for the efficiency of self-cleaning glazing. The TiO_2 photo catalyst can provide the surface clean only if the photocatalytic decontamination rate is higher than that of contamination. The self-cleaning efficacy of TiO_2 surface can be improved by natural water flow due to the super hydrophilic property of TiO_2 surface. The best use of self-cleaning TiO_2 surfaces need to be exterior construction materials, since these materials could be exposed to abundant solar intensity and natural rainfall. Self-cleaning products covering tiles, glass, plastic films, tent materials, cement, etc. have already been commercialized and fabricated in Japan since the late 1990s and in other countries in recent years. Self-cleaning glazing products can be combined with antireflection coatings to produce multifunctional coatings. They can also be integrated into energy efficient triple glazing, vacuum glazing and aerogel products as the film is on the outer glass pane [1].

3.1.5) Reversible

Reversible windows are mostly the double glazed windows of which the exterior surfaces are integrated with highly reflective coatings. Having low solar heat gain coefficients enable them to be used efficiently in the summertime. They are reversed in the winter time in order to collect much of the beneficial solar radiation, however winter performance of these windows are some what lower than the summer performance [1].

3.1.6) Switchable electrochromic

The concept of switchable electrochromic window is based on nano-thick switchable coating on glass pane to be able to change the tint without loss of view. The switchable electrochromic windows can remarkably reduce the average annual daylight glare index and provide a significant amount of annual energy saving if the window area is large. They also notify that the energy and peak demand reductions can be notably higher if the reference window does not have exterior shading or state-of-the-art static glass [1].

3.1.7) Solar transmission controlled

This type of window technology is especially preferred and utilized by the countries, which have extremely hot climatic conditions. The concept is simply based on a window coated with a thin film, which remarkably prevents solar transmission [1].

3.1.7.1) Tinted

Tinted glazing products are fabricated by adding small metal oxides to the float or rolled glass composition. These small additions color the glass bronze, green, blue or gray but do not affect the basic properties of the glass except the solar energy transmission. The color is expected to be homogeneous throughout the thickness. Tinted glazing aims at reducing not only the solar transmission but also the undesired glare. Thermal transmission of a room with

tinted glazing can be reduced more than 20%. Further investigations indicate that light blue and green tint have higher visible performance and lower thermal transmittance among the existing products in market [1].

3.1.7.2) Reflective

The concept of reflective coating is based on lowering the solar heat gain coefficient by increasing the surface reflectivity of the material. Compared to the tinted glazing, reflective glazing has remarkably greater impact on reduction in solar transmission up to 50 %. It is also more preferable because of its glare control and visual superiority. The microscopically thin coating on one face of the glazing provides an attractive appearance and remarkably reduces glare from direct sunlight [1].

3.1.7.3) Anti-reflective

Anti-reflective coated glazing has a layer of coating on both sides to provide a clear and unobstructed view free from reflections both during the day and at night without affecting the U-value. In terms of light transmittance, enhancement around 10 % can be obtained through an anti-reflective coated glazing [1].

3.2 Film deposition technologies

The coatings used for solar energy and energy efficiency are normally thin films, with thicknesses between 10nm and 1 mm, backed by transparent or non-transparent substrates. Consequently thin-film deposition and thin-film optics are of much importance. Deposition constitutes a vast technological field and only the most common methods are mentioned here.

Sputter deposition is widely used to make uniform coatings on glass, polymers, metals, etc. Essentially a plasma is set up in a low pressure of inert and/or reactive gases, and energetic ions in the plasma dislodge material from a solid plate or cylinder of the raw material of the film (known as the target) and deposit these atoms as a uniform film on an adjacent surface (the substrate).

Evaporation can be an alternative to sputtering. Here, the raw material of the film is heated in vacuum so that a vapor transfers material to the substrate at a sufficient rate.
Systems for sputtering and evaporation are normally set up so that the deposition flux hits the substrate at a more or less normal angle, but angle-resolved sputtering is possible even for large areas; such techniques are of interest for applications requiring angular selectivity. Sputtering and evaporation are often referred to jointly as physical vapor deposition or PVD.

Other technologies can be applied without recourse to vacuum. For example, sol–gel deposition involves immersion of a substrate in a chemical solution, withdrawal at a controlled rate, and subsequent heat treatment. Alternatively, the chemical solution can be applied by spray coating. Chemical vapor deposition (CVD) uses heat to decompose a vapor of a precursor chemical to make a thin film of a desired composition. A variety of the CVD

technique is called spray pyrolysis; a fluid containing the precursor is then sprayed onto a hot substrate. This method is used on a large scale for deposition of tin oxide-based films on hot glass, either in a separate process or continuously onto the hot glass as it comes out from the float glass production and is transferred to the cooling stage. Electrochemical techniques include cathodic electrodeposition from a chemical solution and anodic conversion of a metallic surface especially of Al to form a porous oxide. Numerous alternative techniques exist as well [2].

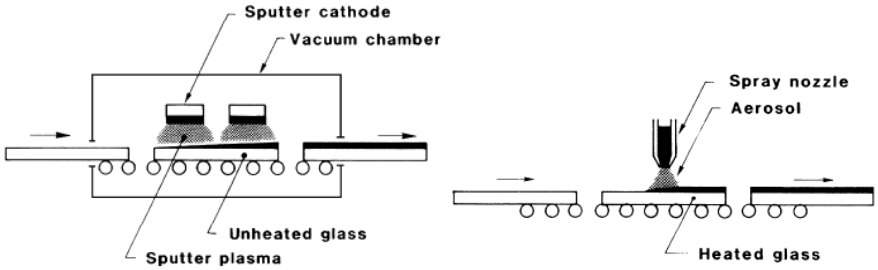

Figure 3.3. Sputtered deposition and spray pyrolysis techniques [2].

3.3 Types of Low-E coatings

Two groups of materials are of particular interest for use as low-E coatings: doped metal oxides and film combinations that incorporate metal layers. The typical thickness of the first group of films is on the order of 10^{-1} μm. They are hard, compact, strongly adherent to glass, chemically inert, their luminous and near-IR absorbance can be low, and their thickness does not affect electrical resistance. The thickness of the second group of films is on the order of 10^{-2} μm and they are soft, porous, poorly adherent to glass substrates, and chemically reactive. In this group of films, the electrical resistance is strongly thickness-dependent [3].

3.3.1) Doped metal oxides

Low-E coatings based on doped metal oxides comprise a host lattice (usually In_2O_3, SnO_2, or ZnO) that is doped by metal or halide atoms. The most common representatives of this group of films are tin-doped indium oxide (In_2O_3:Sn, usually called ITO), fluorine-doped tin oxide (SnO_2:F, usually called TFO), and gallium-doped zinc oxide (ZnO:Ga, usually called GZO). Doping is accomplished either by adding a higher-valence metal, by replacing some oxygen with fluorine, or by oxygen vacancies. The compounds mentioned above have wide enough band gaps to allow considerable transmission in the visible and doping is feasible to a level high enough to render the materials IR reflecting and electrically conducting. In doped metal oxides, the degree of doping determines the position of the transition wavelength (λ_T): the higher the doping, the more metal-like the films are and λ_T appears at lower wavelengths. However, in these films, doping cannot be brought to a sufficiently high level required for

solar control; their λ_T usually lies in the near IR and, thus, doped metal oxide coatings are used mostly for thermal insulation. The main advantage of the doped metal oxides, compared to metal-based films, is the chemical and mechanical stability, which allows their use on glass surfaces exposed to ambient conditions. This is why these films are referred to as 'hard coatings' [3].

3.3.2) Coatings with metal layers

In this type of coatings, the highly reflective metal film (that would otherwise be opaque in the visible) is sandwiched between two dielectric layers that have an antireflective effect: with an appropriate index of refraction and thickness, the light beams reflected on the front and back surfaces of each of the dielectric layers are of opposite phase and of nearly equal amplitude. Thus, they interfere destructively and as a result, the film reflectivity is diminished. One is then led to dielectric/metal/dielectric (D/M/D hereafter) multilayers. Dielectrics with high refractive indices, usually metal oxides, such as TiO_2, ZnO, ZnS, SnO_2, Bi_2O_3, and In_2O_3, are suitable. Appropriate metals are the so-called 'noble' ones, such as Ag, Au, Cu, and Al (given in order of decreasing performance). Of all these metals, Ag is the most suitable, due to its low absorption in the visible. Coatings based on Au or Cu have inferior optical properties and a characteristic golden brown color.
To achieve high transmittance, the metal layer needs to be as thin as possible. The growth mechanism of metal layers on glass imposes the limit: in the initial stages of their development on glass and other dielectric materials, metal films form tiny nuclei. With material continuously added on the substrate, these nuclei grow via surface diffusion and direct impingement, into islands that are discontinuous and possess a fractal nature. Further thickening of the metal film leads to large-scale coalescence and to continuous films. The coalescence thickness is about 15 nm for thermally evaporated Ag films and can be reduced to about 9 nm using other methods such as sputtering and ion-assisted deposition.
In these stacks, the metal layer thickness governs the coating properties. With the metal thickness increasing, the coating electronic conductivity increases, and its thermal emittance and luminous transmittance decrease.

3.4 References

[1] Cuce E, Riffat S. B. A state-of-the-art review on innovative glazing technologies. *Renewable and Sustainable Energy Reviews* 41 (2015) 695–714

[2] Granqvist C. G. Transparent conductors as solar energy materials: A panoramic review. *Solar Energy Materials & Solar Cells* 91 (2007) 1529-1598

[3] Leftheriotis G, Yianoulis P. Glazings and Coatings. University of Patras, Patras, Greece (2012)

3.5 List of figures